Research supported by the
National Autonomous University
of Mexico (UNAM) scholarship through
the Dirección General de Asuntos
del Personal Académico and by
NSF under Grant ATM-9729970 and
by NOAA under Grant NA67RJ0152.

PREDICTIONS FOR THE FINAL EQUILIBRIUM STATE OF FLOWS ON THE SPHERE

by

Ricardo Prieto González

Colorado State University

Wayne H. Schubert, PI

DEPARTMENT OF ATMOSPHERIC SCIENCE

PAPER NO689

PREDICTIONS FOR THE FINAL EQUILIBRIUM STATE OF FLOWS ON THE SPHERE

by

Ricardo Prieto González

Department of Atmospheric Science
Colorado State University
Fort Collins, CO 80523

Fall 1999

Atmospheric Science Paper No. 689

ABSTRACT

PREDICTIONS FOR THE FINAL EQUILIBRIUM STATE OF FLOWS ON THE SPHERE

Taking as motivation the experimental evidence, both observational and numerical, that unforced high-Reynolds number flows have a tendency to an equilibrium state with dominant coherent structures, two theories that predict the end-state of the flow are extended to the case of a spherical domain in order to apply them to large-scale meteorological problems.

The maximum entropy theory is a statistical mechanics approach that abandons the idea of following the precise changes of the fluid, predicting instead a "macroscopic" state, based on the assumption that the most probable macroscopic state is the one that corresponds to the final equilibrium state of the flow; the specification of the actual values of total kinetic energy, angular momentum and circulation of the flow define the structure of the equilibrium state.

The minimum enstrophy theory is based on results of low diffusion numerical experiments, where the values of the domain integrated kinetic energy and circulation are approximately constant over time, while the value of the enstrophy (i.e., one-half the domain integrated squared vorticity) has a considerable decay with time. Using the tools of the calculus of variations, the equilibrium state of the flow is predicted by minimizing the enstrophy while keeping constant the initial value of either total kinetic energy or total angular momentum.

A nonlinear barotropic non-divergent numerical model on the sphere is used to perform long-time integrations of barotropically unstable initial conditions. The type of flows studied are northern hemisphere stratospheric polar vortices, tropical shear layers and alternating zonal jets, the last being integrated both on a rotating and non-rotating sphere.

Predictions of the zonally-independent equilibrium state are compared with the zonal average of the direct numerical integration after 100 days of evolution for the stratospheric polar vortex experiments. Maximum entropy theory has good predictive skill for the zonal wind and absolute

vorticity profiles, as well as for the statistical distribution of traced air parcels. Minimum enstrophy theory has good skill for the zonal wind and absolute vorticity profiles, but just for the cases where mixing is confined to a polar cap, failing in cases where mixing is global or inside a latitude belt; for the latter case a second version of the minimum enstrophy theory, the two-edges problem, shows considerable improvement compared with the one edge solution.

For the tropical shear layer experiments, the minimum enstrophy theory with two-edges and constant energy captures a northward displacement of the easterly wind maximum, as well as the flattening of the absolute vorticity profile in tropical regions, behaviour which is consistent with the direct numerical integration. Maximum entropy theory qualitatively captures changes of the flow in the southern hemisphere, but shows strong sensitivity to small variations of the scale and strength of the initial condition. Predictions from minimum enstrophy theory with two edges and constant angular momentum, with one edge and constant energy, and with one edge and constant angular momentum, show little skill predicting the end-state; the weak decay of absolute enstrophy observed in the direct numerical integration for these cases is a major factor in the predictive skill of the theory.

Two-dimensional predictions of equilibrium states were found using maximum entropy theory for an initial condition with alternating zonal jets. For the rotating sphere, a maximum entropy solution was found which contains a number of zonally elongated coherent structures that resemble the direct numerical integration after 150 days of evolution. The non-rotating sphere case reveals the possibility of having more than one equilibrium state, and that the end-state chosen by the nonlinear evolution might be a linear combination of quasi-orthogonal maximum entropy states.

ACKNOWLEDGEMENTS

I want to thank my advisor Dr. Wayne Schubert for his guidance and patience during my studies at Colorado State University. I also want to thank my commitee members Drs. William Gray, Michael Montgomery and Gerald Taylor for their valuable comments and suggestions on this manuscript, as well as for the time spent providing academic advice.

A special recognition is given to the group members, Paul Ciesielski, Gail Cordova, Matthew Garcia, James Kossin, Katherine Harris, Scott Hausman, Rosana Nieto Ferreira and Richard Taft for all the help, discussions, suggestions and friendship during the realization of this work.

I want to mention that this work would not have been possible without all the advise of Dr. Julián Adem, M. in Sc. René Garduño, Drs. Víctor Magaña, Fernando García and Arturo Quintanar. Thank you very much.

This work was supported by a National Autonomous University of México (UNAM) scholarship through the Dirección General de Asuntos del Personal Académico, by the National Science Foundation under Grant ATM-9729970, and by NOAA under Grant NA67RJ0152.

TABLE OF CONTENTS

LIST OF FIGURES

LIST OF TABLES

Chapter 1

INTRODUCTION

Coherent vortex structures are a well known characteristic of large scale atmospheric flows, for example the stratospheric polar vortex, midlatitude anticyclones, blocking action in the westerlies and, at a smaller scale, tropical cyclones.

Numerical simulations of barotropic flows (e.g., McWilliams 1984, Yoden and Yamada 1993, Polvani et al. 1994, Cho and Polvani 1996), as well as laboratory experiments (e.g., Van de Konijnenberg et al. 1998) have reported the emergence of isolated coherent vortices from initial turbulent conditions.

McWilliams (1984) modeled the decay of two-dimensional flow in a double-periodic square domain. An initially random condition on the vorticity field (Fig. 1.1a) evolves in time to a collection of discrete and isolated vorticity extrema (Fig. 1.1d); most of the isolated vortices are approximately axisymmetric, with exceptions when two or more of them are close enough to have a strong interaction. Time series for the kinetic energy (E), enstrophy (V) and the energy centroid wavenumber ($\bar{k}$) are shown in Fig. 1.2. The energy decay is less than 3% over a time of 40 units, where a unit is approximately a circulation time for the most energetic eddies. The enstrophy decay is substantial at the beginning, although it slows considerably after $t = 10$. The energy centroid wavenumber decreases monotonically with time, which means that energy is transferred to larger scales, although its rate slows down with time.

Montgomery et al. (1992) performed a simulation with initial conditions as close as possible to

those of McWilliams (1984), except that the duration of the run is approximately ten times longer. During the times of overlap, no significant differences were found. However, at long times the like-sign merger of vortices did not stop, but only slowed down. At the end of the simulation all possible like-sign vortex captures had occurred, and only one vortex of each sign remained. Figure 1.3 is a three-dimensional plot of the computed vorticity at four different times.

This kind of phenomenon has been studied from different theoretical points of view, such as the selective decay hypothesis (Matthaeus and Montgomery, 1980, Carnevale et al. 1991, 1992, Matthaeus et al. 1991) in which states of near minimal ratio of enstrophy to energy can be attained in short times compared with the decay time of the flow.

Making use of variational analysis Leith (1984) found two kinds of vortex structures in two-dimensional flow, which represent the selective decay of enstrophy towards a minimum value with the constraints of constant kinetic energy and angular momentum or circulation. For each, the vorticity is confined to a disk whose radius is determined by the value of the constraints. Young (1987) applied the selective decay of enstrophy to a fluid in a periodic β-plane channel. The minimum enstrophy flow in this case is either a parallel flow or a finite-amplitude Rossby wave, depending on the aspect ratio of the channel and the amount of energy and momentum within. Schubert et al. (1999) applied this *minimum enstrophy* idea to the redistribution of vorticity, asymmetric eye contraction and polygonal eyewalls in hurricanes, obtaining the minimum enstrophy radial profiles of vorticity, tangential wind, pressure and angular velocity, hypothesized as the end state of evolution for a hurricane after potential vorticity redistribution has been taken place. Their results show a good agreement between a time integration of a barotropic nondivergent model and the minimum enstrophy predictions with: a) constrained circulation and angular momentum, and b) constrained circulation and energy.

Onsager (1949) applied the standard methods of statistical mechanics to a system of point vortices in an incompressible frictionless fluid. This approach was extended to continuous vorticity fields by Joyce and Montgomery (1973), and further developed by Miller (1990), Robert (1991), Robert and Sommeria (1991) and Sommeria et al. (1991). The idea behind this theory is to compute a local probability distribution of the vorticity field ("macroscopic" or coarse grained view) which describes

the average "microscopic" or fine grain scale fluctuations of the vorticity. One basic hypothesis is that the macroscopic equilibrium state which is observed the most often, is that one for which the number of distributions of the microscopic vorticity field is a maximum: The most probable macroscopic state is the final equilibrium state of the flow.

To find the most probable macroscopic state, we must find the particular probability distribution of vorticity which maximizes the variable known as the "Boltzmann mixing entropy", subject to the integral constraints associated with the vorticity dynamics (such as the conservation of the kinetic energy, circulation and angular momentum), therefore the name "maximum entropy flows".

For the application of the maximum entropy theory to fluids we require some kind of quantization of the vorticity field. We will consider a two-dimensional fluid flow which consists of an array of N vorticity patches; as a schematic view of how we compute the most probable macroscropic state consider a microscopic state which consists of an array of $N = 4$ vorticity patches, each with a vorticity value of either zero or one. The macroscopic state will be the vorticity average of the array. Fig. 1.4 shows all the possible combinations for this system; each column represents an averaged vorticity of (from left to right) $\bar{\zeta} = 0, \frac{1}{4}, \frac{1}{2}, \frac{3}{4}$ and 1; the number of possible arrangements for each macroscopic vorticity value is, using the laws of combinatorics, 1, 4, 6, 4 and 1 respectively.

From this example, the macroscopic state which is observed the most often (6 out of 16 times) is that which has a vorticity average of $\bar{\zeta} = \frac{1}{2}$; therefore, that is the most probable macroscopic state which maximizes the mixing entropy.

For fluids which consist of a large number of vorticity patches ($N \to \infty$), the macroscopic state which maximizes the mixing entropy will be present an overwhelming number of times compared with the rest of macroscopic states and, therefore, will have the biggest probability of being the one observed.

Robert and Sommeria (1991) proposed to apply the predictions of the maximum entropy equilibrium flows to geophysical problems, in particular to the atmosphere. In the present work minimum enstrophy and the statistical equilibrium theories are applied to atmospheric problems in spherical geometry. The class of flows that will be considered are the stratospheric polar vortex, tropical shear layers and banded structures (jets).

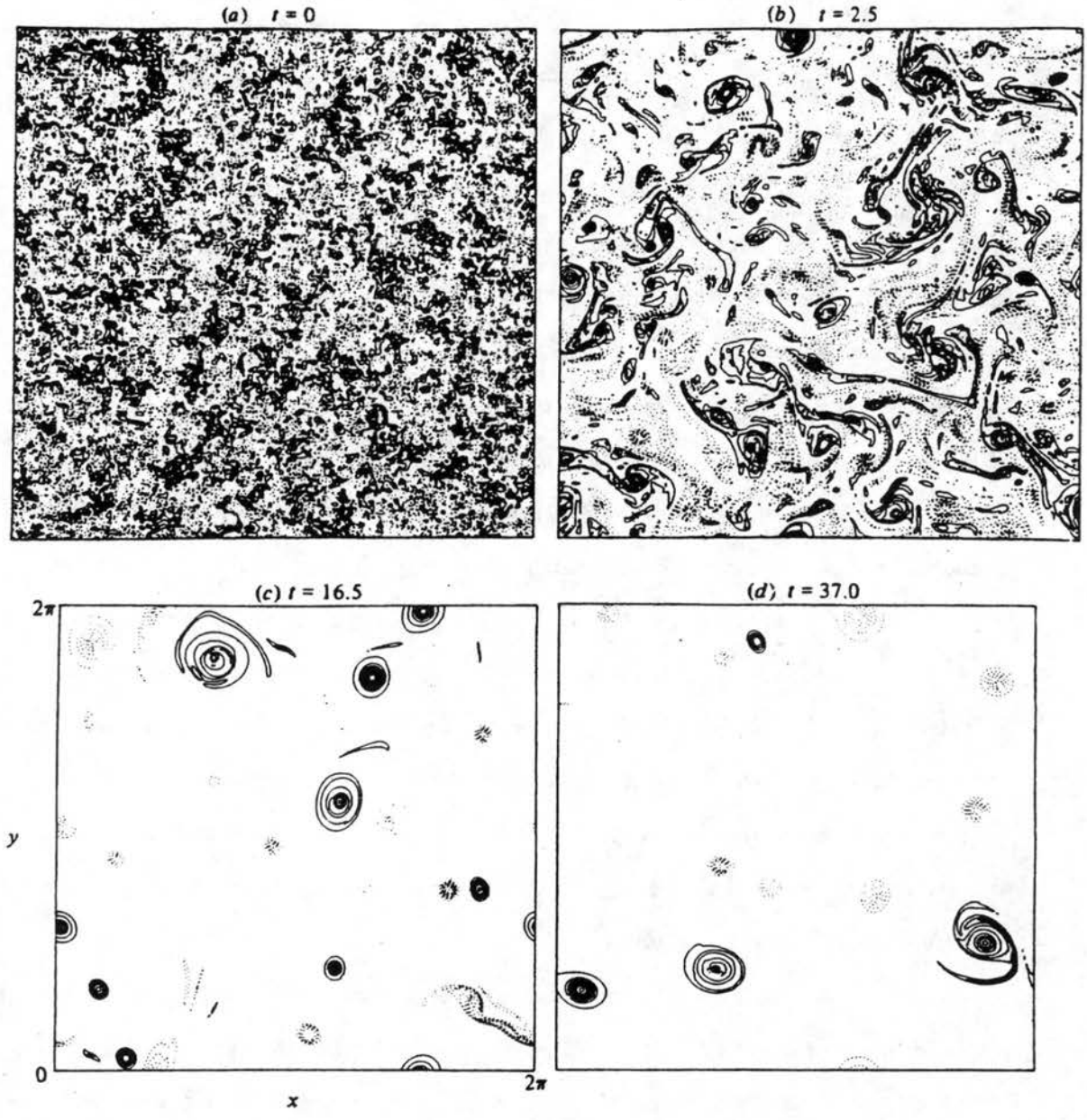

Figure 1.1: Vorticity at $t = 0, 2.5, 16.5$ and 37. The contour interval is 8 for the first of these and 4 thereafter. Positive contours are solid and negative dashed; the zero contour has been deleted. From McWilliams (1984).

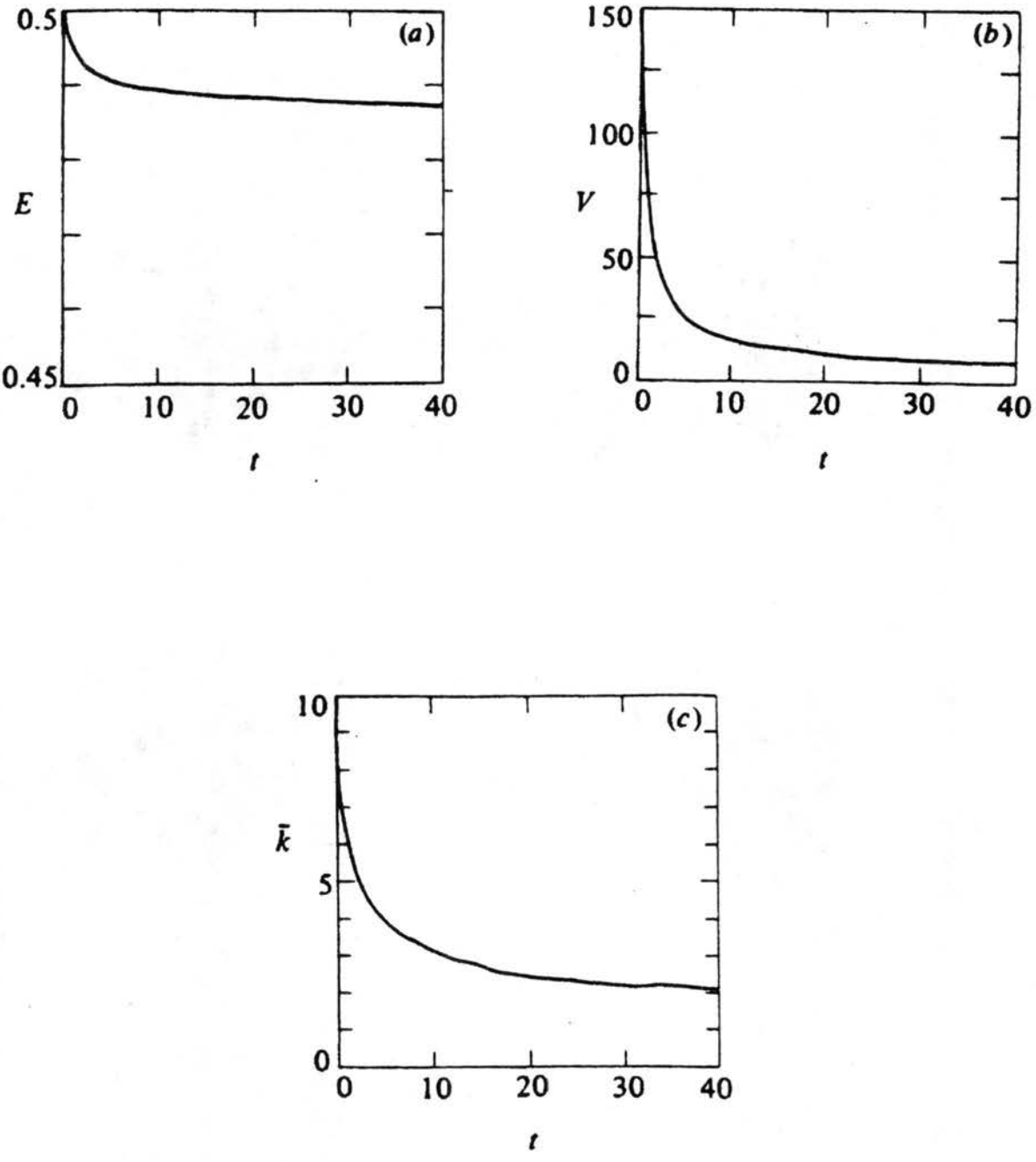

Figure 1.2: Time series of E, V and $\bar{k}$. From McWilliams (1984).

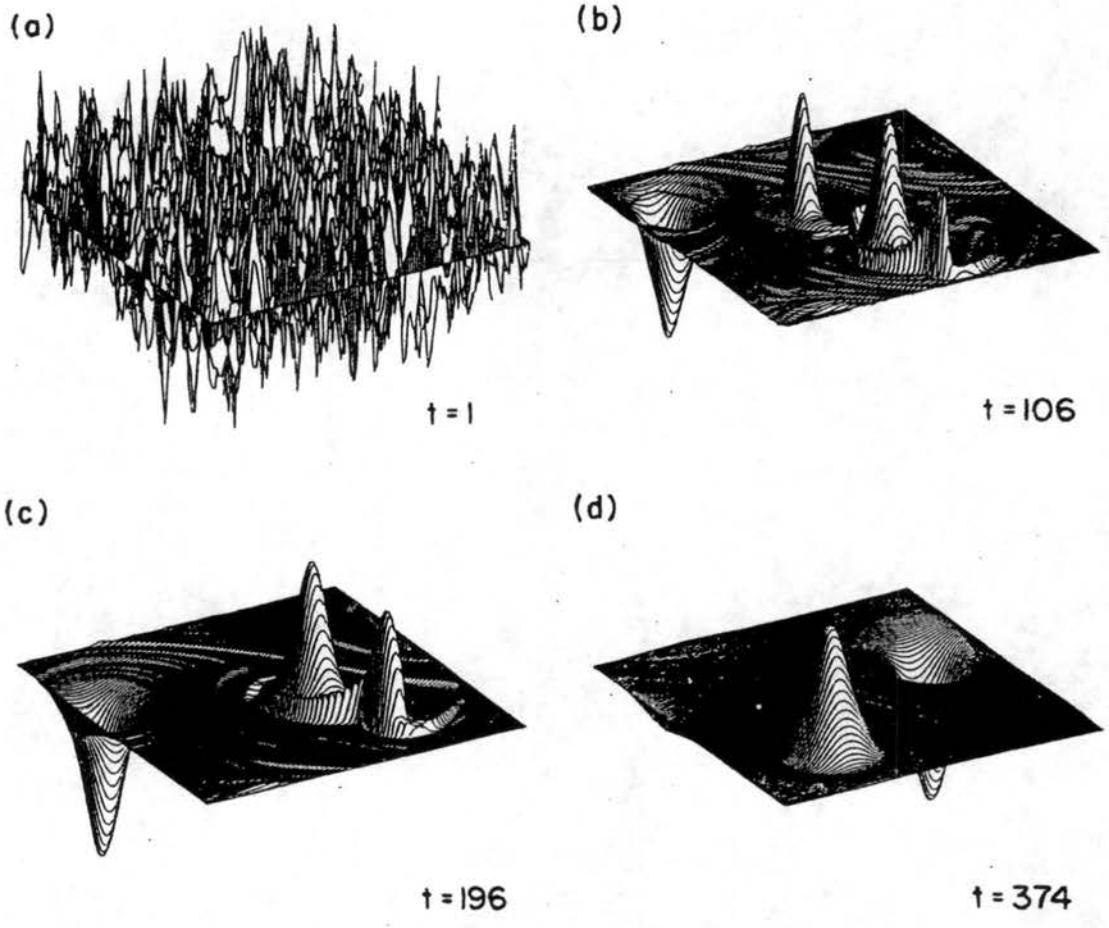

Figure 1.3: Three-dimensional perspective plot of the computed vorticity versus x and y at four different times. From Montgomery et al. (1992).

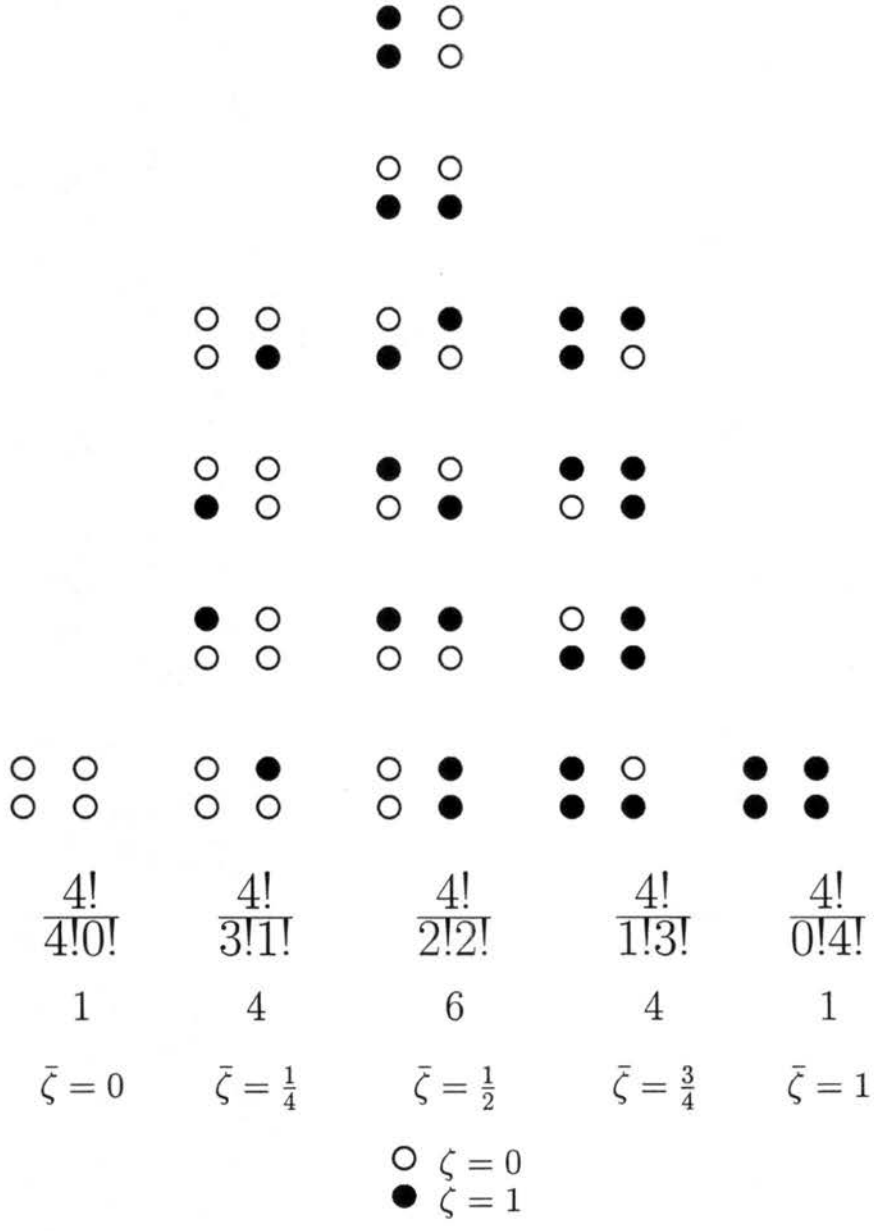

Figure 1.4: All the microscopic states which can be constructed with 4 vorticity patches with vorticity value of either zero (open circle) or one (filled circle). The microscopic states are arranged in columns with the same macroscopic (or average) vorticity $\bar{\zeta}$. The fractional numbers down the last line of arrays represent the total number of microstates computed with the laws of combinatorics, followed down by their integer value.

Chapter 2

BAROTROPIC NON-DIVERGENT NUMERICAL MODEL

Although the study of the real atmosphere requires the use of a three dimensional model with the inclussion of boundary layer, moist and radiative processes, this work concentrates on the basic conservative dynamics. Therefore we will make use of a barotropic nondivergent model, based on the nonlinear dynamics of vorticity. This model is highly idealized and can not be used to give an accurate description of the atmospheric circulation, but with its use we expect to have a better understanding of the dynamical processes occurring in different atmospheric problems.

When we consider motion that is horizontally nondivergent and barotropic, the governing equations of atmospheric flow reduce to the vorticity equation, which states the material conservation of absolute vorticity following a fluid element,

$$\frac{D\zeta}{Dt} = 0, \tag{2.1}$$

where

$$\frac{D}{Dt} \equiv \frac{\partial}{\partial t} + u\frac{\partial}{a\cos\phi\partial\lambda} + v\frac{\partial}{a\partial\phi}, \tag{2.2}$$

is the material derivative, and

$$\zeta = 2\Omega\sin\phi + \frac{\partial v}{a\cos\phi\partial\lambda} - \frac{\partial(u\cos\phi)}{a\cos\phi\partial\phi}, \tag{2.3}$$

is the absolute vorticity, with u and v the eastward and northward components of the velocity, λ the longitude, ϕ the latitude, t the time, a the radius of the earth, and Ω the angular rotation rate

of the earth.

Thus, under barotropic nondivergent conditions, the absolute vorticity behaves as a tracer of horizontal air motion and is rearranged by the circulation. On large scales, the actual atmospheric circulation tends to remain close to barotropic, which makes absolute vorticity approximately conserved.

The horizontal velocity field can be computed with the aid of the streamfunction ψ:

$$u = -\frac{\partial \psi}{a \partial \phi}, \qquad v = \frac{\partial \psi}{a \cos\phi \partial \lambda}, \tag{2.4}$$

as a result, the prognostic variable ζ can be expressed as a function of ψ by substituing (2.4) into (2.3) to obtain

$$\zeta = 2\Omega \sin\phi + \nabla^2 \psi, \tag{2.5}$$

where ∇^2 is the two-dimensional Laplacian operator.

With suitable initial conditions, the barotropic nondivergent vorticity equation (2.1) can be integrated for the motion at a later time.

2.1 Linear stability analysis

For a qualitative analysis of the stability of the barotropic nondivergent vorticity equation (2.1), we will use the perturbation method, where all field variables are divided into a basic state plus a perturbation (denoted by primed quantities), which is the local deviation of the field from the basic state. In that case, the linearized version of equation (2.1) is

$$\left(\frac{\partial}{\partial t} + \overline{u}\frac{\partial}{a\cos\phi\partial\lambda}\right)\nabla^2\psi' + \frac{1}{a^2\cos\phi}\frac{d\overline{\zeta}}{d\phi}\frac{\partial\psi'}{\partial\lambda} = 0, \tag{2.6}$$

where $\overline{u}(\phi)$ is the basic zonal flow, $\overline{\zeta}(\phi) = -\frac{1}{a\cos\phi}\frac{d}{d\phi}(\overline{u}\cos\phi) + 2\Omega\sin\phi$, and $\psi'(\lambda,\phi,t)$ is an infinisitesimal disturbance of the streamfunction.

Defining $\mu \equiv \sin\phi$ we can represent ψ' as

$$\psi'(\lambda,\mu,t) = Re\sum_{n=m}^{N}\psi_n^m P_n^m(\mu)e^{i(m\lambda-\sigma t)}. \tag{2.7}$$

The spherical harmonic functions, $P_n^m(\mu)e^{im\lambda}$, used in the spectral expansion are the eigensolutions of the Laplacian operator in spherical coordinates, and constitute a complete and orthogonal expansion basis.

Substituing (2.7) into (2.6) and noting that $\nabla^2\psi' = -\sum_{n=m}^{N} a^{-2}n(n+1)\psi_n^m P_n^m(\mu)e^{i(m\lambda-\sigma t)}$, we get

$$\frac{m\bar{u}}{a\sqrt{1-\mu^2}}\sum_{n=m}^{N} n(n+1)\psi_n^m P_n^m(\mu) - m\frac{d\bar{\zeta}}{d\mu}\sum_{n=m}^{N}\psi_n^m P_n^m(\mu) = \sigma\sum_{n=m}^{N} n(n+1)\psi_n^m P_n^m(\mu). \tag{2.8}$$

Applying equation (2.8) for $\mu = \mu_1, \mu_2, \cdots, \mu_N$, and fixed m, we get a system of equations which can be written in matrix form as

$$M_1\hat{\Psi} = \sigma M_2\hat{\Psi}, \tag{2.9}$$

or

$$(M_2^{-1}M_1)\hat{\Psi} = \sigma\hat{\Psi}, \tag{2.10}$$

which is an eigenvalue problem for the complex frequencies $\sigma = \sigma_r + i\sigma_i$, and the eigenvectors $\hat{\Psi} = (\psi_m^m, \psi_m^{m+1}, \psi_m^{m+2}, \cdots, \psi_m^{m+N-1})^T$.

Equation (2.10) can be solved by standard methods to determine if the perturbations have a sinusoidal character ($\sigma_i = 0$), or if they grow exponentially with time ($\sigma_i > 0$) or decay ($\sigma_i < 0$), as well as to determine their spatial structure. The software used to solve equation (2.10) was Mathematica Version 3.

2.2 Nonlinear model

The nonlinear system consistent with (2.1), (2.4) and (2.5) will be solved using the spectral transform method in space and explicit time differencing. The basic idea behind this method is to locally evaluate all nonlinear terms in physical space on an associated finite-difference-like grid also known as the transform grid. These terms are then transformed to wavenumber space to calculate linear terms and derivatives, and to obtain tendencies for the time-dependant variable.

The method basically consists of representing the physical scalar variables like ζ, as a truncated

series of spherical harmonic functions

$$\zeta(\lambda,\mu) = \sum_{m=-M}^{M} \sum_{n=|m|}^{N} \zeta_n^m P_n^m(\mu) e^{im\lambda}, \tag{2.11}$$

where M is the highest Fourier wavenumber included in the east-west representation and N is the highest degree of the associated Legendre functions included in the north-south representation. In this work, triangular truncation is used, meaning that $M = N$.

The complex coefficients of the spectral expansion (2.11) can be determined by projecting the scalar field $\zeta(\lambda,\mu)$ onto the normalized orthogonal basis

$$\zeta_n^m = \int_{-1}^{1} \left(\frac{1}{2\pi} \int_0^{2\pi} \zeta(\lambda,\mu) e^{-im\lambda} d\lambda \right) P_n^m(\mu) d\mu. \tag{2.12}$$

The inner integral in (2.12) represents a Fourier transform,

$$\zeta^m(\mu) = \frac{1}{2\pi} \int_0^{2\pi} \zeta(\lambda,\mu) e^{-im\lambda} d\lambda = \frac{1}{J} \sum_{j=1}^{J} \zeta(\lambda_j,\mu) e^{-im\lambda_j}, \tag{2.13}$$

where

$$\lambda_j = \frac{2\pi j}{J}, \tag{2.14}$$

which can be evaluated using a Fast Fourier Transform procedure. In order to allow an exact, unaliassed Fourier transform of quadratic terms, the number of gridpoints J in the east-west direction must satisfy $J \geq 3M + 1$.

The outer integral in (2.12) is performed using Gaussian quadrature,

$$\zeta_n^m = \int_{-1}^{+1} \zeta^m(\mu) P_n^m(\mu) d\mu = \sum_{k=1}^{K} \zeta(\mu_k) P_n^m(\mu_k) w_k, \tag{2.15}$$

where μ_k denotes the Gaussian latitudes, w_k the Gaussian weight at latitude μ_k, and K the number of Gaussian latitudes from pole to pole. The Gaussian latitudes (μ_k) are determined from the roots of the Legendre Polynomial $P_K(\mu)$, where the corresponding weights are given by

$$w_k = \frac{2(1-\mu_k^2)}{[K P_{K-1}(\mu_k)]^2}, \tag{2.16}$$

which also satisfy the relation

$$\sum_{k=1}^{K} w_k = 2. \tag{2.17}$$

The Gaussian grid used for the north-south transformation is generally chosen to allow exact, unaliased computations of quadratic terms. Therefore the number of Gaussian latitudes K must satisfy $K \geq (3N+1)/2$ for triangular truncation.

Redefining the intermediate variables $U \equiv u\cos\phi, V \equiv v\cos\phi, A \equiv U\zeta, B \equiv V\zeta, f \equiv 2\Omega\mu$, equation (2.1) can be written as

$$\frac{\partial \zeta}{\partial t} = -\frac{1}{a(1-\mu^2)}\frac{\partial A}{\partial \lambda} - \frac{1}{a}\frac{\partial B}{\partial \mu}. \tag{2.18}$$

Given the initial condition, the iterative method proceeds as follows:

STEP 1: The nonlinear terms in equation (2.18) are locally evaluated in physical space on an associated finite-difference-like grid (λ_j, μ_k), where λ_j is given by equation (2.14), and μ_k are the Gaussian latitudes with weights w_k given by (2.16),

$$A(\lambda_j, \mu_k) = U(\lambda_j, \mu_k)\zeta(\lambda_j, \mu_k), \tag{2.19}$$

$$B(\lambda_j, \mu_k) = V(\lambda_j, \mu_k)\zeta(\lambda_j, \mu_k). \tag{2.20}$$

STEP 2: A and B are then transformed into spectral space to calculate derivatives and to obtain tendencies for the time-dependent variable ζ_n^m,

$$A^m(\mu_k) = \frac{1}{J}\sum_{j=1}^{J} A(\lambda_j, \mu_k)e^{-im\lambda_j}, \tag{2.21}$$

$$B^m(\mu_k) = \frac{1}{J}\sum_{j=1}^{J} B(\lambda_j, \mu_k)e^{-im\lambda_j}, \tag{2.22}$$

$$\frac{\partial \zeta_n^m}{\partial t} = -\sum_{k=1}^{K}[imA^m(\mu_k)P_n^m(\mu_k) - B^m(\mu_k)(1-\mu_k^2)\frac{dP_n^m(\mu_k)}{d\mu}]\frac{w_k}{a(1-\mu_k^2)}; \tag{2.23}$$

integration over time is performed using a forward time step of $\frac{\Delta t}{2}$ to start the model integration (i.e., by setting variables at $t = -\frac{\Delta t}{4}$ equal to those at $t = 0$ and using a centered time step of $2\Delta t/4$), followed by a centered time step of Δt. All subsequent time steps are $2\Delta t$ with centered time differencing. Then, the explicit centered equations for the vorticity spectral coefficients is

$$\{\zeta_n^m\}^{(\tau+1)} = \sum_{k=1}^{K}\{\{\zeta^m(\mu_k)\}^{(\tau-1)}P_n^m(\mu_k)$$

$$-\frac{2\Delta t}{a(1-\mu_k^2)}[imA^m(\mu_k)P_n^m(\mu_k) - B^m(\mu_k)(1-\mu_k)\frac{dP_n^m(\mu_k)}{d\mu}]\}w_k. \tag{2.24}$$

STEP 3: Finally, the vorticity and horizontal velocity fields in physical space are computed, and one cycle of integration is completed:

$$\zeta(\lambda_j,\mu_k) = \sum_{m=-M}^{M}\sum_{n=|m|}^{M}\zeta_n^m P_n^m(\mu_k)e^{im\lambda_j}, \tag{2.25}$$

$$U(\lambda_j,\mu_k) = \sum_{m=-M}^{M}\sum_{n=|m|}^{M}\frac{a}{n(n+1)}[(\zeta_n^m - f_n^m)(1-\mu_k)\frac{dP_n^m(\mu_k)}{d\mu}]e^{im\lambda_j}, \tag{2.26}$$

$$V(\lambda_j,\mu_k) = -\sum_{m=-M}^{M}\sum_{n=|m|}^{M}\frac{a}{n(n+1)}[im(\zeta_n^m - f_n^m)P_n^m(\mu_k)]e^{im\lambda_j}. \tag{2.27}$$

The computer code for this model was derived from the shallow water model of Hack and Jacob (1992).

2.3 Diffusion term

The nonlinear numerical model used here also includes the hyperdiffusion term $-\nu(\nabla^4\zeta - \frac{4}{a^4}\zeta)$, which is added to the right hand side of equation (2.1), to control accumulations in the smallest scales resolved by the numerical model. This type of diffusion results in significantly weaker dampimg on the resolved scales than $\nu\nabla^2\zeta$ diffusion. The conservation of angular momentum requires adding the second term of $\frac{4}{a^4}\nu\zeta$. Thus, we expect the angular momentum to be a "rugged invariant" in the numerical simulations presented here.

To understand the role of dissipation in the numerical simulations we note that, since $\nabla^2 Y_n^m = -a^{-2}n(n+1)Y_n^m$, and $\nabla^4 Y_n^m = a^{-4}[n(n+1)]^2 Y_n^m$, the physical space partial differential equation $\partial\zeta/\partial t = -\nu\nabla^4\zeta$ transforms to the spectral space ordinary differential equation $d\zeta_n^m/dt = -\nu a^{-4}[n(n+1)]^2\zeta_n^m$, which has the solution $\zeta_n^m(t) = \zeta_n^m(0)e^{-t/\tau_n}$ where $\tau_n = a^4\nu^{-1}[n(n+1)]^{-2}$ is the decay time for spherical harmonic modes with total wavenumber n. The shortest decay time is for

spherical harmonic modes with the highest total wavenumber N is given by $\tau_N = a^4\nu^{-1}[N(N+1)]^{-2}$. For example, choosing $\nu = 2.23 \times 10^{14}$ m^{4}s^{-1}, and $N = 150$, results in $\tau_N = 4$ hours.

Three integral properties associated with the $-\nu(\nabla^4 - 4a^{-4})\zeta$ diffusion are the angular momemtum, energy and enstrophy relations

$$\frac{d\mathcal{M}}{dt} = 0, \tag{2.28}$$

$$\frac{d\mathcal{E}}{dt} = 2\nu\mathcal{P} - \frac{8\nu}{a^4}\mathcal{E}, \tag{2.29}$$

$$\frac{d\mathcal{Z}}{dt} = -2\nu\mathcal{L} + \frac{8\nu}{a^4}\mathcal{Z}, \tag{2.30}$$

where

$$\mathcal{M} = \int_{-1}^{1}\int_{0}^{2\pi} \mu\zeta \, d\lambda d\mu \tag{2.31}$$

is the angular momentum,

$$\mathcal{E} = \int_{-1}^{1}\int_{0}^{2\pi} \tfrac{1}{2}\nabla\psi \cdot \nabla\psi \, d\lambda d\mu \tag{2.32}$$

is the kinetic energy,

$$\mathcal{Z} = \int_{-1}^{1}\int_{0}^{2\pi} \tfrac{1}{2}\zeta^2 \, d\lambda d\mu \tag{2.33}$$

is the enstrophy,

$$\mathcal{P} = \int_{-1}^{1}\int_{0}^{2\pi} \tfrac{1}{2}\nabla\zeta \cdot \nabla\zeta \, d\lambda d\mu \tag{2.34}$$

is the palinstrophy, and

$$\mathcal{L} = \int_{-1}^{1}\int_{0}^{2\pi} \tfrac{1}{2}(\nabla^2\zeta)^2 \, d\lambda d\mu. \tag{2.35}$$

The integral relations (2.31)–(2.33) are easily obtained by multiplying the barotropic vorticity equation, with the hyperdiffusion term included, by μ, ψ and ζ respectively, and then integrating over the surface of the sphere. In the absence of dissipation, $\mathcal{E}$ and $\mathcal{Z}$ are strict invariants of the flow. With dissipation, $\mathcal{E}$ and $\mathcal{Z}$ are not strict invariants, the kinetic energy $\mathcal{E}$ tends to be essentially invariant (i.e., rugged) while the enstrophy $\mathcal{Z}$ selectively decays.

2.4 Trajectories

The nonlinear numerical model includes the computation of air parcel trajectories, which are of interest as tracers of materially conserved quantities, and in the quantitative estimation of atmospheric mixing. We are making the assumption that the rate of change of the tracers following the motion is negligible, as well as the diabatic effects and chemical sources and sinks, therefore, we are considering "quasi-conservative" tracers.

The trajectories are "passive" in the sense that the parcels are advected by the flow field, without having any feedback on the evolution of the flow field.

At every time-step, the model computes the new position of each of the initially defined air parcels, which are of the order of 1000, in the following manner:

i) Given the position (λ^n, ϕ^n) of the tracer at time t, find its closest four gridpoints.

ii) Compute the velocity field $u(\lambda^n, \phi^n), v(\lambda^n, \phi^n)$ as a weighted average of the velocity on the four closest gridpoints, giving more weight to the closest gridpoint.

iii) Compute the new position $(\lambda^{n+1}, \phi^{n+1})$ in physical space using a leapfrog scheme:

$$\lambda^{n+1} = \lambda^{n-1} + \frac{2\Delta t}{a \cos \phi^n} u(\lambda^n, \phi^n) \tag{2.36}$$

$$\phi^{n+1} = \phi^{n-1} + \frac{2\Delta t}{a} v(\lambda^n, \phi^n) \tag{2.37}$$

iv) Repeat the procedure for the next time-step.

Chapter 3

THEORY OF MAXIMUM ENTROPY FLOWS ON THE SPHERE

3.1 What is entropy?

The concept of entropy is involved in the second law of thermodynamics, and it is defined only for equilibrium states of a physical system. The entropy of the system is a function only of the state of the system, and is completely independent of the past history of the system.

The second law of thermodynamics is usually expressed as the definition of the differential change in entropy dS of the system when the system absorbs an amount of heat $\bar{d}Q$, at the temperature T of the system as it moves reversibly from one to a neighboring equilibrium state

$$dS = \frac{\bar{d}Q}{T}, \tag{3.1}$$

where the bar in the differential operator indicates that $\bar{d}Q$ is not an exact differential, but rather depends on the path over which the system is taken when the heat is absorbed. The second law as it is expressed in (3.1) tells us that if the heat absorbed by the system is divided by the temperature of the system at which the heat is absorbed, the result is a quantity (entropy) which is independent of the manner in which the heat is supplied to the system.

The integrated form of (3.1) defines the entropy difference between two states of the system, i

and f:

$$\Delta S = S_f - S_i = \int_i^f \frac{\bar{d}Q}{T}, \tag{3.2}$$

where the integral is evaluated for a reversible process connecting the two states of the system. Entropy has dimensions of energy divided by thermodynamic temperature, and the SI unit is joules per kelvin (J/K).

Notice that the difference or change in entropy is defined by using a reversible process to connect the two states. An irreversible process cannot be used in applying the definition. However, any reversible process that connects states i and f may be used. This independence of path corresponds to the fact that entropy is a function of state.

Any process can be described in terms of the changes in the system of interest and the changes in the surroundings of that system. Together our system and the relevant part of the surroundings form a larger, isolated system that we call the universe. Consider the entropy changes that occur for a process. We denote the change in entropy of our system by ΔS_{sys} and the change in entropy of its surroundigns by ΔS_{sur}. The sum of these changes is the change in entropy of the universe ΔS_{univ}:

$$\Delta S_{univ} = \Delta S_{sys} + \Delta S_{sur}. \tag{3.3}$$

In every calculation, we find that the entropy of the universe either increases or remains the same. The entropy of the universe never decreases. This result is in accord with another statement of the second law of thermodynamics: For any process, the entropy of the universe either increases (if the process is irreversible) or remains the same (if the process is reversible). In equation form,

$$\Delta S_{univ} \geq 0. \tag{3.4}$$

We should note that a reversible process is an idealization, all real processes are irreversible. For any real process, the entropy of the universe increases.

Entropy and the second law can also be interpreted at the microscopic level. There the description is in statistical terms. Instead of forbidding a particular process, the second law describes the process

as very highly improbable. For example, the probability is virtually zero that all of the gas molecules are in one part of a container after an irreversible free expansion of the gas from just one side of the container. Increasing entropy can be interpreted at the microscopic level as corresponding to a change from an ordered configuration to a more disordered one.

3.2 Historical remarks and general description of the maximum entropy method.

Direct numerical integrations like those presented in Legras and Dristchel (1993), Ishioka and Yoden (1994), Norton (1994), and Waugh and Plumb (1994), illustrate how barotropic instability processes can produce intricate vorticity patterns. Adaptive numerical methods, such as contour dynamics, require an increasing amount of computer time to advance one time step as the vorticity field becomes more complex. The spectral method described in chapter 2 is not adaptive and requires a fixed amount of computer time to advance one time step, no matter how complex the vorticity field. In the spectral method the production of finer and finer scales in vorticity is arrested by the model resolution and by the diffusion (or hyperdiffusion) processes operating near the resolution limit. While it is tempting to run spectral models at higher and higher resolution in order to follow vorticity structures to finer and finer scales, such costly pursuits do not necessarily produce fundamental dynamical advances. A statistical mechanics approach can be more useful. Such an approach has recently been developed by Miller (1990), Robert (1991), Robert and Sommeria (1991, 1992), Sommeria et al. (1991), Miller et al. (1992), Whitaker and Turkington (1994), Chavanis and Sommeria (1996), and Turkington and Whitaker (1996), but their basic ideas date back to the origins of the kinetic theory of gases and statistical mechanics.

In the kinetic theory of gases it is intended to explain the macroscopic properties of gaseous systems in terms of the motion of their component molecules. For example, the pressure of a gas is a consequence of the motion of its molecules and could be computed by considering the dynamical influence of the molecular collisions on the walls of the gas container.

In 1872 Boltzmann established a fundamental connection between the microscopic approach and

the phenomenological approach with what is known as the H-theorem. This theorem provides a molecular basis for the natural tendency of physical systems to approach, and stay, in a state of equilibrium. The H-theorem also provided a direct method of computing the entropy of a given physical system from a purely microscopic standpoint.

The general nature of the statistical mechanical procedure for the treatment of complicated systems consists in abandoning the attempt to follow the precise changes in state that would take place in a particular system, and in studying instead the behaviour of a collection or ensemble of systems of similar structure to the system of actual interest, distributed over a range of different precise states. From a knowledge of the average behaviour of the systems in a representative ensemble, appropiately chosen so as to correspond to the partial knowledge that we do have as to the initial state of the system of interest, we can then make predictions as to what may be expected, on the average, for the particular system which concerns us.

For the specific case we are dealing in this work, that is two-dimensional flows on the surface of a sphere, the specification of the actual values of the total energy, angular momentum and circulation of the flow, defines a particular macroscopic state of the system. However, at the "microscopic" level, there exist a large number of vorticity fields which are consistent with the macroscopic state. Each of the different vorticity fields specifies a particular "microstate". To a given macrostate of the system there does in general correspond a large number of microstates (vorticity fields), and it seems natural to assume that at any time t the system is equally likely to be in any of these microstates. This assumption is generally referred to as the postulate of "equal a priori probabilities" for all microstates consistent with a given macrostate.

The numerical method that is described in the next section has the purpose of finding the macrostate that has the largest number of microstates consistent with the knowledge we have of the state of the system (that is, its energy, angular momentum and circulation). The basic hypothesis is that the most probable macroscopic state of the system is that one which is the final equilibrium state of the flow.

It should be emphasized that this method has a statistical character, and that the results which

it provides are not necessarily precisely true in an individual case but in an average sense for the systems in an appropiately chosen ensemble.

3.3 Numerical method

Here we present a simple version of this maximum entropy argument. In particular, from the definition of the absolute vorticity by equation (2.3), we assume that the initial state consists of L levels of absolute vorticity $\hat{\zeta}_\ell$ with fractional area $\mathcal{A}_\ell$, $\ell = 1, \cdots, L$. These initial parameters are not all independent, but must satisfy $\sum_{\ell=1}^{L} \mathcal{A}_\ell = 1$ and $\sum_{\ell=1}^{L} \hat{\zeta}_\ell \mathcal{A}_\ell = 0$ (since the absolute vorticity integrated over the sphere must vanish). Denoting the initial absolute vorticity by $\zeta_0(\lambda, \mu)$ and the initial streamfunction by $\psi_0(\lambda, \mu)$, we note that $\nabla^2 \psi_0 = \zeta_0 - 2\Omega\mu$ on the spherical domain. The solution of this Poisson problem on the spherical domain is only unique to within an arbitrary additive constant. We fix this constant by requiring that $\int_{-1}^{1} \int_{0}^{2\pi} \psi_0(\lambda, \mu) d\lambda d\mu = 0$. We shall make a similar argument for the final streamfunction $\psi(\lambda, \mu)$, and hence require $\int_{-1}^{1} \int_{0}^{2\pi} \psi(\lambda, \mu) d\lambda d\mu = 0$.

To begin the argument let us suppose that, after the absolute vorticity field has become intricately stretched and folded, we sample the vorticity field at N points within a small neighborhood of λ, μ. Let n_ℓ denote the number of sampled points at which the absolute vorticity value $\hat{\zeta}_\ell$ is found. Then $\rho_\ell(\lambda, \mu) = n_\ell / N$ denotes the probability, at point (λ, μ), of finding the absolute vorticity $\hat{\zeta}_\ell$, and the macroscopic absolute vorticity at point (λ, μ) is

$$\zeta(\lambda, \mu) = \sum_{\ell=1}^{L} \hat{\zeta}_\ell \rho_\ell(\lambda, \mu). \tag{3.5}$$

From the statistical mechanics view, the macroscopic equilibrium state is that which has a maximum number of distributions of the sampled points with absolute vorticity $\hat{\zeta}_\ell$, in other words, the most mixed state. Therefore we must count the total number W of corresponding distributions. The number of possible arrangements having n_1 points with absolute vorticity $\hat{\zeta}_1$, n_2 points with absolute vorticity $\hat{\zeta}_2$, etc., is the multiplicity function W, which is given by

$$W = \frac{N!}{n_1! n_2! \cdots n_L!}. \tag{3.6}$$

The division by $n_1! n_2! \cdots n_L!$ comes from the fact that two sampled points of vorticity with the

same vorticity value are indistinguishable if their positions are interchanged (e.g., see Fig. 1.4). This is analogous to the Maxwell-Boltzmann-Planck statistics used in classical statistical mechanics for ensembles of molecules (see, e.g., Reed and Roy, 1995). The logarithm of the multiplicity function is $\ln W = \ln N! - \sum_{\ell=1}^{L} \ln n_\ell!$. Using the Stirling approximation (e.g., $\ln N! \approx N \ln N - N$ for large N), we obtain $\ln W \approx N \ln N - \sum_{\ell=1}^{L} n_\ell \ln n_\ell = -\sum_{\ell=1}^{L} n_\ell \ln(n_\ell/N)$, where we have used $\sum_{\ell=1}^{L} n_\ell = N$. We conclude that

$$\lim_{N\to\infty} \left(\frac{1}{N} \ln W \right) = -\sum_{\ell=1}^{L} \rho_\ell \ln \rho_\ell. \tag{3.7}$$

Considered as a function of $(\rho_1, \cdots, \rho_L)$ for $\rho_\ell \geq 0$ and with $\sum_{\ell=1}^{L} \rho_\ell = 1$ the function $-\sum_{\ell=1}^{L} \rho_\ell \ln \rho_\ell$ has its maximum value of $\ln L$ at $\rho_1 = \rho_2 = \cdots = \rho_L = 1/L$. In other words the multiplicity of microstates is a maximum when N/L of the sampled points in the neighborhood of (λ, μ) have absolute vorticity $\hat{\zeta}_1$, N/L have absolute vorticity $\hat{\zeta}_2$, etc.; this constitutes a well-mixed state.

We now define the Boltzmann mixing entropy $S[\rho_1(\lambda,\mu), \cdots, \rho_L(\lambda,\mu)]$ as

$$S[\rho_1(\lambda,\mu), \cdots, \rho_L(\lambda,\mu)] = \int_{-1}^{1} \int_{0}^{2\pi} \left(-\sum_{\ell=1}^{L} \rho_\ell(\lambda,\mu) \ln \rho_\ell(\lambda,\mu) \right) d\lambda d\mu. \tag{3.8}$$

For a description of the derivation of equation (3.8) see Appendix A.

The functional $S[\rho_1(\lambda,\mu), \cdots, \rho_L(\lambda,\mu)]$ measures the loss of information in going from the fine grain (microscopic) view to the coarse grain (macroscopic) view. To find the most probable macroscopic state, we must find the particular set of functions $\rho_\ell(\lambda,\mu)$, $\ell = 1, \cdots, L$, which maximize $S[\rho_1(\lambda,\mu), \cdots, \rho_L(\lambda,\mu)]$ subject to all the integral constraints associated with the inviscid vorticity dynamics. The kinetic energy constraint requires that the final and initial kinetic energies be equal, i.e., $\int_{-1}^{1} \int_{0}^{2\pi} \frac{1}{2}(u^2 + v^2) d\lambda d\mu = \int_{-1}^{1} \int_{0}^{2\pi} \frac{1}{2}(u_0^2 + v_0^2) d\lambda d\mu$, where the subscript zero denotes the initial state. With the aid of $(u, v\cos\phi) = (-\partial\psi/a\partial\phi, \partial\psi/a\partial\lambda)$ and $(u_0, v_0\cos\phi) = (-\partial\psi_0/a\partial\phi, \partial\psi_0/a\partial\lambda)$, we can use integration by parts to express the kinetic energy constraint as $\int_{-1}^{1} \int_{0}^{2\pi} \psi\zeta d\lambda d\mu = \int_{-1}^{1} \int_{0}^{2\pi} \psi_0\zeta_0 d\lambda d\mu$. Using (3.5), we can write the kinetic energy constraint as (3.10). The angular momentum constraint requires that the final and initial angular momenta be equal, i.e., $\int_{-1}^{1} \int_{0}^{2\pi} m d\lambda d\mu = \int_{-1}^{1} \int_{0}^{2\pi} m_0 d\lambda d\mu$, where $m = (u + \Omega a\cos\phi)a\cos\phi$ is the absolute angular momentum per unit mass. With the aid of (2.3) we can use integration by parts to express the angular momentum constraint as $\int_{-1}^{1} \int_{0}^{2\pi} \mu\zeta d\lambda d\mu = \int_{-1}^{1} \int_{0}^{2\pi} \mu\zeta_0 d\lambda d\mu$. Using (3.5), we can write

the angular momentum constraint as (3.11). In other words, the variational problem is to find the expectation functions $\rho_\ell(\lambda,\mu)$ by maximizing (3.8) subject to the circulation constraints

$$\int_{-1}^{1}\int_{0}^{2\pi} \rho_\ell(\lambda,\mu)d\lambda d\mu = 4\pi\mathcal{A}_\ell, \qquad \ell = 1,2,\cdots,L, \tag{3.9}$$

the energy constraint

$$\int_{-1}^{1}\int_{0}^{2\pi} \psi\left(\sum_{\ell=1}^{L}\hat{\zeta}_\ell\rho_\ell\right)d\lambda d\mu = \int_{-1}^{1}\int_{0}^{2\pi}\psi_0\zeta_0 d\lambda d\mu, \tag{3.10}$$

and the angular momentum constraint

$$\int_{-1}^{1}\int_{0}^{2\pi} \mu\left(\sum_{\ell=1}^{L}\hat{\zeta}_\ell\rho_\ell\right)d\lambda d\mu = \int_{-1}^{1}\int_{0}^{2\pi}\mu\zeta_0 d\lambda d\mu. \tag{3.11}$$

Making use of standard techniques of the calculus of variations, we take a linear combination of equations (3.8)–(3.11) in the following manner: multiply equation (3.8) by unity, equations (3.9) by α_ℓ, equation (3.10) by $\frac{1}{2}\beta$ and equation (3.11) by γ, then add, and take the variation (see Appendix B) of the resulting equation:

$$\begin{aligned}
0 &= \delta\int_{-1}^{1}\int_{0}^{2\pi}\sum_{\ell=1}^{L}\left[-\rho_\ell\ln\rho_\ell + \alpha_\ell\rho_\ell + \hat{\zeta}_\ell\left(\tfrac{1}{2}\beta\psi+\gamma\mu\right)\rho_\ell\right]d\lambda d\mu \\
&= \int_{-1}^{1}\int_{0}^{2\pi}\sum_{\ell=1}^{L}\left\{\left(-1-\ln\rho_\ell\right)\delta\rho_\ell + \alpha_\ell\delta\rho_\ell + \hat{\zeta}_\ell\left[\tfrac{1}{2}\beta\left(\psi\delta\rho_\ell+\rho_\ell\delta\psi\right)+\gamma\mu\delta\rho_\ell\right]\right\}d\lambda d\mu \\
&= \int_{-1}^{1}\int_{0}^{2\pi}\sum_{\ell=1}^{L}\left[-1-\ln\rho_\ell+\alpha_\ell+\hat{\zeta}_\ell\left(\beta\psi+\gamma\mu\right)\right]\delta\rho_\ell\, d\lambda d\mu.
\end{aligned} \tag{3.12}$$

The quantities α_ℓ, β and γ are known as the Lagrange multipliers. For arbitrary variations $\delta\rho_\ell$ we obtain from (3.12)

$$1+\ln\rho_\ell = \alpha_\ell + \hat{\zeta}_\ell\left(\beta\psi+\gamma\mu\right), \qquad \ell = 1,2,\cdots,L. \tag{3.13}$$

Solving (3.13) for $\rho_\ell(\lambda,\mu)$ and requiring $\sum_{\ell=1}^{L}\rho_\ell = 1$, we obtain

$$\rho_\ell(\lambda,\mu) = \frac{1}{Z}\exp[\alpha_\ell + \hat{\zeta}_\ell(\beta\psi+\gamma\mu)], \tag{3.14}$$

where the partition function Z is given by

$$Z = \sum_{\ell=1}^{L}\exp[\alpha_\ell+\hat{\zeta}_\ell(\beta\psi+\gamma\mu)]. \tag{3.15}$$

Using (3.14) in (3.5), we obtain

$$\zeta = \frac{1}{Z}\sum_{\ell=1}^{L} \hat{\zeta}_\ell \exp[\alpha_\ell + \hat{\zeta}_\ell(\beta\psi + \gamma\mu)], \tag{3.16}$$

which can be used in the invertibility relation

$$\nabla^2\psi = \zeta - 2\Omega\mu \tag{3.17}$$

to obtain the streamfunction. Since the right hand side of (3.17) depends on ψ through (3.16), we are faced with solving a nonlinear partial differential equation for $\psi(\lambda,\mu)$ with yet to be determined Lagrange multipliers $\alpha_\ell, \beta, \gamma$. The equations for $\alpha_\ell, \beta, \gamma$ are obtained by enforcing the constraints (3.9)–(3.11). In summary, the solution of the maximum entropy flow problem involves solving the nonlinear system (3.9), (3.10), (3.11), (3.16), (3.17) for $\alpha_\ell, \beta, \gamma, \zeta(\lambda,\mu), \psi(\lambda,\mu)$, given the initial flow. Analytical solutions of this system are not easily obtained, and numerical methods are required.

Turkington and Whitaker (1996) have proposed an iterative algorithm based on the variational structure of the constrained optimization problem. The extension of this algorithm to the present geometry generates $\alpha_\ell^{(\nu)}, \beta^{(\nu)}, \gamma^{(\nu)}, \rho_\ell^{(\nu)}(\lambda,\mu), \zeta^{(\nu)}(\lambda,\mu), \psi^{(\nu)}(\lambda,\mu)$ from $\zeta^{(\nu-1)}(\lambda,\mu), \psi^{(\nu-1)}(\lambda,\mu)$ by maximizing $S[\rho_1^{(\nu)}(\lambda,\mu), \cdots, \rho_L^{(\nu)}(\lambda,\mu)]$, subject to the respective circulation constraint, the energy constraint and the absolute angular momentum constraint; then a set of equations for $\alpha_\ell^{(\nu)}, \beta^{(\nu)}, \gamma^{(\nu)}$ are obtained:

$$F_\ell\left(\alpha_1^{(\nu)}, \cdots, \alpha_{L-1}^{(\nu)}, \beta^{(\nu)}, \gamma^{(\nu)}\right) = 0, \qquad \ell = 1, 2, \cdots, L+1, \tag{3.18}$$

where

$$F_\ell\left(\alpha_1^{(\nu)}, \cdots, \alpha_{L-1}^{(\nu)}, \beta^{(\nu)}, \gamma^{(\nu)}\right) = 4\pi\mathcal{A}_\ell - \int_{-1}^{1}\int_0^{2\pi} \rho_\ell^{(\nu)}(\lambda,\mu)\,d\lambda d\mu, \qquad \ell = 1, 2, \cdots, L-1, \tag{3.19}$$

$$F_L\left(\alpha_1^{(\nu)}, \cdots, \alpha_{L-1}^{(\nu)}, \beta^{(\nu)}, \gamma^{(\nu)}\right) = \int_{-1}^{1}\int_0^{2\pi} \left[\tfrac{1}{2}\left(\psi_0\zeta_0 + \psi^{(\nu-1)}\zeta^{(\nu-1)}\right) - \psi^{(\nu-1)}\zeta^{(\nu)}\right] d\lambda d\mu, \tag{3.20}$$

$$F_{L+1}\left(\alpha_1^{(\nu)}, \cdots, \alpha_{L-1}^{(\nu)}, \beta^{(\nu)}, \gamma^{(\nu)}\right) = \int_{-1}^{1}\int_0^{2\pi} \mu\left[\zeta_0(\lambda,\mu) - \zeta^{(\nu)}(\lambda,\mu)\right] d\lambda d\mu. \tag{3.21}$$

Given the initial condition, the iteration proceeds as follows: 1) Knowing $\zeta^{(\nu-1)}(\lambda,\mu)$ and $\psi^{(\nu-1)}(\lambda,\mu)$ from the previous iteration (or from an initial guess), solve the $L+1$ algebraic equations

(3.18) for $\alpha_\ell^{(\nu)}, \beta^{(\nu)}, \gamma^{(\nu)}$; 2) Substitute the $\alpha_\ell^{(\nu)}, \beta^{(\nu)}, \gamma^{(\nu)}$ into (3.16) to obtain $\zeta^{(\nu)}(\lambda, \mu)$; 3) Knowing $\zeta^{(\nu)}(\lambda, \mu)$, solve the invertibility relation (3.17) for $\psi^{(\nu)}(\lambda, \mu)$, and return to step 1.

The invertibility is solved in spectral space using spherical harmonics $P_n^m(\mu)e^{im\lambda}$ as basis functions. Consider the points (λ_j, μ_k) where $\lambda_j = 2\pi j/J$ $(j = 1, 2, \cdots, J)$ and the Gaussian latitudes μ_k and weights G_k are computed from $P_{M+1}(\mu_k) = 0$. Then, the streamfunction ψ is obtained from the absolute vorticity ζ by the sequence of steps

$$\zeta^m(\mu_k) = \frac{1}{J}\sum_{j=1}^{J} \zeta(\lambda_j, \mu_k)e^{-im\lambda_j}, \tag{3.22}$$

$$\zeta_n^m = \sum_{k=1}^{K} G_k \zeta^m(\mu_k) P_n^m(\mu_k), \tag{3.23}$$

$$\psi_n^m = -\frac{a^2}{n(n+1)}\zeta_n^m, \tag{3.24}$$

$$\psi(\lambda_j, \mu_k) = \sum_{m=-M}^{M} \sum_{n=|m|}^{M} \psi_n^m P_n^m(\mu_k) e^{im\lambda_j}. \tag{3.25}$$

As in Whitaker and Turkington (1994), the stopping criteria for the iteration in ν is chosen to be

$$\frac{|E^{(\nu)} - E^{(0)}|}{|E^{(0)}|} \leq 5 \times 10^{-3}, \tag{3.26}$$

where

$$E^{(0)} = -\int_{-1}^{1}\int_{0}^{2\pi} \tfrac{1}{2}\psi_0\zeta_0 d\lambda d\mu, \tag{3.27}$$

$$E^{(\nu)} = -\int_{-1}^{1}\int_{0}^{2\pi} \tfrac{1}{2}\psi^{(\nu)}\zeta^{(\nu)} d\lambda d\mu. \tag{3.28}$$

The number of iterations required for convergence varies depending on the initialization, but typically from ten to twenty iterations are required to satisfy (3.26).

Chapter 4

THEORY OF MINIMUM ENSTROPHY FLOWS ON THE SPHERE

4.1 Introduction

In Chapter 2 we have presented the conservation laws for the time rate of change of angular momentum $\mathcal{M}$, energy $\mathcal{E}$ and enstrophy $\mathcal{Z}$ for the $-\nu(\nabla^4 - 4a^{-4})\zeta$ type diffusion. These are:

$$\frac{d\mathcal{M}}{dt} = 0, \tag{4.1}$$

$$\frac{d\mathcal{E}}{dt} = 2\nu\mathcal{P} - \frac{8\nu}{a^4}\mathcal{E}, \tag{4.2}$$

$$\frac{d\mathcal{Z}}{dt} = -2\nu\mathcal{L} + \frac{8\nu}{a^4}\mathcal{Z}, \tag{4.3}$$

where $\mathcal{P}$ and $\mathcal{L}$ are given by (2.34) and (2.35) respectively. For inviscid flow ($\nu = 0$) we have that both energy and enstrophy are strictly conserved.

Using the spherical harmonic expansion for the absolute vorticity

$$\zeta(\lambda, \mu) = Re \sum_{m=-M}^{M} \sum_{n=|m|}^{N} \zeta_n^m Y_n^m(\lambda, \mu), \tag{4.4}$$

and noting that

$$\nabla^2\zeta = Re \sum_{m=-M}^{M} \sum_{n=|m|}^{N} a^{-2} n(n+1) \zeta_n^m Y_n^m(\lambda, \mu), \tag{4.5}$$

we can express $\mathcal{Z}$ and $\mathcal{L}$ from their definitions (2.33) and (2.35) as

$$\mathcal{Z} = \int_{-1}^{1} \int_{0}^{2\pi} \frac{1}{2} \left(Re \sum_{m=-M}^{M} \sum_{n=|m|}^{N} \zeta_n^m Y_n^m(\lambda, \mu) \right)^2 d\lambda d\mu, \tag{4.6}$$

$$\mathcal{L} = \int_{-1}^{1}\int_{0}^{2\pi} \frac{1}{2}\left(a^{-2}n(n+1)Re\sum_{m=-M}^{M}\sum_{n=|m|}^{N}\zeta_n^m Y_n^m(\lambda,\mu)\right)^2 d\lambda d\mu. \tag{4.7}$$

Substituing (4.6) and (4.7) in (4.3) and using the orthogonality relations for spherical harmonics we get

$$\begin{aligned}\frac{d\mathcal{Z}}{dt} &= -2\nu(\mathcal{L} - \frac{4}{a^4}\mathcal{Z}) \\ &= -\nu\int_{-1}^{1}\int_{0}^{2\pi}\sum_{m=-M}^{M}\sum_{n=|m|}^{N}\left[\left(\frac{n(n+1)}{a^2}\right)^2 - \frac{4}{a^4}\right](Re[\zeta_n^m Y_n^m(\lambda,\mu)])^2\, d\lambda d\mu. \end{aligned}\tag{4.8}$$

Since the integrated vorticity is zero, $\zeta_0^0 = 0$. Then the term inside the integration in (4.8) is always non-negative and if $\nu > 0$, then $\frac{d\mathcal{Z}}{dt} < 0$. Therefore, in our numerical simulations we expect that enstrophy is a decaying function of time due to viscous dissipation.

Fjørtoft (1953) used the spherical harmonic expansion to compute the energy spectrum $\mathcal{E}(n,t)$ which is interpreted as the kinetic energy per unit mass per unit wavenumber that characterizes the flow field. The enstrophy spectrum is given by $\mathcal{Z}(n,t) = \frac{n(n+1)}{a^2}\mathcal{E}(n,t)$. Fjørtoft (1953) showed that the energy fluxes towards low wavenumbers, while because of the $\frac{n(n+1)}{a^2}$ term, enstrophy fluxes towards high wavenumbers (small scales). Physically, this can be interpreted as the formation of large eddies while vorticity is sheared out as filaments. If disturbances on the flow are generated at the larger spatial scales, they excite progressively smaller and smaller scales by the nonlinear term in (2.1). Flow at higher and higher n's is generated until it becomes dissipated by the viscous term at the smallest scales. The extra factor of $\frac{n(n+1)}{a^2}$ forces the enstrophy spectrum to peak at higher n, so that the effect of dissipation is greater on $\mathcal{Z}$ than on $\mathcal{E}$.

Merilees and Warn (1975) showed that in two-dimensional non-divergent flow on the plane and in a bounded region, roughly 70% of triad interactions lead to a larger energy exchange with lower wavenumbers, while about 60% exchange more enstrophy with higher wavenumbers. Extending that calculation to spherical geometry, Merilees and Warn (1975) estimated that, at the limit of large zonal wavenumber m, about 75% of interactions imply larger energy exchange with lower wavenumbers, and 55% exchange more enstrophy with higher wavenumbers; as m grows larger, those numbers converge to 70% and 60% respectively.

This enstrophy cascade towards large wavenumbers and energy inverse cascade towards small

wavenumbers has raised the hypothesis of selective decay used by Bretherton and Haidvogel (1976), Matthaeus and Montgomery (1980), Leith (1984), Young (1987) and Schubert et al. (1999). This hypothesis can be summarized as follows: The simplest state to which the flow might tend is that of minimum enstrophy compatible with the initial energy and/or other relevant constraints of the flow (like angular momentum).

Next, we develop the minimum enstrophy theory applied to flows on the sphere with one constraint, either angular momentum or energy. Let μ_e denote the outer edge of the vorticity mixing region. Following Leith (1984) we first hypothesize that, out of the family of zonal flows which have the same integrated angular momentum north of $\mu = \mu_e$ and the same zonal wind at each latitude south of $\mu = \mu_e$, the zonal flow with minimum integrated enstrophy north of $\mu = \mu_e$ is the one toward which the flow actually evolves. This zonal flow is derived in section 4.2 and is called MinEF-$\mathcal{M}$, i.e., the minimum enstrophy flow with constrained angular momentum. As a second hypothesis we argue that, out of the family of zonal flows which have the same integrated energy north of $\mu = \mu_e$ and the same zonal wind at each latitude south of $\mu = \mu_e$, the flow with minimum integrated enstrophy north of $\mu = \mu_e$ is the one toward which the flow actually evolves. This vortex is called MinEF-$\mathcal{E}$, i.e., the minimum enstrophy flow with constrained energy, and is presented in section 4.3.

4.2 Minimum enstrophy flow with fixed angular momentum and one edge (MinEF-$\mathcal{M}$)

Let us assume that vorticity mixing is confined to a polar cap with unknown south edge μ_s. In the region $-1 \leq \mu \leq \mu_s$, the final zonally symmetric flow $U(\mu)$ is equal to the initial zonally symmetric flow $U_0(\mu)$ and the final absolute vorticity $\zeta(\mu)$ is equal to the initial absolute vorticity $\zeta_0(\mu)$. Requiring $U(\mu)$ to be a continuous function, we have

$$U(\mu_s) = U_0(\mu_s), \tag{4.9}$$

as the boundary condition on the final flow in the mixed region.

Given the conservation of total angular momentum, it is easy to show that maximizing the

absolute enstrophy deficit is equivalent to maximizing the relative enstrophy deficit, that is:

$$\int_{\mu_s}^{1} \tfrac{1}{2}(\zeta_0^2 - \zeta^2)d\mu = \int_{\mu_s}^{1} \tfrac{1}{2}(\zeta_{r0}^2 - \zeta_r^2)d\mu.$$

We will consider the first case (i.e., maximize the absolute enstrophy deficit) for the calculations in this chapter.

We now explore the hypothesis that the final flow can be found by maximizing the enstrophy deficit (relative to the initial enstrophy) subject to the constraint of angular momentum invariance, i.e.,

$$\text{maximize} \quad \int_{\mu_s}^{1} \tfrac{1}{2}(\zeta_0^2 - \zeta^2)d\mu, \tag{4.10}$$

subject to

$$\int_{\mu_s}^{1} (U_0 - U)d\mu = 0. \tag{4.11}$$

To solve this problem we now vary the mixing edge μ_s, the zonal wind profile $U(\mu)$ and the associated vorticity profile $\zeta(\mu)$ in search of that zonal flow which has maximum enstrophy deficit (i.e., minimum enstrophy) for fixed angular momentum. Since μ_s is unknown, its first variation is related to the first variation in U at that latitude by $\delta U(\mu_s) = [U_0'(\mu_s) - U'(\mu_s)]\,\delta\mu_s = -a\,[\zeta_0(\mu_s) - \zeta(\mu_s)]\,\delta\mu_s$ (e.g., Fox 1987, pages 210–213). Using this result, introducing the Lagrange multiplier $-\gamma$, and recalling Leibniz's rule, the variational problem is

$$\begin{aligned}
0 &= \delta \int_{\mu_s}^{1} \left[\tfrac{1}{2}(\zeta_0^2 - \zeta^2) - \gamma(U_0 - U)\right] d\mu \\
&= \int_{\mu_s}^{1} (-\zeta\delta\zeta + \gamma\delta U)\, d\mu - \tfrac{1}{2}\left[\zeta_0^2(\mu_s) - \zeta^2(\mu_s)\right]\delta\mu_s \\
&= \int_{\mu_s}^{1} \left(-\frac{d\zeta}{a d\mu} + \gamma\right) \delta U\, d\mu - \frac{1}{a}\zeta(\mu_s)\delta U(\mu_s) - \tfrac{1}{2}\left[\zeta_0^2(\mu_s) - \zeta^2(\mu_s)\right]\delta\mu_s \\
&= \int_{\mu_s}^{1} \left(-\frac{d\zeta}{a d\mu} + \gamma\right) \delta U\, d\mu - \tfrac{1}{2}\left[\zeta_0(\mu_s) - \zeta(\mu_s)\right]^2 \delta\mu_s,
\end{aligned} \tag{4.12}$$

where the third line follows from an integration by parts, along with the relation $a\delta\zeta = -d(\delta U)/d\mu$. For the independent variation $\delta\mu_s$, we obtain the transversality condition

$$\zeta(\mu_s) = \zeta_0(\mu_s). \tag{4.13}$$

For the independent variation δU, we obtain the Euler-Lagrange equation

$$\frac{d\zeta}{a d\mu} = \gamma \quad \text{for} \quad \mu_s \le \mu \le 1. \tag{4.14}$$

We can obtain the solutions for $\zeta(\mu)$ and $U(\mu)$ by first integrating (4.14) and enforcing the transversality condition (4.13), and then integrating $d[U+\Omega a(1-\mu^2)]/d\mu = -a\zeta$ and enforcing the boundary condition (4.9) and the condition $U(1) = 0$. We thus obtain

$$\zeta(\mu) = \zeta_0(\mu_s) + 2\left[\frac{U_0(\mu_s) + \Omega a(1-\mu_s^2)}{a(1-\mu_s)} - \zeta_0(\mu_s)\right]\left(\frac{\mu-\mu_s}{1-\mu_s}\right), \tag{4.15}$$

$$\begin{aligned} U(\mu) + \Omega a\left(1-\mu^2\right) &= \left[U_0(\mu_s) + \Omega a\left(1-\mu_s^2\right) - a\zeta_0(\mu_s)(1-\mu_s)\right]\left[1 - \left(\frac{\mu-\mu_s}{1-\mu_s}\right)^2\right] \\ &\quad + a\zeta_0(\mu_s)(1-\mu), \end{aligned} \tag{4.16}$$

for $\mu_s \le \mu \le 1$. Note that (4.16) satisfies the boundary condition (4.9). For given initial conditions $U_0(\mu)$ and $\zeta_0(\mu)$, the transcendental relation for the determination of the mixing edge μ_s is obtained by substituting (4.16) into the angular momentum constraint (4.11).

We can now summarize the argument for the minimum enstrophy zonal flow with constrained angular momentum. Given an initial unstable zonally symmetric flow with zonal wind $U_0(\mu)$ and vorticity $\zeta_0(\mu)$, first determine μ_s from (4.11) and (4.16). The final adjusted vorticity profile $\zeta(\mu)$ and zonal wind profile $U(\mu)$ are then given by (4.15) and (4.16).

Since $\int_{\mu_s}^1 \zeta d\mu = \int_{\mu_s}^1 \zeta_0 d\mu$ and $\int_{\mu_s}^1 \mu\zeta d\mu = \int_{\mu_s}^1 \mu\zeta_0 d\mu$, we can define a mean latitude $\bar{\mu}$ by

$$\bar{\mu} = \frac{\int_{\mu_s}^1 \mu\zeta d\mu}{\int_{\mu_s}^1 \zeta d\mu} = \frac{\int_{\mu_s}^1 \mu\zeta_0 d\mu}{\int_{\mu_s}^1 \zeta_0 d\mu}. \tag{4.17}$$

The mean latitude $\bar{\mu}$ is a measure of the dispersion of the vorticity about the equator. For MinEF-$\mathcal{M}$, $\bar{\mu}$ is strictly conserved from the initial to the final flow. Since $\bar{\mu}$ is so constrained, it is easy to see how a small equatorward mixing of vorticity by thinning troughs must be accompanied by a much larger poleward mixing of vorticity by polar vortex contraction.

4.2.1 Minimum enstrophy flow with fixed angular momentum and two edges (MinEF-$\mathcal{M}$)

Let us assume that vorticity mixing is confined to a zonal strip with unknown south edge μ_s and unknown north edge μ_n. In the regions $-1 \le \mu \le \mu_s$ and $\mu_n \le \mu \le 1$, the final zonally symmetric flow $U(\mu)$ is equal to the initial zonally symmetric flow $U_0(\mu)$ and the final vorticity $\zeta(\mu)$ is equal to the initial vorticity $\zeta_0(\mu)$. Requiring $U(\mu)$ to be a continuous function, we have

$$U(\mu_s) = U_0(\mu_s), \qquad U(\mu_n) = U_0(\mu_n) \tag{4.18}$$

as boundary conditions on the final flow in the mixed region.

We now explore the hypothesis that the final flow can be found by maximizing the enstrophy deficit (relative to the initial enstrophy) subject to the constraint of angular momentum invariance, i.e.,

$$\text{maximize} \quad \int_{\mu_s}^{\mu_n} \tfrac{1}{2}(\zeta_0^2 - \zeta^2) d\mu, \tag{4.19}$$

subject to

$$\int_{\mu_s}^{\mu_n} (U_0 - U) d\mu = 0. \tag{4.20}$$

To solve this problem we now vary the mixing edges μ_s and μ_n, the zonal wind profile $U(\mu)$ and the associated vorticity profile $\zeta(\mu)$ in search of that zonal flow which has maximum enstrophy deficit (i.e., minimum enstrophy) for fixed angular momentum. Since μ_s and μ_n are unknown, their first variations are related to the first variations in U at those latitudes by $\delta U(\mu_s) = [U_0'(\mu_s) - U'(\mu_s)]\,\delta\mu_s = -a\,[\zeta_0(\mu_s) - \zeta(\mu_s)]\,\delta\mu_s$ and $\delta U(\mu_n) = [U_0'(\mu_n) - U'(\mu_n)]\,\delta\mu_n = -a\,[\zeta_0(\mu_n) - \zeta(\mu_n)]\,\delta\mu_n$ (e.g., Fox 1987, pages 210–213). Using these results, introducing the Lagrange multiplier $-\gamma$, and recalling Leibniz's rule, the variational problem is

$$\begin{aligned}
0 &= \delta \int_{\mu_s}^{\mu_n} \left[\tfrac{1}{2}(\zeta_0^2 - \zeta^2) - \gamma(U_0 - U)\right] d\mu \\
&= \int_{\mu_s}^{\mu_n} (-\zeta\delta\zeta + \gamma\delta U)\, d\mu + \tfrac{1}{2}\left[\zeta_0^2(\mu_n) - \zeta^2(\mu_n)\right]\delta\mu_n - \tfrac{1}{2}\left[\zeta_0^2(\mu_s) - \zeta^2(\mu_s)\right]\delta\mu_s \\
&= \int_{\mu_s}^{\mu_n} \left(-\frac{d\zeta}{a d\mu} + \gamma\right)\delta U\, d\mu + \frac{1}{a}\zeta(\mu_n)\delta U(\mu_n) + \tfrac{1}{2}\left[\zeta_0^2(\mu_n) - \zeta^2(\mu_n)\right]\delta\mu_n \\
&\quad - \frac{1}{a}\zeta(\mu_s)\delta U(\mu_s) - \tfrac{1}{2}\left[\zeta_0^2(\mu_s) - \zeta^2(\mu_s)\right]\delta\mu_s \\
&= \int_{\mu_s}^{\mu_n} \left(-\frac{d\zeta}{a d\mu} + \gamma\right)\delta U\, d\mu + \tfrac{1}{2}\left[\zeta_0(\mu_n) - \zeta(\mu_n)\right]^2\delta\mu_n - \tfrac{1}{2}\left[\zeta_0(\mu_s) - \zeta(\mu_s)\right]^2\delta\mu_s,
\end{aligned} \tag{4.21}$$

where the third line follows from an integration by parts, along with the relation $a\delta\zeta = -d(\delta U)/d\mu$. For the independent variations $\delta\mu_s$ and $\delta\mu_n$, we obtain the transversality conditions

$$\zeta(\mu_s) = \zeta_0(\mu_s), \qquad \zeta(\mu_n) = \zeta_0(\mu_n). \tag{4.22}$$

For the independent variation δU, we obtain the Euler-Lagrange equation

$$\frac{d\zeta}{a d\mu} = \gamma \quad \text{for} \quad \mu_s \le \mu \le \mu_n. \tag{4.23}$$

Integrating (4.23) and enforcing the transversality conditions (4.22), we find that the final vorticity satisfies

$$\zeta(\mu) = \zeta_0(\mu_n)\left(\frac{\mu-\mu_s}{\mu_n-\mu_s}\right) + \zeta_0(\mu_s)\left(\frac{\mu_n-\mu}{\mu_n-\mu_s}\right) \qquad \text{for} \qquad \mu_s \le \mu \le \mu_n, \tag{4.24}$$

if the Lagrange multiplier γ takes on the value

$$\gamma = \frac{\zeta_0(\mu_n)-\zeta_0(\mu_s)}{a(\mu_n-\mu_s)}, \tag{4.25}$$

which is the constant vorticity gradient across the mixed region.

Since $d[U+\Omega a(1-\mu^2)]/d\mu = -a\zeta$, the solution for $U(\mu)$ can be written as

$$\begin{aligned} U(\mu)+\Omega a\left(1-\mu^2\right) &= \left[U_0(\mu_s)+\Omega a\left(1-\mu_s^2\right)\right]\left(\frac{\mu_n-\mu}{\mu_n-\mu_s}\right) \\ &\quad + \left[U_0(\mu_n)+\Omega a\left(1-\mu_n^2\right)\right]\left(\frac{\mu-\mu_s}{\mu_n-\mu_s}\right) \\ &\quad - \tfrac{1}{2}a\left[\frac{\zeta_0(\mu_n)-\zeta_0(\mu_s)}{\mu_n-\mu_s}\right]\left[\mu^2-(\mu_s+\mu_n)\mu+\mu_s\mu_n\right] \end{aligned} \tag{4.26}$$

for $\mu_s \le \mu \le \mu_n$. Note that (4.26) satisfies the boundary conditions (4.18). The linear vorticity function obtained by taking $d/d\mu$ of (4.26) has the same constant $d\zeta/d\mu$ value as given by (4.23) and (4.25). Requiring that (4.24) and (4.26) lead to consistent values of $\zeta(\mu)$ at one point in the mixing region (e.g., the point $\mu = \frac{1}{2}(\mu_s+\mu_n)$) leads to the relation

$$\tfrac{1}{2}\left[\zeta_0(\mu_s)+\zeta_0(\mu_n)\right] = \frac{\left[U_0(\mu_s)+\Omega a(1-\mu_s^2)\right]-\left[U_0(\mu_n)+\Omega a(1-\mu_n^2)\right]}{a(\mu_n-\mu_s)}. \tag{4.27}$$

For given initial conditions $U_0(\mu)$ and $\zeta_0(\mu)$, (4.27) constitutes one of the two transcendental relations required for the determination of the mixing edges μ_s and μ_n. The other relation is obtained by substituting (4.26) into the angular momentum constraint (4.20).

We can now summarize the argument for the minimum enstrophy zonal flow with constrained angular momentum. Given an initial unstable zonally symmetric flow with zonal wind $U_0(\mu)$ and vorticity $\zeta_0(\mu)$, first determine μ_s and μ_n from (4.20) and (4.27). The final adjusted vorticity profile $\zeta(\mu)$ and zonal wind profile $U(\mu)$ are then given by (4.24) and (4.26).

Since $\int_{\mu_s}^{\mu_n}\zeta d\mu = \int_{\mu_s}^{\mu_n}\zeta_0 d\mu$ and $\int_{\mu_s}^{\mu_n}\mu\zeta d\mu = \int_{\mu_s}^{\mu_n}\mu\zeta_0 d\mu$, we can define a mean latitude $\bar{\mu}$ by

$$\bar{\mu} = \frac{\int_{\mu_s}^{\mu_n}\mu\zeta d\mu}{\int_{\mu_s}^{\mu_n}\zeta d\mu} = \frac{\int_{\mu_s}^{\mu_n}\mu\zeta_0 d\mu}{\int_{\mu_s}^{\mu_n}\zeta_0 d\mu}. \tag{4.28}$$

The mean latitude $\bar{\mu}$ is a measure of the dispersion of the vorticity about the equator. For MinEF-$\mathcal{M}$, $\bar{\mu}$ is strictly conserved from the initial to the final flow.

4.3 Minimum enstrophy flow with fixed energy and one edge (MinEF-$\mathcal{E}$)

We assume that, in the region $-1 \leq \mu \leq \mu_s$, the final angular velocity $\omega(\mu)$ is equal to the initial angular velocity $\omega_0(\mu)$, so that in particular

$$\omega(\mu_s) = \omega_0(\mu_s). \tag{4.29}$$

We now explore the hypothesis that the final flow can be found by maximizing the enstrophy deficit subject to the constraint of kinetic energy invariance, i.e.,

$$\text{maximize} \quad \int_{\mu_s}^{1} \tfrac{1}{2}(\zeta_0^2 - \zeta^2) d\mu, \tag{4.30}$$

subject to

$$\int_{\mu_s}^{1} \tfrac{1}{2}(u_0^2 - u^2) d\mu = 0. \tag{4.31}$$

We now vary μ_s, the zonal wind profile $u(\mu)$ and the associated vorticity profile $\zeta(\mu)$ in search of that zonal flow which has maximum enstrophy deficit for fixed energy. Introducing the Lagrange multiplier β, the variational problem is

$$\begin{aligned}
0 &= \delta \int_{\mu_s}^{1} \tfrac{1}{2} \left[\zeta_0^2 - \zeta^2 + \beta(u_0^2 - u^2)\right] d\mu \\
&= -\int_{\mu_s}^{1} (\zeta \delta\zeta + \beta u \delta u)\, d\mu - \tfrac{1}{2} \left[\zeta_0^2(\mu_s) - \zeta^2(\mu_s)\right] \delta\mu_s \\
&= -\int_{\mu_s}^{1} (\zeta - \beta\psi)\, \delta\zeta\, d\mu - \frac{\beta}{a}\psi(\mu_s)\delta U(\mu_s) - \tfrac{1}{2} \left[\zeta_0^2(\mu_s) - \zeta^2(\mu_s)\right] \delta\mu_s \\
&= -\int_{\mu_s}^{1} (\zeta - \beta\psi)\, \delta\zeta\, d\mu - \tfrac{1}{2} \left[\zeta_0(\mu_s) + \zeta(\mu_s) - 2\beta\psi(\mu_s)\right] \left[\zeta_0(\mu_s) - \zeta(\mu_s)\right] \delta\mu_s,
\end{aligned} \tag{4.32}$$

where the third line of (4.32) results from an integration by parts. For the independent variation $\delta\mu_s$, we again obtain the transversality condition

$$\zeta(\mu_s) = \zeta_0(\mu_s). \tag{4.33}$$

For the independent variation $\delta\zeta$, we obtain $\zeta = -a^{-2}\alpha(\alpha+1)\psi$ for $\mu_s \leq \mu \leq 1$, where α is defined in terms of the Lagrange multiplier by $\alpha(\alpha+1) = -\beta a^2$. When written in terms of the streamfunction,

this linear relation between ζ and ψ takes the form

$$(1-\mu^2)\frac{d^2\psi}{d\mu^2} - 2\mu\frac{d\psi}{d\mu} + \alpha(\alpha+1)\psi = -2\Omega a^2\mu \quad \text{for} \quad \mu_s \le \mu \le 1. \tag{4.34}$$

The general solution of (4.34) is $\psi(\mu) = AP_\alpha(\mu) + BQ_\alpha(\mu) + 2\Omega a^2\mu/[2-\alpha(\alpha+1)]$, where $P_\alpha(\mu)$ and $Q_\alpha(\mu)$ are the Legendre functions of (noninteger) order α, and A and B are constants. The Legendre function $P_\alpha(\mu)$ is not finite at $\mu = -1$ while the Legendre function $Q_\alpha(\mu)$ is not finite at $\mu = 1$. Since we are considering mixing in the north polar cap, we set $B = 0$. Since $\zeta(\mu) = -a^{-2}\alpha(\alpha+1)\psi$, the solution for the vorticity is $\zeta(\mu) = -a^{-2}\alpha(\alpha+1)\left\{AP_\alpha(\mu) + 2\Omega a^2\mu/[2-\alpha(\alpha+1)]\right\}$. The constant A can now be obtained by enforcing the transversality condition (4.33). This results in

$$\zeta(\mu) = \left[\zeta_0(\mu_s) - \left(\frac{\alpha(\alpha+1)2\Omega\mu_s}{\alpha(\alpha+1)-2}\right)\right]\frac{P_\alpha(\mu)}{P_\alpha(\mu_s)} + \frac{\alpha(\alpha+1)2\Omega\mu}{\alpha(\alpha+1)-2} \tag{4.35}$$

for $\mu_s \le \mu \le 1$. Since the angular velocity is related to the streamfunction by $\omega(\mu) = -a^{-2}(d\psi/d\mu)$, we can also determine the constants A and B by enforcing (4.29). This results in

$$\omega(\mu) = \left[\omega_0(\mu_s) - \frac{2\Omega}{\alpha(\alpha+1)-2}\right]\frac{P'_\alpha(\mu)}{P'_\alpha(\mu_s)} + \frac{2\Omega}{\alpha(\alpha+1)-2}. \tag{4.36}$$

Because $\zeta(\mu)$ and $\omega(\mu)$ are related by $\zeta = 2\Omega\mu - d[(1-\mu^2)\omega]/d\mu$, consistency between (4.35) and (4.36) requires

$$\alpha(\alpha+1)\left[\omega_0(\mu_s) - \frac{2\Omega}{\alpha(\alpha+1)-2}\right]P_\alpha(\mu_s) = \left[\zeta_0(\mu_s) - \frac{\alpha(\alpha+1)2\Omega\mu_s}{\alpha(\alpha+1)-2}\right]P'_\alpha(\mu_s), \tag{4.37}$$

For given initial conditions $\omega_0(\mu)$ and $\zeta_0(\mu)$, (4.37) constitutes one of the two transcendental relations required for the determination of the mixing edge μ_s and the Lagrange multiplier α. The other relation is obtained by substituting (4.36) into the energy constraint (4.31).

We can summarize the MinEF-$\mathcal{E}$ argument as follows. Given an initial unstable zonal flow with angular velocity $\omega_0(\mu)$ and vorticity $\zeta_0(\mu)$, first determine α, and μ_s from (4.31) and (4.37). The final adjusted vorticity profile $\zeta(\mu)$ and angular velocity profile $\omega(\mu)$ are then given by (4.35) and (4.36).

4.3.1 Minimum enstrophy flow with fixed energy and two edges (MinEF-$\mathcal{E}$)

We assume that, in the regions $-1 \leq \mu \leq \mu_s$ and $\mu_n \leq \mu \leq 1$, the final angular velocity $\omega(\mu)$ is equal to the initial angular velocity $\omega_0(\mu)$, so that in particular

$$\omega(\mu_s) = \omega_0(\mu_s), \qquad \omega(\mu_n) = \omega_0(\mu_n). \tag{4.38}$$

We now explore the hypothesis that the final flow can be found by maximizing the enstrophy deficit subject to the constraint of kinetic energy invariance, i.e.,

$$\text{maximize} \quad \int_{\mu_s}^{\mu_n} \tfrac{1}{2}(\zeta_0^2 - \zeta^2) d\mu, \tag{4.39}$$

subject to

$$\int_{\mu_s}^{\mu_n} \tfrac{1}{2}(u_0^2 - u^2) d\mu = 0. \tag{4.40}$$

We now vary μ_s, μ_n, the zonal wind profile $u(\mu)$ and the associated vorticity profile $\zeta(\mu)$ in search of that zonal flow which has maximum enstrophy deficit for fixed energy. Introducing the Lagrange multiplier β, the variational problem is

$$\begin{aligned}
0 &= \delta \int_{\mu_s}^{\mu_n} \tfrac{1}{2} \left[\zeta_0^2 - \zeta^2 + \beta(u_0^2 - u^2)\right] d\mu \\
&= -\int_{\mu_s}^{\mu_n} (\zeta \delta\zeta + \beta u \delta u)\, d\mu + \tfrac{1}{2}\left[\zeta_0^2(\mu_n) - \zeta^2(\mu_n)\right] \delta\mu_n - \tfrac{1}{2}\left[\zeta_0^2(\mu_s) - \zeta^2(\mu_s)\right] \delta\mu_s \\
&= -\int_{\mu_s}^{\mu_n} (\zeta - \beta\psi)\, \delta\zeta\, d\mu + \frac{\beta}{a}\left[\psi(\mu_n)\delta U(\mu_n) - \psi(\mu_s)\delta U(\mu_s)\right] \\
&\quad + \tfrac{1}{2}\left[\zeta_0^2(\mu_n) - \zeta^2(\mu_n)\right] \delta\mu_n - \tfrac{1}{2}\left[\zeta_0^2(\mu_s) - \zeta^2(\mu_s)\right] \delta\mu_s \\
&= -\int_{\mu_s}^{\mu_n} (\zeta - \beta\psi)\, \delta\zeta\, d\mu + \tfrac{1}{2}\left[\zeta_0(\mu_n) + \zeta(\mu_n) - 2\beta\psi(\mu_n)\right]\left[\zeta_0(\mu_n) - \zeta(\mu_n)\right] \delta\mu_n \\
&\quad - \tfrac{1}{2}\left[\zeta_0(\mu_s) + \zeta(\mu_s) - 2\beta\psi(\mu_s)\right]\left[\zeta_0(\mu_s) - \zeta(\mu_s)\right] \delta\mu_s,
\end{aligned} \tag{4.41}$$

where the third line of (4.41) results from an integration by parts. For the independent variations $\delta\mu_s$ and $\delta\mu_n$, we again obtain the transversality conditions

$$\zeta(\mu_s) = \zeta_0(\mu_s), \qquad \zeta(\mu_n) = \zeta_0(\mu_n). \tag{4.42}$$

For the independent variation $\delta\zeta$, we obtain $\zeta = -a^{-2}\alpha(\alpha+1)\psi$ for $\mu_s \leq \mu \leq \mu_n$, where α is defined in terms of the Lagrange multiplier by $\alpha(\alpha+1) = -\beta a^2$. When written in terms of the

streamfunction, this linear relation between ζ and ψ takes the form

$$(1-\mu^2)\frac{d^2\psi}{d\mu^2} - 2\mu\frac{d\psi}{d\mu} + \alpha(\alpha+1)\psi = -2\Omega a^2\mu \quad \text{for} \quad \mu_s \le \mu \le \mu_n. \tag{4.43}$$

The general solution of (4.43) is $\psi(\mu) = AP_\alpha(\mu) + BQ_\alpha(\mu) + 2\Omega a^2\mu/[2-\alpha(\alpha+1)]$, where $P_\alpha(\mu)$ and $Q_\alpha(\mu)$ are the Legendre functions of (noninteger) order α, and A and B are constants. The Legendre function $P_\alpha(\mu)$ is not finite at $\mu = -1$ while the Legendre function $Q_\alpha(\mu)$ is not finite at $\mu = 1$. If $-1 < \mu_s$ and $\mu_n < 1$, both Legendre functions are needed in the construction of the general solution to (4.43). Since $\zeta(\mu) = -a^{-2}\alpha(\alpha+1)\psi$, the general solution for the vorticity is $\zeta(\mu) = -a^{-2}\alpha(\alpha+1)\left\{AP_\alpha(\mu) + BQ_\alpha(\mu) + 2\Omega a^2\mu/[2-\alpha(\alpha+1)]\right\}$. The constants A and B can now be obtained by enforcing the transversality conditions (4.42). This results in

$$\begin{aligned}
\zeta(\mu) &= \left[\zeta_0(\mu_n) - \left(\frac{\alpha(\alpha+1)2\Omega\mu_n}{\alpha(\alpha+1)-2}\right)\right]\left[\frac{Q_\alpha(\mu_s)P_\alpha(\mu) - P_\alpha(\mu_s)Q_\alpha(\mu)}{Q_\alpha(\mu_s)P_\alpha(\mu_n) - P_\alpha(\mu_s)Q_\alpha(\mu_n)}\right] \\
&+ \left[\zeta_0(\mu_s) - \left(\frac{\alpha(\alpha+1)2\Omega\mu_s}{\alpha(\alpha+1)-2}\right)\right]\left[\frac{P_\alpha(\mu_n)Q_\alpha(\mu) - Q_\alpha(\mu_n)P_\alpha(\mu)}{P_\alpha(\mu_n)Q_\alpha(\mu_s) - Q_\alpha(\mu_n)P_\alpha(\mu_s)}\right] \\
&+ \frac{\alpha(\alpha+1)2\Omega\mu}{\alpha(\alpha+1)-2},
\end{aligned} \tag{4.44}$$

for $\mu_s \le \mu \le \mu_n$. Since the angular velocity is related to the streamfunction by $\omega(\mu) = -a^{-2}(d\psi/d\mu)$, we can also determine the constants A and B by enforcing (4.38). This results in

$$\begin{aligned}
\omega(\mu) &= \left[\omega_0(\mu_n) - \frac{2\Omega}{\alpha(\alpha+1)-2}\right]\left[\frac{Q'_\alpha(\mu_s)P'_\alpha(\mu) - P'_\alpha(\mu_s)Q'_\alpha(\mu)}{Q'_\alpha(\mu_s)P'_\alpha(\mu_n) - P'_\alpha(\mu_s)Q'_\alpha(\mu_n)}\right] \\
&+ \left[\omega_0(\mu_s) - \frac{2\Omega}{\alpha(\alpha+1)-2}\right]\left[\frac{P'_\alpha(\mu_n)Q'_\alpha(\mu) - Q'_\alpha(\mu_n)P'_\alpha(\mu)}{P'_\alpha(\mu_n)Q'_\alpha(\mu_s) - Q'_\alpha(\mu_n)P'_\alpha(\mu_s)}\right] \\
&+ \frac{2\Omega}{\alpha(\alpha+1)-2}.
\end{aligned} \tag{4.45}$$

Because $\zeta(\mu)$ and $\omega(\mu)$ are related by $\zeta = 2\Omega\mu - d[(1-\mu^2)\omega]/d\mu$, consistency between (4.44) and (4.45) requires

$$\alpha(\alpha+1)\left[\frac{P_\alpha(\mu_n)Q_\alpha(\mu_s) - P_\alpha(\mu_s)Q_\alpha(\mu_n)}{P'_\alpha(\mu_n)Q'_\alpha(\mu_s) - P'_\alpha(\mu_s)Q'_\alpha(\mu_n)}\right] = \left[\frac{C(\mu_n)Q_\alpha(\mu_s) - C(\mu_s)Q_\alpha(\mu_n)}{D(\mu_n)Q'_\alpha(\mu_s) - D(\mu_s)Q'_\alpha(\mu_n)}\right], \tag{4.46}$$

$$\alpha(\alpha+1)\left[\frac{P_\alpha(\mu_n)Q_\alpha(\mu_s) - P_\alpha(\mu_s)Q_\alpha(\mu_n)}{P'_\alpha(\mu_n)Q'_\alpha(\mu_s) - P'_\alpha(\mu_s)Q'_\alpha(\mu_n)}\right] = \left[\frac{C(\mu_n)P_\alpha(\mu_s) - C(\mu_s)P_\alpha(\mu_n)}{D(\mu_n)P'_\alpha(\mu_s) - D(\mu_s)P'_\alpha(\mu_n)}\right], \tag{4.47}$$

where

$$C(\mu) = \zeta_0(\mu) - \frac{\alpha(\alpha+1)2\Omega\mu}{\alpha(\alpha+1)-2}, \tag{4.48}$$

$$D(\mu) = \omega_0(\mu) - \frac{2\Omega}{\alpha(\alpha+1)-2}. \tag{4.49}$$

For given initial conditions $\omega_0(\mu)$ and $\zeta_0(\mu)$, (4.46) and (4.47) constitute two of the three transcendental relations required for the determination of the mixing edges μ_s and μ_n and the Lagrange multiplier α. The other relation is obtained by substituting (4.45) into the energy constraint (4.40).

We can summarize the MinEF-$\mathcal{E}$ argument as follows. Given an initial unstable zonal flow with angular velocity $\omega_0(\mu)$ and vorticity $\zeta_0(\mu)$, first determine α, μ_s and μ_n from (4.40), (4.46) and (4.47). The final adjusted vorticity profile $\zeta(\mu)$ and angular velocity profile $\omega(\mu)$ are then given by (4.44) and (4.45).

4.4 Second variation and verification of minimum

The solutions for the MinEF-$\mathcal{M}$ and MinEF-$\mathcal{E}$ presented above correspond to stationary points, which may be maxima, saddle-points or minima. After satisfying the conditions for a stationary value (that is, first variation equal to zero), the further criterion for an extremum depends on the sign of the second variation. An extremum requires that the sign of the second variation shall remain the same for any possible infinitesimal virtual displacements, positive for a minimum, negative for a maximum. If the sign of the second variation is positive for some displacements and negative for others, then the stationary value of the function does not yield an extremum.

4.4.1 Second variation MinEF-$\mathcal{M}$

In order to determine if the solutions given by (4.15) and (4.16) for the MinEF-$\mathcal{M}$ with one edge correspond to a real minimum enstrophy flow (or maximum enstrophy deficit), we explore the second variation of the enstrophy deficit (4.10) subject to the angular momentum constraint (4.11). Defining $\delta^2\mathcal{Z}_d$ as

$$\delta^2\mathcal{Z}_d \equiv \delta^2 \int_{\mu_s}^{1} \tfrac{1}{2}(\zeta_0^2 - \zeta^2)d\mu - \gamma\delta^2 \int_{\mu_s}^{1} (U_0 - U)d\mu. \tag{4.50}$$

Then, using (4.12)

$$\begin{aligned}\delta^2\mathcal{Z}_d \;=\; & \int_{\mu_s}^{1} -\frac{d\delta\zeta}{ad\mu}\delta U\, d\mu + \int_{\mu_s}^{1}\left(-\frac{d\zeta}{ad\mu}+\gamma\right)\delta^2 U\, d\mu + \left(-\frac{d\zeta}{ad\mu}(\mu_s)+\gamma\right)\delta U(\mu_s)\delta\mu_s \\ & + [\zeta_0(\mu_s)-\zeta(\mu_s)]\,\delta\zeta(\mu_s)\delta\mu_s - \tfrac{1}{2}\left[\zeta_0(\mu_s)-\zeta(\mu_s)\right]^2\delta^2\mu_s.\end{aligned} \tag{4.51}$$

Terms inside the big parentheses in (4.51) are equal to zero because of (4.14), while from (4.13) terms in brackets are also equal to zero. Then

$$\delta^2 \mathcal{Z}_d = \int_{\mu_s}^{1} \left(-\frac{d\delta\zeta}{a d\mu} \right) \delta U \, d\mu. \tag{4.52}$$

Using the relation $a\delta\zeta = -d(\delta U)/d\mu$ and integrating by parts we obtain

$$\begin{aligned} \delta^2 \mathcal{Z}_d &= \int_{\mu_s}^{1} \left(\frac{d^2\delta U}{a^2 d\mu^2} \right) \delta U \, d\mu \\ &= \delta U(\mu = 1) \frac{d\delta U}{a^2 d\mu}(\mu = 1) - \delta U(\mu_s) \frac{d\delta U}{a^2 d\mu}(\mu_s) \\ &\quad - \int_{\mu_s}^{1} \left(\frac{d\delta U}{a d\mu} \right)^2 d\mu. \end{aligned} \tag{4.53}$$

Since $\delta U(\mu_s) = [U_0'(\mu_s) - U'(\mu_s)]\,\delta\mu_s = -a\,[\zeta_0(\mu_s) - \zeta(\mu_s)]\,\delta\mu_s = 0$ and $\delta U(\mu = 1) = 0$, we finally get

$$\delta^2 \mathcal{Z}_d = -\int_{\mu_s}^{1} \left(\frac{d\delta U}{a d\mu} \right)^2 d\mu = -\int_{\mu_s}^{1} (\delta\zeta)^2 \, d\mu \leq 0. \tag{4.54}$$

Therefore, for an arbitrary and continuous variation from the solution given by (4.15) which has any nonzero value in the interval from μ_s to 1, we have a maximum enstrophy deficit, or minimum enstrophy flow (see Schubert et al. 1999, footnote number 7).

In a similar way we can derive the second variation of enstrophy deficit subject to the angular momentum constraint for the case with two edges, obtaining

$$\delta^2 \mathcal{Z}_d = -\int_{\mu_s}^{\mu_n} \left(\frac{d\delta U}{a d\mu} \right)^2 d\mu = -\int_{\mu_s}^{\mu_n} (\delta\zeta)^2 \, d\mu \leq 0. \tag{4.55}$$

4.4.2 Second variation MinEF-$\mathcal{E}$

Now we explore the second variation for the minimum enstrophy flow with the energy constraint and one edge, corresponding to the solution given by (4.35) and (4.36). The second variation of the enstrophy deficit (4.30) with the energy constraint (4.31) is given by

$$\delta^2 \mathcal{Z}_d \equiv \delta^2 \int_{\mu_s}^{1} \tfrac{1}{2}(\zeta_0^2 - \zeta^2) d\mu + \beta\delta^2 \int_{\mu_s}^{1} \tfrac{1}{2}(u_0^2 - u^2) d\mu, \tag{4.56}$$

which is equivalent to take the variation of the right hand side of equation (4.32), that is

$$\begin{aligned}
\delta^2 \mathcal{Z}_d &= -\int_{\mu_s}^{1} (\zeta - \beta\psi)\, \delta^2\zeta \, d\mu - \int_{\mu_s}^{1} (\delta\zeta - \beta\delta\psi)\, \delta\zeta \, d\mu \\
&+ \left[\zeta(\mu_s) - \beta\psi(\mu_s)\right] \delta\mu_s - \tfrac{1}{2}\left[\zeta_0(\mu_s) + \zeta(\mu_s) - 2\beta\psi(\mu_s)\right]\left[\delta(\zeta_0(\mu_s) - \zeta(\mu_s))\right]\delta\mu_s \\
&- \tfrac{1}{2}\delta\left[\zeta_0(\mu_s) + \zeta(\mu_s) - 2\beta\psi(\mu_s)\right]\left[\zeta_0(\mu_s) - \zeta(\mu_s)\right]\delta\mu_s \\
&- \tfrac{1}{2}\left[\zeta_0(\mu_s) + \zeta(\mu_s) - 2\beta\psi(\mu_s)\right]\left[\zeta_0(\mu_s) - \zeta(\mu_s)\right]\delta^2\mu_s. \qquad (4.57)
\end{aligned}$$

With the aid of (4.33) and the fact that from the first variation $\zeta(\mu) = \beta\psi(\mu)$ for $\mu_s \leq \mu \leq 1$, (4.57) simplifies to

$$\delta^2 \mathcal{Z}_d = -\int_{\mu_s}^{1} (\delta\zeta)^2 - \beta\delta\psi\delta\zeta \, d\mu. \qquad (4.58)$$

Using the relation $a\delta\zeta = -d(\delta U)/d\mu$ and integrating by parts we obtain

$$\begin{aligned}
\delta^2 \mathcal{Z}_d &= -\int_{\mu_s}^{1} \left((\delta\zeta)^2 + \beta\delta\psi \frac{d(\delta U)}{a d\mu} \right) d\mu \\
&= -\int_{\mu_s}^{1} (\delta\zeta)^2 \, d\mu - \frac{\beta}{a}\delta\psi(\mu = 1)\delta U(\mu = 1) + \frac{\beta}{a}\delta\psi(\mu_s)\delta U(\mu_s) \\
&+ \int_{\mu_s}^{1} \beta \frac{d(\delta\psi)}{a d\mu}\delta U \, d\mu. \qquad (4.59)
\end{aligned}$$

Since $\delta U(\mu_s) = \left[U_0'(\mu_s) - U'(\mu_s)\right]\delta\mu_s = -a\left[\zeta_0(\mu_s) - \zeta(\mu_s)\right]\delta\mu_s = 0$ and $\delta U(\mu = 1) = 0$, we get

$$\delta^2 \mathcal{Z}_d = -\int_{\mu_s}^{1} (\delta\zeta)^2 + \beta(\delta u)^2 \, d\mu, \qquad (4.60)$$

where we have used the fact that $U(\mu) = u(\mu)(1-\mu^2)^{1/2}$ and $u(\mu) = -(1-\mu^2)^{1/2} d\psi/a d\mu$. From (4.60) and recalling that $\beta = -\alpha(\alpha+1)/a^2$, we conclude that if $\beta \geq 0$ and there is any first variation of either ζ or u, then $\delta^2 \mathcal{Z}_d < 0$. Thus, if $\beta \geq 0$, the solution defined by (4.35) and (4.36) corresponds to a maximum enstrophy deficit or a minimum enstrophy flow.

In a similar way we can derive the second variation of enstrophy deficit subject to the energy constraint for the case with two edges, obtaining

$$\delta^2 \mathcal{Z}_d = -\int_{\mu_s}^{\mu_n} (\delta\zeta)^2 + \beta(\delta u)^2 \, d\mu. \qquad (4.61)$$

Chapter 5

STRATOSPHERIC POLAR VORTEX

5.1 Introduction

The atmosphere is usually divided into four regions according to the vertical profile of global-mean temperature. The stratosphere is the region which extends from the tropopause to an altitude of about 48 km (1 mb). This region is characterized by an increase of temperature with height and, when compared with the troposphere, a high stratification, having therefore weaker vertical motions.

The dynamic circulation of the stratosphere is strongly influenced by the seasonal cycle. In the summer hemisphere there is an easterly zonal-mean wind, while in the winter hemisphere the zonal-mean wind is westerly and is usually called the "polar night jet". The change from winter westerlies to summer easterlies occurs, on average, during March-April in the north and during October-November in the south. Another characteristic of the stratosphere is that geographically fixed planetary-scale wave patterns are observed primarily in the northern winter.

Many important contributions to the study of the dynamical behaviour of the stratosphere have been made since the early 1960's. Charney and Drazin (1961) derived a linear theory of the vertical propagation of disturbances on a mean zonal flow which is a function only of height. Their results show that if the mean zonal flow is westerly, only the long wavelength Rossby waves can propagate vertically. This is a plausible explanation of why long planetary-scale waves dominate the stratospheric circulation.

Charney and Stern (1962) described the formation of the polar vortex during the fall as a consequence of the absence of heating at high latitudes, combined with intense ozone absorption of sunlight at lower latitudes and lack of meridional heat exchange, producing strong stratospheric temperature gradients near latitude 60^o and a wind maximum at a height of about 60 km. Fig. 5.1 shows the zonal mean wind in the Southern Hemisphere during August 1979 and a smoothed representation of the meridional gradient of quasi-geostrophic potential vorticity during the same period. Note the regions of small or negative potential vorticity gradient at about 40°S and 70°S on the flanks of the polar night jet stream. Hartmann (1983) argued that these regions of large positive zonal wind curvature or small potential vorticity gradient are continually forced by radiative processes. The existence of regions where there is a zero in the gradient of absolute vorticity is a necesary condition for the instability of a zonal wind profile as shown by Kuo (1949).

Matsuno (1970) studied numerical solutions of the linearized equation for vertical wave propagation of perturbations superimposed on a basic zonal wind, taking the observed 500 mb monthly mean as the lower boundary condition. In this study Matsuno concluded that the planetary-scale disturbances in the stratosphere are upward extensions of those driven in the troposphere.

One phenomenon that occurs in the northern hemisphere stratosphere is what is known as sudden warming, which has been observed on average about once every other winter. Matsuno (1971) has enumerated as characteristics of sudden warmings: the distortion and breakdown of the polar vortex, sudden warming of the polar air and the appearance of circumpolar easterly winds after the weakening and disappearance of the polar night westerly jet. Matsuno (1971) used a linear model of the interaction of vertically propagating planetary waves in zonal winds to explain the sudden warmings; his conclusions are that anomalously intense vertically propagating waves have an interaction with the westerly jet, decelerating it and causing the sudden warming as described above. However, some discrepancies of his model with observations were noted, and he pointed out the need for a fully nonlinear treatment of the planetary wave propagation.

Matsuno (1971) as well as McIntyre (1982) suggested that shear instabilities, either barotropic or baroclinic, and critical layers could play an important role in the initiation of stratospheric sudden

warmings. Critical layers can be defined as those regions in the atmosphere where the phase speed of incident waves is equal to the speed of the basic state flow. As a wave (e.g., Rossby wave) approaches a critical layer, its amplitude will increase, its group velocity will decrease and irreversible shredding and mixing of the vorticity field will occur (see, e.g., Killworth and McIntyre, 1985).

McIntyre and Palmer (1983, 1984) presented synoptic-scale isentropic maps of Ertel's potential vorticity Q, for the northern middle stratosphere, illustrating how advective processes tend to produce Q fields of increasing intricacy. In these works, McIntyre and Palmer used the analogy of the breaking ocean waves approaching a beach with what was observed in the synoptic maps of Q, talking then of "breaking" Rossby or planetary waves. The criteria they used to differentiate a breaking planetary wave is whether material contours and surfaces are irreversibly deformed, rather than just undulating back and forth as in linear wave theory. Their conclusions were that, in the region around the main polar vortex, planetary waves are breaking most of the time, and that the resulting quasi-horizontal mixing is a possible explanation for the weak gradients that are observed in that area. In their view, major warmings are wave events that completely break up the polar vortex, advecting lower potential vorticity air poleward.

Hartmann (1983) studied barotropically unstable zonal flows, similar to those observed in the wintertime stratospheric circulation. He computed unstable modes of the linear barotropic vorticity equation associated with a negative potential vorticity gradient for two cases: 1) the polar side of the westerly jet and, 2) on the equatorward flank of the jet. For case 1 the most unstable wavenumbers were 1 and 2 with growth rates of 3-4 and 1.5-2 days respectively; for case 2, the most unstable wavenumbers were 1-3 with growth rates on the order of a week or more for wavenumbers 1 and 2. Based on these results, Hartmann suggested that vertical propagation of tropospheric waves could have important interactions with the barotropic instability of the polar vortex, causing then wave growth.

Juckes and McIntyre (1987) indicated that, when studying the stratospheric circulation, the breakdown of linear wave theory can be produced by the decrease of mass density encountered by the waves as they propagate upward and, when an equatorward wave propagation is present, the

weakening of the zonal winds. They simulated planetary wave breaking with numerical integrations of a one-layer hemispheric nonlinear model, showing a chaotic evolution of the "surf" zone, while the main vortex remains as a distinct material entity with very little transport into it and some area reduction due to erosion processes; they hypothesized that the portion of the vortex which survives erosion will behave as a chemically isolated material entity, even in the presence of substantial wave breaking, creating then, in their terminology, a "containment vessel".

McIntyre (1989), making reference to the numerical simulations of Juckes and McIntyre (1987), noted that the main part of the vortex is surrounded by a narrow edge of very steep potential vorticity gradients that acts like a barrier, sealing off the interior of the vortex from external intrusions of air. He concluded that this isolation of material within the polar vortex could be an important factor in the chemical destruction of ozone which has been observed inside the polar vortex during the spring, noting also that any "leakage" across the potential vorticity barrier will be important for the chemistry within the vortex.

Bowman (1993a) used Lagrangian tracer analysis in an equivalent barotropic model to study quasi-horizontal mixing by the large scale flow in the stratosphere during the Southern Hemisphere spring. He found that mixing occurred close to the critical lines of waves that were forced at the lower boundary, finding also that the interior of the polar vortex can become a critical region where wave forcing is capable of causing vortex breakdown and mixing of the whole vortex interior.

Bowman and Mangus (1993) presented Total Ozone Mapping Spectrometer (TOMS) images during the Southern Hemisphere spring, showing, on the equatorward side of the polar vortex, folding and stretching of the ozone field, qualitatively similar to the wave breaking of Ertel's potential vorticity (McIntyre and Palmer, 1983,1984). Figure 5.2 is a sequence of TOMS images from October 1983 taken from Bowman and Mangus (1993). The ozone hole is the dark region centered over the South Pole; it is surrounded by a region of higher ozone values shown in white; stretching and folding of the ozone field is observed, which gives us information about the dynamical processes occurring during that time period. Figure 5.3 shows another sequence of TOMS images which are typical of the breakdown of the polar vortex and the mixing of ozone over an extended region, with the

consequent disappearance of the ozone hole. Based on different structures present in TOMS images, Bowman and Mangus (1993) suggested that deformations of the ozone field are relatively deep and barotropic.

Bowman (1993b) diagnosed mixing and transport of air using Lagrangian dispersion statistics of tracer trajectories. These trajectories were computed from winds derived of the analysis of observed geopotential fields. His results showed that at the level of 450 K and above, there is little exchange of air across the polar vortex boundary before the vortex breakdown. At the levels of 400 and 425 K, mixing was greater, with considerable exchange of air between the middle latitudes and the vortex interior. During the vortex breakdown, strong mixing of vortex air with middle latitudes took place.

Bowman (1995) used a kinematic model of breaking waves to study the displacement of fluid particles. Based upon his results, an alternative view of mixing barriers is that they are the result of the absence of waves with phase speeds matching the basic state speed of the polar vortex flow. Therefore, the high wind maximum of the jet and the absence of waves with comparable phase speeds produce the barrier. This hypothesis was tested by Bowman (1996) using Lagrangian trajectories derived from Southern Hemisphere stratospheric winds, finding that, during winter, important mixing was restricted to the surf zone, and that a region near the polar vortex core, where a maximum potential vorticity gradient was approximately located, behaved as a mixing barrier. He argued that the absence of critical lines for propagating waves was the cause of the observed mixing barrier, as well as the relatively high potential vorticity gradient which provides a significant Rossby wave restoring mechanism.

5.2 Experiments

As an initial condition to model the behaviour of a polar vortex we have selected two types of zonally symmetric jet profiles which are those used by Hartmann (1983) and Ishioka and Yoden (1994):

tanh-type jet:

$$u_0(\phi) = \frac{U}{2}\cos\phi\left(1+\tanh\frac{\phi-\phi_0}{B}\right), \tag{5.1}$$

sech-type jet:

$$u_0(\phi) = U \cos\phi \, \mathrm{sech} \frac{2(\phi - \phi_0)}{B}, \tag{5.2}$$

where U is a measure of the intensity of the jet, ϕ_0 the position of it, and B the width of it.

In this chapter we will discuss the linear stability analysis, direct numerical integration and final equilibrium state of two experiments using the tanh type jet and two experiments using the sech type jet.

5.2.1 Experiment 1

This experiment is a tanh type jet given by equation (5.1) with the following values of the parameters: $U = 180\mathrm{ms}^{-1}$, $\phi_0 = 45^o\mathrm{N}$, $B = 6^o$, which corresponds to the experiment reported by Ishioka and Yoden (1994) in their Fig. 6b. The corresponding absolute vorticity is given by

$$\zeta_0(\phi) = \frac{U}{a}\left[\left(1 + \tanh\frac{\phi - \phi_0}{B}\right)\sin\phi - \frac{\left(\mathrm{sech}\frac{\phi-\phi_0}{B}\right)^2 \cos\phi}{2B}\right] + 2\Omega\sin\phi, \tag{5.3}$$

with a and Ω the Earth's radius and rotation rate respectively.

A plot of the initial absolute vorticity $\zeta_0(\phi)$ is shown in Fig. 5.4, together with a discretized version consisting of 60 vorticity levels to be used as initial condition for the maximum entropy prediction. The absolute vorticity profile $\zeta_0(\phi)$ in the Southern Hemisphere is basically given by the Earth's vorticity $f = 2\Omega\sin\phi$, while in the northern hemisphere it has a relative maximum at 32.8°N and a relative minimum at 43.7°N, satisfying Kuo's (1949) necessary condition for barotropic instability, i.e., a zero in the absolute vorticity gradient.

A linear stability analysis of this jet is performed using the theory presented in section 2.1. The results for the complex frequencies σ of the most unstable mode as a function of zonal wavenumber m is presented in Fig. 5.5, and the e-folding time $\tau_i = 1/Im(\sigma)$ and period $\tau_r = 2\pi/Re(\sigma)$ is summarized in Table 5.1 together with the results for the other three experiments of this chapter.

The most unstable zonal wavenumber for experiment 1 is wavenumber 4 with an e-folding time of $\tau_i = 0.774$ days and period $\tau_r = 2.02$ days, which is consistent with the values reported by Ishioka

and Yoden (1994) in their Table 2. Wavenumbers 1 and 7 are stable. Wavenumbers 3 and 4 have comparable values of the e-folding time τ_i.

The non-linear barotropic nondivergent model described in section 2.2 is used to study the evolution of the vorticity field given by (5.3) plus a disturbance of the form

$$\zeta_d(\lambda,\phi) = c_1 \left(e^{c_2(g(\lambda,\phi)-1)} - \frac{1-e^{-2c_2}}{2c_2} \right); \tag{5.4}$$

where

$$g(\lambda,\phi) = \sin\phi \ \sin\phi_d + \cos\phi \ \cos\phi_d \ \cos(\lambda-\lambda_d). \tag{5.5}$$

Here $c_1 = 0.01\Omega$ and $c_2 = 100$, which are measures of the intensity and horizontal extent of the disturbance, respectively. $\zeta_d(\lambda,\phi)$ is the same disturbance chosen by Ishioka and Yoden (1994) which is a Gaussian-like smooth function on a sphere and has nearly white spectra in the wavenumber space for large c_2; the disturbance is centered at $(\lambda_d,\phi_d) = (0,\frac{\pi}{4})$. The same $\zeta_d(\lambda,\phi)$ will be included for the study of the nonlinear time integration in all the experiments of this chapter.

Numerical integration is performed using a triangular truncation of $M = 150$, $\nu = 2.23 \times 10^{14}\mathrm{m}^4\mathrm{s}^{-1}$, and a timestep of 300s. The value of the hyperdifussion coefficient ν is obtained empirically via a preliminary set of runs, and corresponds to an e-folding time of the highest wavenumber $n = 150$ of $\tau_{150} = 4$ hours as mentioned in section 2.3.

Figure 5.6a is a Northern Hemisphere polar stereographic projection of the initial ($t = 0$) absolute vorticity field. Latitude $\lambda = 0$ corresponds to the straight line that runs from the North Pole upward on the page. This run includes the computation of 1000 air parcel trajectories initially uniformily distributed in two latitudinal rings, 500 of them corresponding to the relative maximum of the vorticity field ($\phi = 32.8^o$N) shown in red, and other 500 green parcels located at the relative minimum of ζ at $\phi = 43.7^o$N.

At $t = 4.5$ days (Fig. 5.6b) the deformation of the initially circular contours is evident, creating two folds of the vorticity contours of the "cat's eye" type (Killworth and McIntyre, 1985). At $t = 6$ days (Fig. 5.6c) vorticity contours are folded creating four pools of relatively lower vorticity which contain a big number of green parcels, while filamentation of the vortex edge (defined here as the

region with the maximum absolute vorticity gradient) takes place. A strong deformation of the region of red particles is evident, with a tendency for these parcels to approach the vortex edge.

At $t = 8.0$ days two pools of green parcels have merged and a triangular shape of the polar vortex edge has arisen with long vorticity filaments coming out of the vertices. At this time most of the red parcels have been advected poleward close to the vortex edge. At $t = 12$ days the polar vortex edge has an elliptical shape indicating a strong restoring mechanism towards axisymmetry after the deformations suffered at earlier times. On the other hand, the vortices which contain green parcels become elongated and begin to diffuse out and mix at low latitudes. This process continues at later times.

This simulation stops at $t = 100$ days (Fig. 5.6f) where a zonal symmetry is clear, specially at high latitudes. The polar vortex is almost centered at the North Pole surrounded by a region where red parcels are preferentially located over green parcels, while a ring of green parcels is evident in the region between 10^oN and 20^oN. Note that inside the polar vortex edge there are few colored air parcels, meaning that the core of the polar vortex has behaved as an isolated region from midlatitude air intrusions.

Tracer positions as a function of latitude at $t = 100$ days are shown in Fig. 5.7a. The counting is done within 5^o latitude rings dividing by the total number of parcels (500) of each color. The maximum of green tracers is located between $15^o - 20^o$N, south of their initial position at 43.7^oN. The maximum of red parcels is between $45^o - 50^o$N, north of their initial position at 32.8^oN. Notice the zero frequency of colored air parcels positions northward of 60^oN, this implies that "surf zone" air is not mixed with air inside the high vorticity gradient zone.

Figure 5.7b shows the positions of tracers but now taking into account the zonal coverage relative to the initial position, in this way they can be directly compared with the predictions for the respective density functions $\rho_\ell(\phi)$ given by maximum entropy theory (dotted lines). Recall that the density function $\rho_\ell(\phi)$ give us the probability of finding the absolute vorticity value $\hat{\zeta}_\ell$ within a small neighborhood as a function of latitude. There is a good fit between the red parcel positions and the corresponding density function in the magnitude, width and location of the tracers, as well as in its

zero value north of 60°N. The comparison between green tracer positions and its density function is good in the position of maximum frequency, but not in the magnitude and width of the curves.

Figure 5.8 is the time series of the total kinetic energy change (dashed line) and total absolute enstrophy change (continuous line) relative to their initial values for the direct numerical integration. The kinetic energy curve shows a steady dissipation, reducing its initial value by approximately 0.75% at the end of the integration. The absolute enstrophy curve shows a sharp reduction of around 1.25% between day 5 and day 30, this is the period of maximum nonlinear behaviour of the flow with Rossby wave breaking, ejection of vorticity filaments and strong mixing. From day 30 to 100, the absolute enstrophy curve shows a further reduction of aroun 0.25% but with signs of approaching an asymptotic value which is consistent with the numerical simulation of McWilliams (1984), and with the main hypothesis of minimum enstrophy theory described in chapter 4.

A comparison of the zonal wind profiles for this experiment (Fig. 5.9) shows that the initial condition is modified by the direct numerical integration just southward of 55°N; the velocity maximum is reduced by around 5 ms^{-1} while the jet broadens towards the south, creating a weak easterly flow between $10^o - 25^o$N and between the South Pole and 50°S. The maximum entropy prediction (red dashed line) has an easterly flow from the South Pole to 15°N, with a broadening of the jet and a slight modification of the initial condition at high northern latitudes, with a decrease of the initial wind maximum of the order of 10 ms^{-1}. For the minimum enstrophy predictions with one edge we see an acceleration of the jet at high northern latitudes which is not consistent with the direct numerical integration profile. The minimum enstrophy prediction with constant energy and two edges broadens the velocity profile, predicting mixing from 17.7°N to 64.8°N, reducing the wind maximum more than the other predictions. For the minimum enstrophy prediction with constant angular momentum and two edges no solution was found.

A comparison of the absolute vorticity profile is made in Fig. 5.10. With the exception of the minimum enstrophy prediction with constant angular momentum and one edge, all the other predictions remove the reversal of the absolute vorticity gradient. The minimum enstrophy predictions with one edge violate the conservation of vorticity, predicting a maximum of ζ higher than the max-

imum in the initial condition. This is a failure in the assumption that vorticity will be mixed all the way to the North Pole; instead, the minimum enstrophy prediction with constant energy and two edges has a better fit in comparison with the direct numerical integration.

The best prediction for this experiment is that given by the maximum entropy theory. The vorticity profile between the maximum entropy prediction and the time integration is good in the Southern Hemisphere, while in the Northern Hemisphere maximum entropy has a relative good agreement with the time integration. Note that, while the maximum entropy results are global, the minimum enstrophy results are restricted to a portion of the sphere.

The actual absolute enstrophy values for the minimum enstrophy predictions are as follows: 98.34% of initial value for minEF-$\mathcal{E}$ with two edges; 98.00% for minEF-$\mathcal{E}$ with one edge; and 99.16% for minEF-$\mathcal{M}$ with one edge. These values can be compared with the value of 98.45% at $t = 100$ days of the numerical integration.

5.2.2 Experiment 2

Experiment 2 consists of a tanh type jet (equation 5.1) with the following parameter values: $U = 180\text{ms}^{-1}$, $\phi_0 = 45^o\text{N}$, $B = 4^o$, corresponding to the experiment of Fig. 6a of Ishioka and Yoden (1994). The initial absolute vorticity profile, in both its continuous and discrete version of 60 vorticity levels (Fig. 5.11), has a local absolute vorticity maximum at $\phi = 35^o\text{N}$, and a local minimum at $\phi = 44.5^o\text{N}$; this minimum is contiguous to a steep vorticity gradient and, northward, a flat vorticity region from 50^oN to the North Pole. Since this profile has a region in the Northern Hemisphere where $\zeta < 0$, it is inertially unstable and therefore is not a valid initial condition. However, since Ishioka and Yoden (1994) showed the nonlinear behaviour of this polar vortex in their Fig. A1, it will be interesting to compare their results with our nonlinear run.

Figure 5.12 shows the normalized real and imaginary parts of the most unstable mode as a function of wavenumber m for the linear stability analysis. Wavenumbers 4 through 7 have the fastest exponential growth with e-folding times on the order of 0.4 days (Table 5.1) and periods between 1.89 and 0.89 days.

The direct numerical integration with triangular truncation T150 ($M = 150$), $\nu = 2.23 \times 10^{14}\mathrm{m}^4\mathrm{s}^{-1}$ and a timestep of 300s, after 3.0 days of simulation (Fig. 5.13b), shows folding of vorticity contours near the local minimum of absolute vorticity (the shading corresponds to regions where $\zeta < 0$), where a ring of 500 (green) air parcels is located. The ring of 500 red parcels is at the local maximum of ζ, that is, at $\phi = 35^o$N. At $t = 5.0$ days the surf zone at midlatitudes has evolved into four well-differentiated vortices with low absolute vorticity which contain most of the green air parcels, while red air parcels are advected towards the edge of maximum vorticity gradient. At later times (10 to 15 days) there is interaction of negative absolute vorticity regions while they migrate towards the Southern Hemisphere.

By the end of the numerical simulation ($t = 100$ days) the polar vortex has recovered its zonal symmetry, surrounded by a region of homogeneously distributed red air parcels at midlatitudes, and a homogeneous distribution of green parcels at low latitudes, which is a result of strong mixing of low and midlatitude air, but not of air inside the vortex edge, as discussed in experiment 1.

When comparing Fig. 5.13 and Ishioka and Yoden's Fig. A1, a similar evolution is seen but its occurrence is faster in our simulation. We attribute this to the different kind of diffusion we are using in our model which is a $\nu\nabla^4\zeta$-type, in constrast with Ishioka and Yoden's $\nu\nabla^2\zeta$-type. In our experiment there is less damping of low wavenumbers than in Ishioka and Yoden's experiment.

The reversal in positions of the tracers is clear in the histograms of Fig. 5.14, where now the red parcels are mostly north of the green parcels, in constrast with their positions at $t = 0$. The maximum entropy density function $\rho_\ell(\phi)$ for red parcels is in good agreement with the parcel positions, while for the green parcels the density functions is displaced south of the histogram by about 15^o. As in experiment 1, the isolation of the polar vortex core is relevant in the histogram plots.

For the time integration, a steady decrease of kinetic energy is observed as a function of time (Fig. 5.15), with a total decrease of less than 1% at $t = 100$ days. As in experiment 1, absolute enstrophy has a big decrease while most of the nonlinear activity is occurring (5 to 40 days); afterwards, it has a slow decrease towards an asymptotic value of around 95% of the initial absolute enstrophy.

A comparison between the zonal velocity predictions and the average zonal flow of the direct numerical integration (Fig. 5.16) shows a good agreement with the maximum entropy theory, but with a slight displacement in the Northern Hemisphere of the maximum entropy curve of about 5^o to the south and a lower peak. Maximum entropy theory is able to predict the appearence of easterlies in the Southern Hemisphere. The minEF-$\mathcal{E}$ with two edges gives us a good agreement for the mixing region $\phi_s = 16.89^o$N to $\phi_n = 64.31^o$N. The minimum enstrophy predictions with one edge accelerate the jet at high latitudes, while that behaviour is not observed in the time integration.

The absolute vorticity predictions for minEF-$\mathcal{E}$ with two edges and maximum entropy (Fig. 5.17) are in good agreement with the time integration, they both remove the local minimum of ζ homogenizing the absolute vorticity in the Northern Hemisphere midlatitudes. Maximum entropy predicts quite well the absolute vorticity profile in the Southern Hemisphere. A violation in the conservation of the absolute vorticity maximum is observed in the minimum enstrophy predictions with one edge, which prevents us from using the hypothesis of vorticity change all the way to the North Pole in problems where the poleward region is not mixing.

After 100 days of direct numerical integration, 95.32% of the initial absolute enstrophy is left, which can be compared with the values of 97.73% for minEF-$\mathcal{M}$, 95.76% for minEF-$\mathcal{E}$ with one edge, and 96.12% for minEF-$\mathcal{E}$ with two edges.

5.2.3 Experiment 3

This experiment consists of a sech-type jet (equation 5.2) with $U = 240\text{ms}^{-1}$, $\phi_0 = 60^o$N and $B = 20^o$. These values correspond to the Ishioka and Yoden (1994) experiment of their Fig. 10e. The basic absolute vorticity is

$$\zeta_0(\phi) = \frac{2}{aB} u_0(\phi)\ \tanh\left[\frac{2(\phi - \phi_0)}{B}\right] + \frac{2u_0(\phi)}{a}\ \tan\phi + 2\Omega\ \sin\phi. \tag{5.6}$$

The initial absolute vorticity profile (Fig. 5.18) has a maximum at $\phi = 66^o$N and a relative minimum at the North Pole.

Linear stability analysis results (Table 5.1) show instability in zonal wavenumbers 1, 2 and 3

with e-folding times of 4.44, 5.15 and 7.22 days respectively, and periods of 2.18, 1.21 and 0.82 days. Wavenumber 1 is the fastest linear growth mode.

The nonlinear evolution for experiment 3 is shown in Fig. 5.19; it has been used a triangular truncation of 150 ($M = 150$), $\nu = 3.35 \times 10^{14}\mathrm{m}^4\mathrm{s}^{-1}$ and timestep of 300s. At t=0, 500 red air parcels are located in a ring placed at the maximum of absolute vorticity ($\phi = 66^o$N), and the ring of 500 green air parcels is at $\phi = 75^o$N. Nonlinear behaviour begins to appear at later times than in the previous two experiments, this is consistent with the larger e-folding time (from 4 to 7 days) of the linear stability analysis. After 30.0 days of evolution, the polar vortex shows two foldings of the red parcel ring, while the green ring presents an elliptical shape. At $t = 40.0$ days most of the red parcels are embedded in a coherent vortex which tends to move towards and around the North Pole, while the relative lower absolute vorticity originally at the North Pole is being displaced southward conserving its integrity.

At $t = 50.0$ days and $t = 60.0$ days most of the red air parcels are placed close to the North Pole, and the green ring is being elongated and disrupted. The rest of the time integration uniform mixing of green air parcels at latitudes between 45^oN and 75^oN is observed (Fig. 5.20), and the red air parcels have a preference to stay close to the North Pole. It is evident that in this experiment all the activity is confined to latitudes north of 40^oN.

Comparing the green air parcels positions at $t = 100$ days with its respective density function given by the maximum entropy result, we can see that the green density function has a comparable magnitude between 50^oN and 70^oN, but has a higher value northward; red air parcels positions at $t = 100$ days and its respective density function have a better agreement, showing a steady increase going from 50^oN to the North Pole. In contrast with the previous two experiments, the polar vortex core has suffered a substantial change during the nonlinear evolution, while southern latitudes experience no significant modification of the initial condition.

An approximately steady decay of the total kinetic energy is observed (Fig. 5.21) for the direct numerical integration, but the absolute enstrophy has a steep decay between 40 to 80 days, where most of the nonlinear behaviour and strong mixing is occurring.

Figure 5.22 compares the zonal wind profiles for the time integration at 100 days (black dashed line) with those given by the minEF-$\mathcal{E}$ (blue line) and minEF-$\mathcal{M}$ (violet line) both with one edge and by the maximum entropy (red dashed line) predictions. A good agreement in the zonal wind is seen for all of the predictions; the minEF-$\mathcal{M}$ overlays with the time integration curve on most of the plot, except at the region of maximum wind.

A comparison for the absolute vorticity field (Fig. 5.23) shows that the time integration and all the predictions remove the relative minimum that initially was at the North Pole, giving an equilibrium state where the absolute vorticity is monotonically increasing with latitude. The best prediction for $\zeta(\phi)$ is minEF-$\mathcal{M}$ which overlays the time integration plot. The maximum entropy result overpredicts mixing of vorticity at latitudes higher than about 50^oN, while the minEF-$\mathcal{E}$ prediction gives a far south mixing edge at $\phi = 20^o$N.

The absolute enstrophy values of the equilibrium states, given as a percentage of the initial field, are 98.28% at $t = 100$ days of the direct numerical integration, 98.02% for minEF-$\mathcal{E}$, and 98.33% for minEF-$\mathcal{M}$.

5.2.4 Experiment 4

Experiment 4 is a sech-type jet (equation 5.2) with $U = 180\text{ms}^{-1}$, $\phi_0 = 60^o$N and $B = 10^o$, which is the experiment of Fig. 11a of Ishioka and Yoden (1994). This initial condition has three reversals of the absolute vorticity gradient (see Fig. 5.24); the maximum of $\zeta(\phi)$ is at $\phi = 63.5^o$N, with a relative maximum at $\phi = 41.8^o$N and two relative minima at 54^oN and at the North Pole.

As in Ishioka and Yoden (1994) and Hartmann (1983) we show the results of the linear stability analysis for the "polar" mode and for the "midlatitude" mode (Table 5.1). Polar modes show instability for wavenumbers 1 to 4, while midlatitude modes are unstable for wavenumbers 2 to 7. The most unstable (midlatitude) mode is wavenumber 4 with e-folding time of 1.11 days and period of 1.65 days.

The run of the nonlinear barotropic model using a triangular truncation of $M = 150$, $\nu = 2.23 \times 10^{14}\text{m}^4\text{s}^{-1}$ and timestep of 300s, is shown in Fig. 5.25. We have included the trajectory

calculation for 1000 colored air parcels, initially distributed in 4 rings with 250 color parcels each; the green ring is placed at the relative maximum of $\zeta(\phi)$ at $\phi = 41.8^{o}$N; the blue ring is at the relative minimum of $\zeta(\phi)$ at $\phi = 54^{o}$N; 250 red air parcels are at the maximum of absolute vorticity ($\phi = 63.5^{o}$N) and a ring closer to the pole ($\phi = 75^{o}$N) consists of 250 yellow air parcels.

After 6.0 days of time integration is clear a folding of absolute vorticity contours at latitudes close to the blue air parcel ring. At $t = 8.0$ days a zonal wavenumber 4 instability is seen at midlatitudes, equatorward of the highest absolute vorticity gradient, and another wavenumber 4 instability occurs poleward of the highest absolute vorticity gradient. At $t = 10.0$ days a strong mixing of vorticity is observed at middle and high latitudes; green air parcels have been advected towards the polar vortex edge and blue air parcels towards lower latitudes; the yellow and red rings preserve most of their integrity while they move around the pole and begin to switch places. Long, thin filaments are observed both inside and outside the region of highest absolute vorticity gradient.

Strong mixing is present at $t = 15.0$ days with detachment and diffusion of vorticity filaments, as well as dispersion of colored air parcels northward of 20^{o}N. At the end of the time integration (100 days), the polar vortex has zonal symmetry and colored air parcels are distributed over the whole Northern Hemisphere. Fig. 5.26 shows that green air parcels are preferentially placed northward of blue air parcels, while red air parcels mostly stay poleward than yellow air parcels, contrary to their initial positions. The density functions of maximum entropy theory have a remarkable agreement with the green, yellow and red air parcels positions, but the blue air parcels have a wider distribution than that predicted by maximum entropy.

At $t = 100$ days the kinetic energy has a total decrease of 98.5% of its initial value (Fig. 5.27), most of it occurring after $t = 10.0$ days. The absolute enstrophy curve for the time integration has a steep decay between 10 and 25 days, followed by a slight decrease at later times, finishing at $t = 100$ days at 96.4% of its initial value.

The comparison of the zonal wind profiles for the three predictions and the direct numerical integration (Fig. 5.28) shows a good agreement for the value of the wind maximum ($\sim 65\text{ms}^{-1}$) which has decreased from an original wind maximum of the order of 90ms^{-1}. Minimum enstro-

phy predictions reproduce well the zonal wind distribution at high northward latitudes, while the maximum entropy prediction wind field is shifted southward by about 10^o.

The predictions of the zonal absolute vorticity profile are shown in Fig. 5.29. The best agreement is for minEF-$\mathcal{E}$ which predicts a south mixing edge of 31.9^oN and closely follows the time integration result. The absolute vorticity given by maximum entropy theory has a lower maximum that in the initial condition, which can be interpreted as the macroscopic view of strong mixing of vorticity levels for high northward latitudes. The minEF-$\mathcal{M}$ absolute vorticity curve has a good agreement with the time integration between 55^oN and 75^oN. The actual absolute enstrophy values at $t = 100$ days for the direct numerical integration is 96.38% of the initial value, 96.37% for minEF-$\mathcal{E}$ and 96.43% for minEF-$\mathcal{M}$.

5.3 Discussion

Barotropic instability of the polar night jet has been investigated using a linear model, as well as nonlinear time integration of a nondivergent barotropic model on the sphere. The mechanism by which the flow instabilities are removed is the breaking and mixing of vorticity in regions where the absolute vorticity gradient has a sign reversal. Most of the nonlinear phase is marked by "wave breaking", filamentation of vorticity contours, dispersion of air parcel tracers, and a rapid decrease of the total enstrophy of the flow. Results obtained with both linear and nonlinear analysis are consistent with the work of Ishioka and Yoden (1994).

The nonlinear activity is followed by a quasi-steady state of the fluid, which in our experiments is characterized by an almost zonally symmetric flow that has a small and steady decay of kinetic energy while seems to approach an asymptotic value of enstrophy. Theoretical predictions of this end-state, given by the maximum entropy theory of chapter 3 and minimum enstrophy theory of chapter 4, are compared with the zonal average of absolute vorticity and zonal wind at $t = 100$ days of the direct numerical integration.

Predictions from the maximum entropy theory demonstrated good skill for flows which have a substantial change over the whole sphere. The minimum enstrophy predictions showed a very good

agreement with flows which nonlinear behaviour is restricted to a polar cap.

The above predictions are compared with the zonal average of the direct numerical integration. Therefore, any deviation from zonal symmetry of the flow will have a negative impact in the comparisons.

The predictions are based upon the initial flow condition, and since we are using a numerical model with a diffusive term, the energy of the flow will be reduced over time, thus changing the actual energy value of the equilibrium state. Flows with equilibrium states relatively far from the initial condition will overcome a significant decrease of energy before a steady state is reached; in those cases predictions which mantain a constant energy (like minEF-$\mathcal{E}$ and maximum entropy) will not have good skill when compared with the nonlinear time integration.

Maximum entropy theory gives us an additional source of information with the density functions $\rho_\ell(\phi)$, which in a probabilistic sense tells us how the vorticity field (and therefore the mass field) is redistributed at the equilibrium state. The density functions showed good skill predicting several of the colored air parcel spatial distributions in the above experiments. Also, from a local point of view, density functions give us a way to determine the degree of mixing of initially well separated air mases, information that could be valuable in the tracing of atmospheric chemical components.

Table 5.1: e-folding time τ_i and period τ_r as a function of zonal wavenumber m for all unstable modes obtained in the linear stability analysis for the polar vortex experiments, values in parenthesis of experiment 4 are for midlatitude modes.

e-folding time τ_i (days)

m	1	2	3	4	5	6	7	8	9	10
Exp. 1		1.78	0.811	0.774	0.972	2.25				
Exp. 2		1.19	0.559	0.454	0.421	0.420	0.443	0.498	0.615	1.72
Exp. 3	4.44	5.148	7.219							
Exp. 4	4.60	2.64	3.72	4.43						
		(6.50)	(1.20)	(1.11)	(1.17)	(3.03)	(12.19)			

Period τ_r (days)

m	1	2	3	4	5	6	7	8	9	10
Exp. 1		14.33	3.48	2.02	1.45	1.18				
Exp. 2		12.06	3.22	1.89	1.36	1.07	0.89	0.80	0.32	0.26
Exp. 3	2.18	1.21	0.82							
Exp. 4	2.91	1.63	1.09	0.813						
		(16.09)	(3.17)	(1.65)	(1.11)	(0.680)	(0.651)			

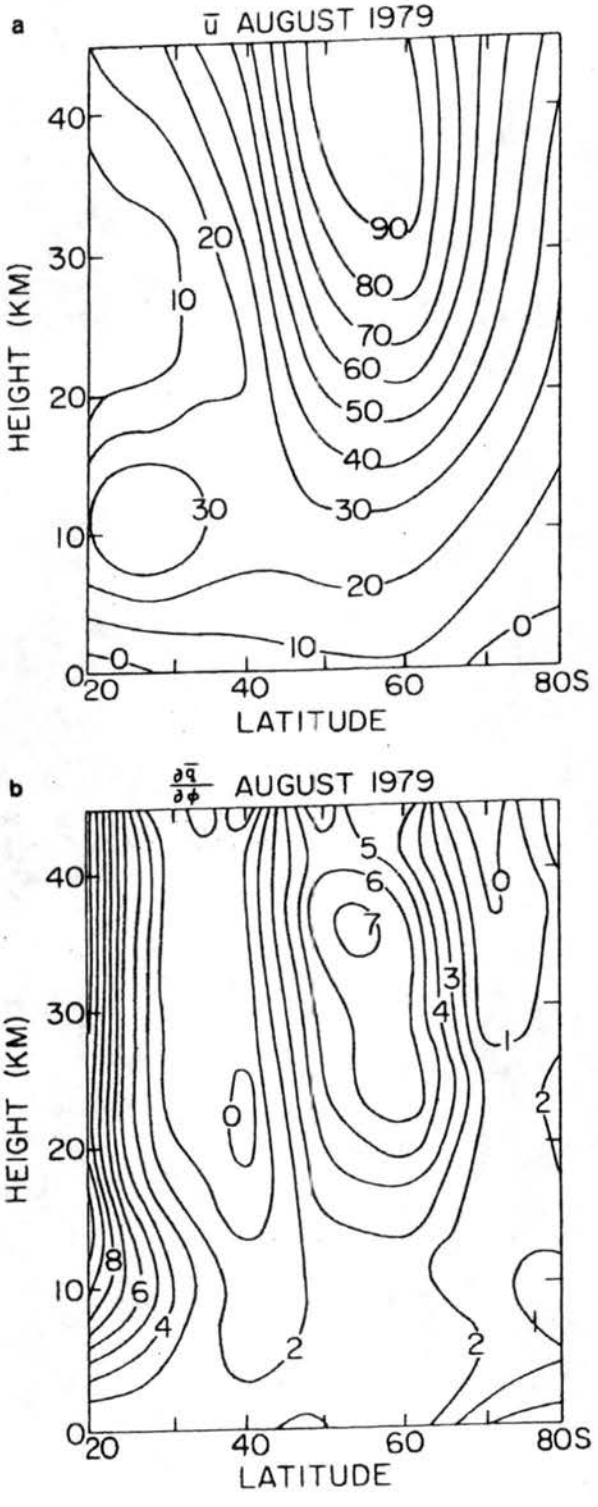

Figure 5.1: Height versus latitude contour plots of a) zonal-mean wind (ms^{-1}) and b) the smoothed gradient of potential vorticity (divided by Ω) for the month of August 1979 in the Southern hemisphere (from Hartmann, 1983).

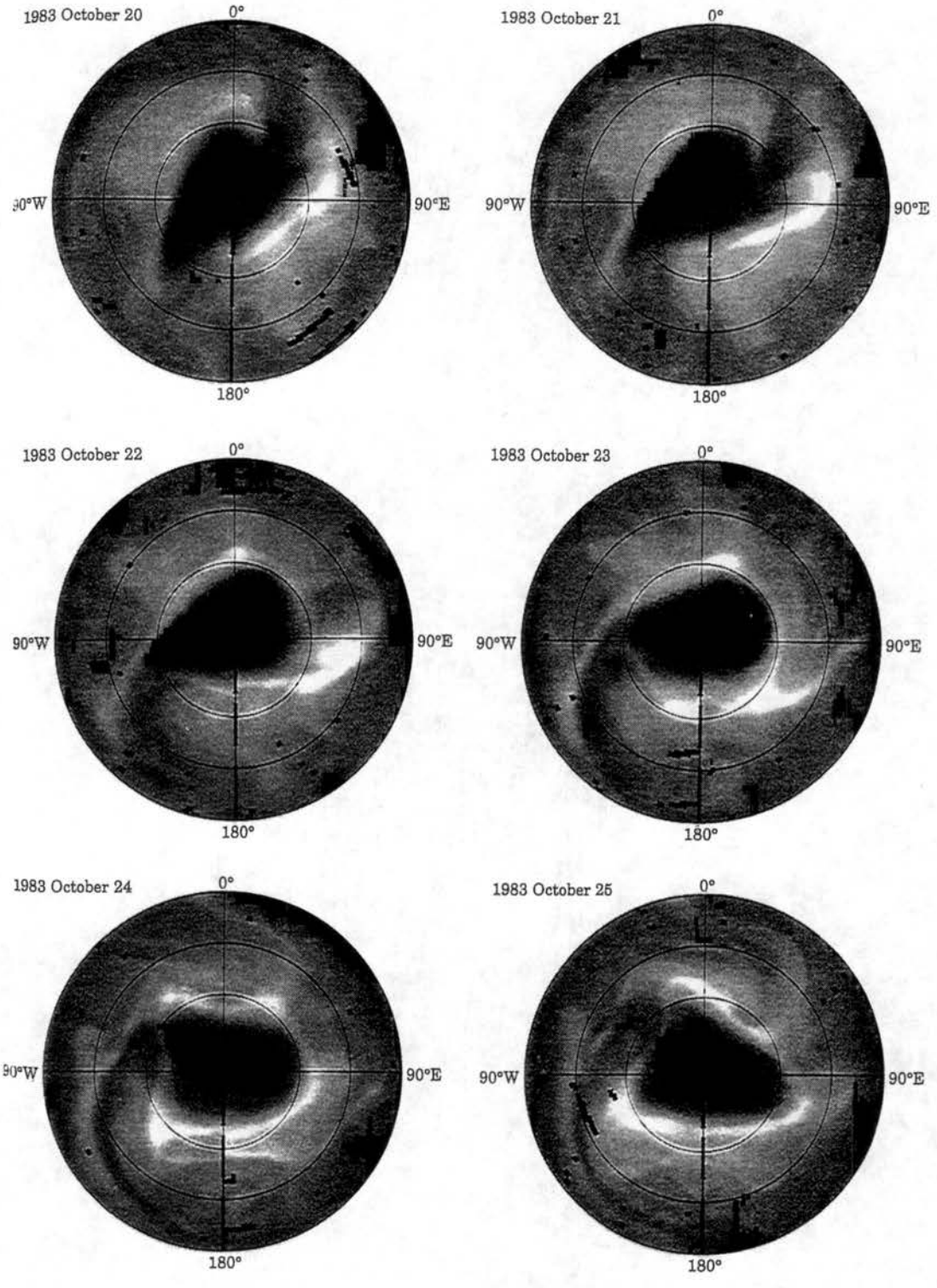

Figure 5.2: Daily TOMS images of total ozone in the Southern Hemisphere for six consecutive days in October 1983. Latitude circles are drawn at 40°, 60° and 80° S. The outermost latitude is 20°S. Taken from Bowman and Mangus (1993).

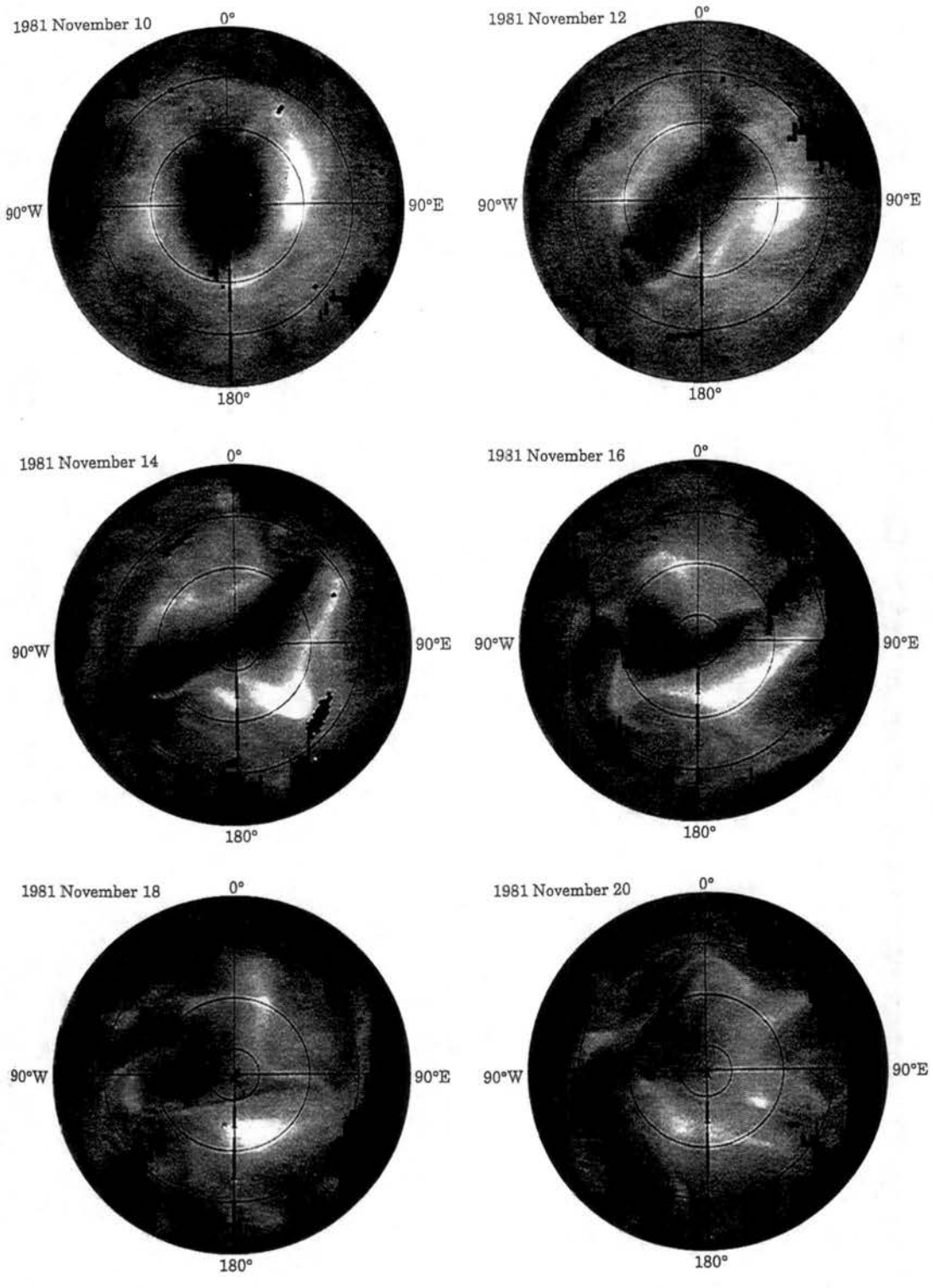

Figure 5.3: Daily TOMS images of total ozone in the Southern Hemisphere for six days in November 1981. Consecutive images are separated by two days. The map projection is as in Fig. 5.2. Taken from Bowman and Mangus (1993).

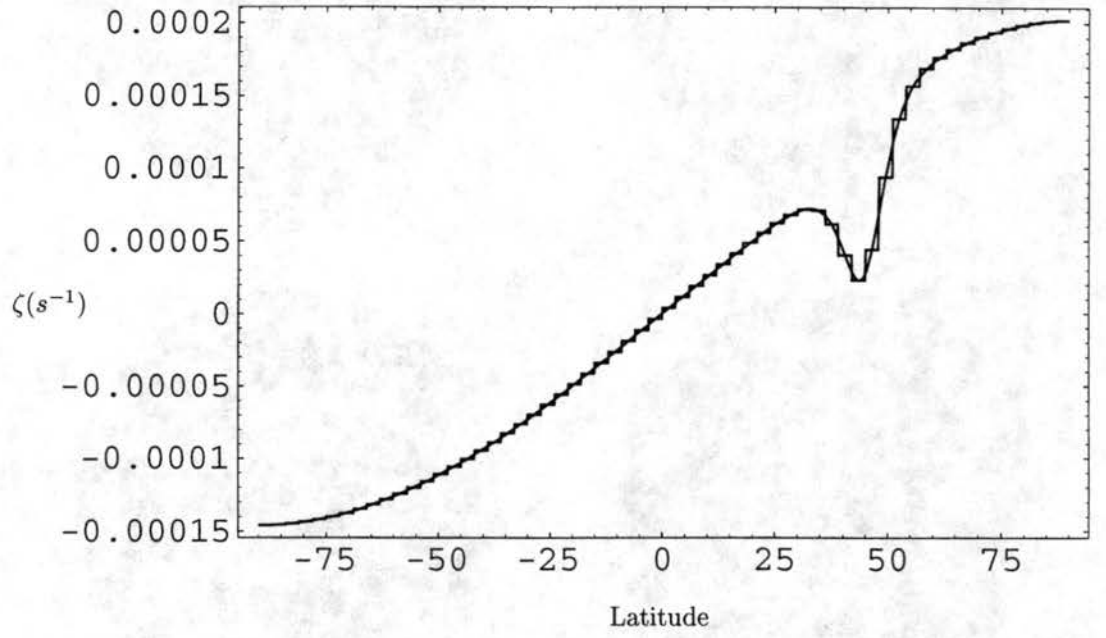

Figure 5.4: Initial absolute vorticity profiles for the direct numerical integration and for the maximum entropy theory (step-wise plot). Experiment 1.

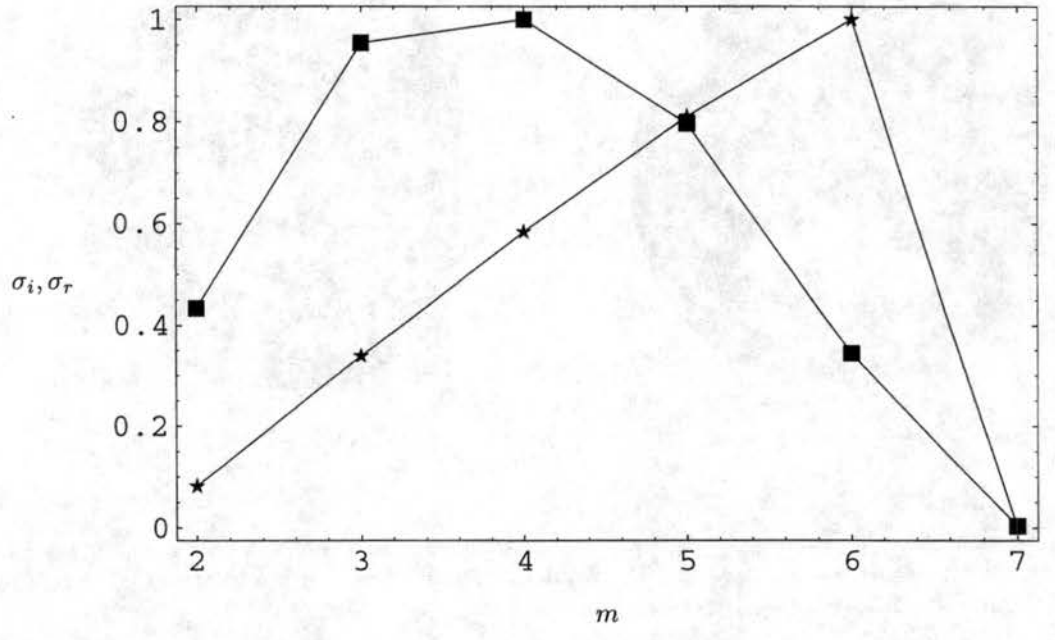

Figure 5.5: Linear stability analysis results for the normalized frequencies: Normalized σ_i (squares) and σ_r (stars) as a function of zonal wavenumber m. Experiment 1.

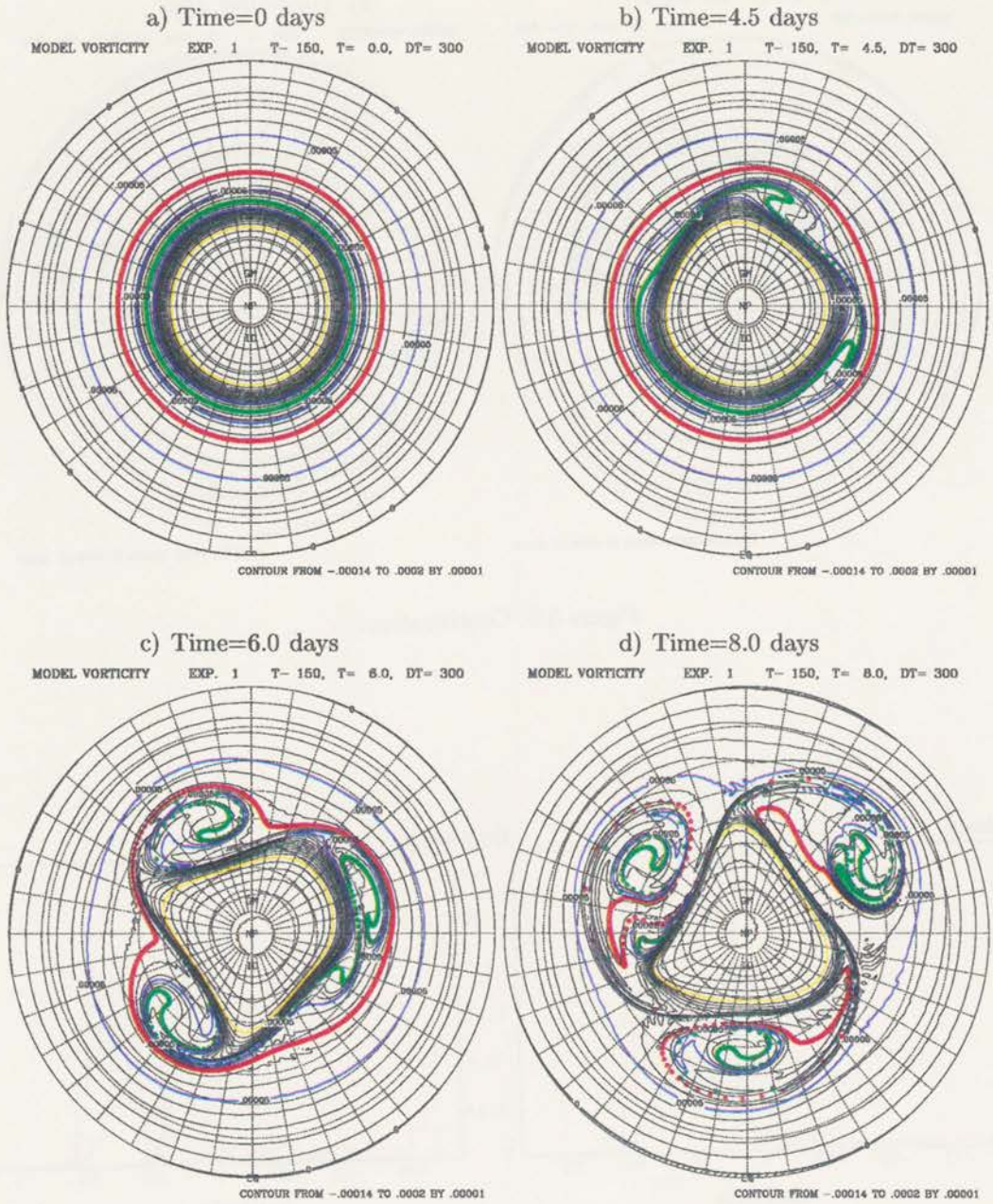

Figure 5.6: Northern Hemisphere polar stereographic plots of the absolute vorticity field (in s^{-1}) and tracer positions for selected snapshots of experiment number 1.

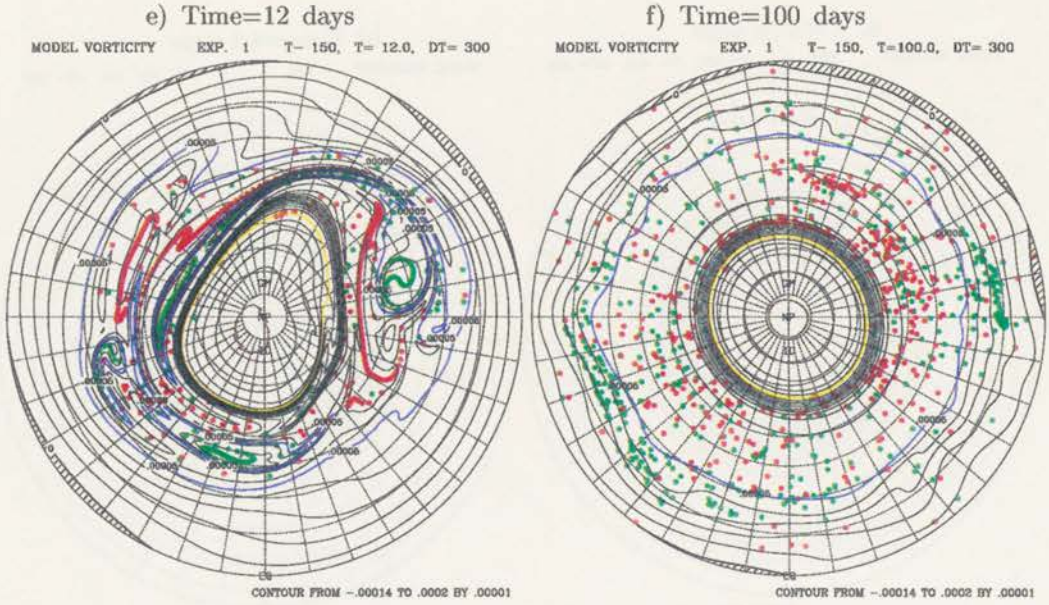

Figure 5.6: Continuation.

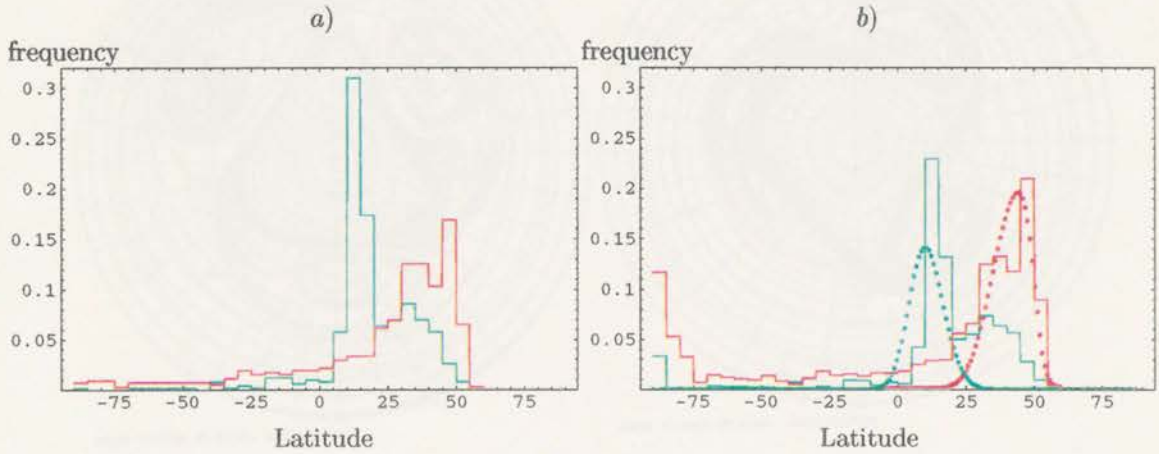

Figure 5.7: a) Tracer positions as a function of latitude for time = 100 days of direct numerical integration. Positions counted at 5 degrees latitude intervals. b) Same as a) but taking into account zonal coverage relative to initial position, displayed together with their respective density function. Experiment 1.

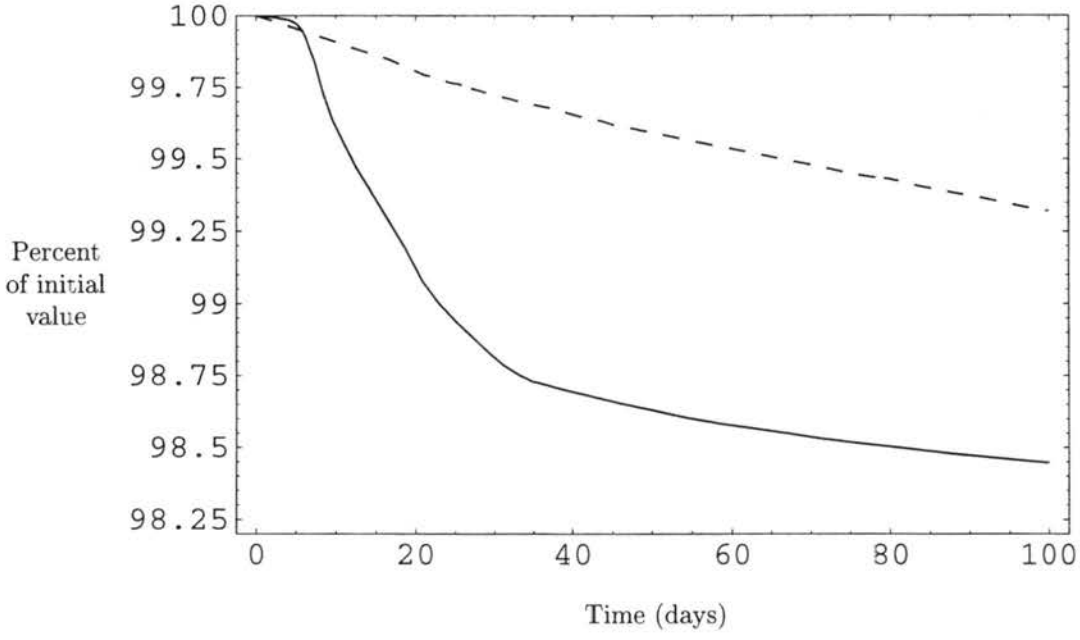

Figure 5.8: Time dependence of the kinetic energy (dashed line) and absolute enstrophy (continuous line) relative to their initial values for experiment 1.

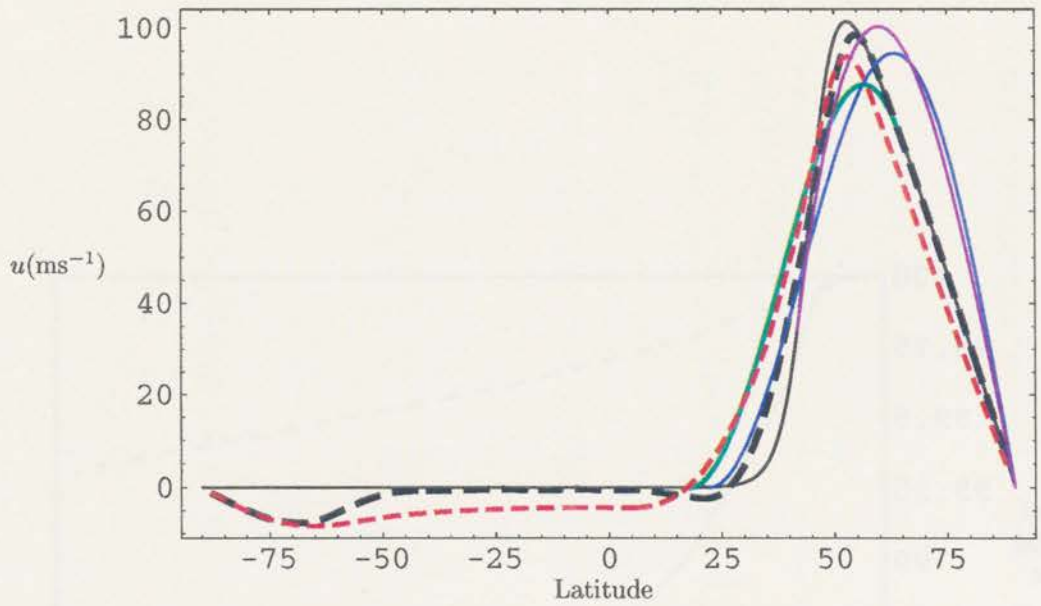

Figure 5.9: Zonal wind profiles. Initial condition: black solid line. Direct numerical integration at t=100 days: black dashed line. MinEF-$\mathcal{E}$ with two edges: green line. Maximum entropy prediction: red dashed line. MinEF-$\mathcal{E}$ with one edge: blue line. MinEF-$\mathcal{M}$ with one edge: violet line. Experiment 1.

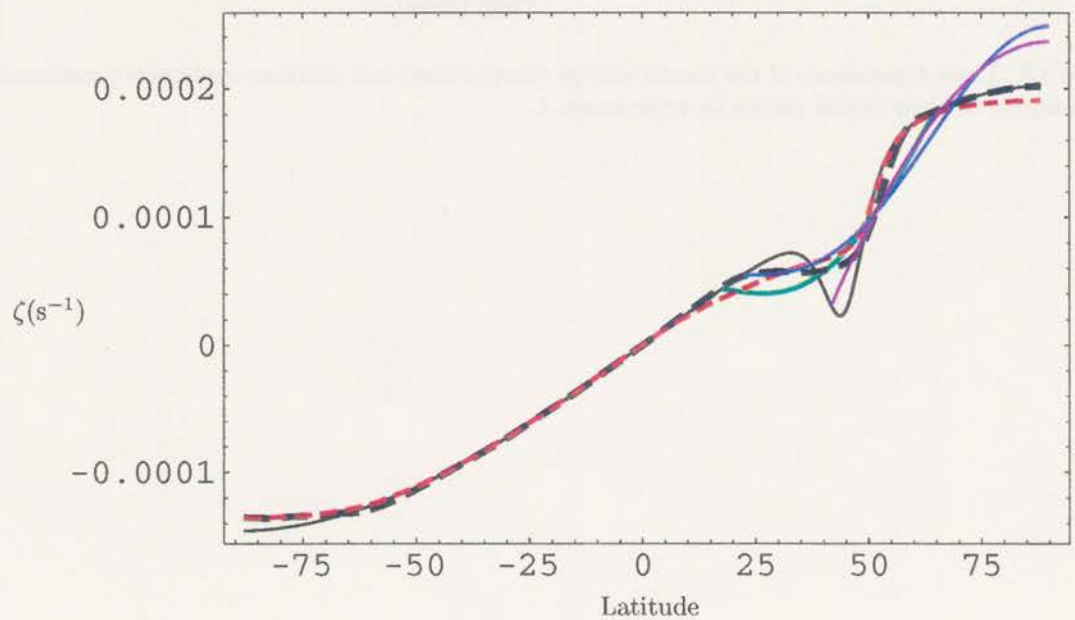

Figure 5.10: Same than Fig. 5.9 but for absolute vorticity profiles. Experiment 1.

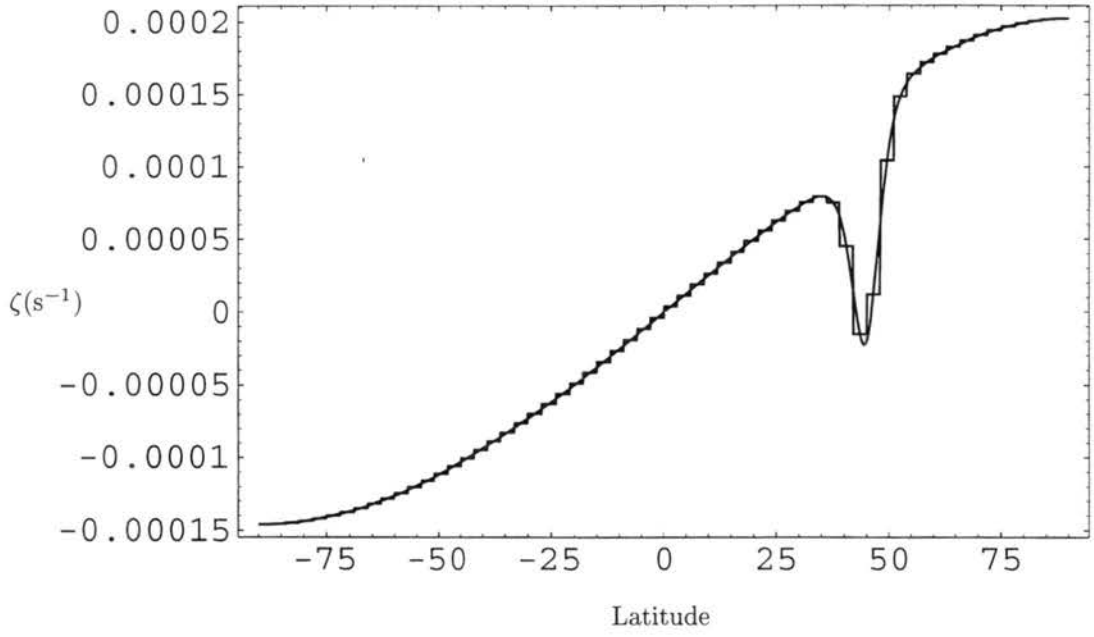

Figure 5.11: Initial absolute vorticity profiles for the direct numerical integration and for the maximum entropy theory (step-wise plot). Experiment 2.

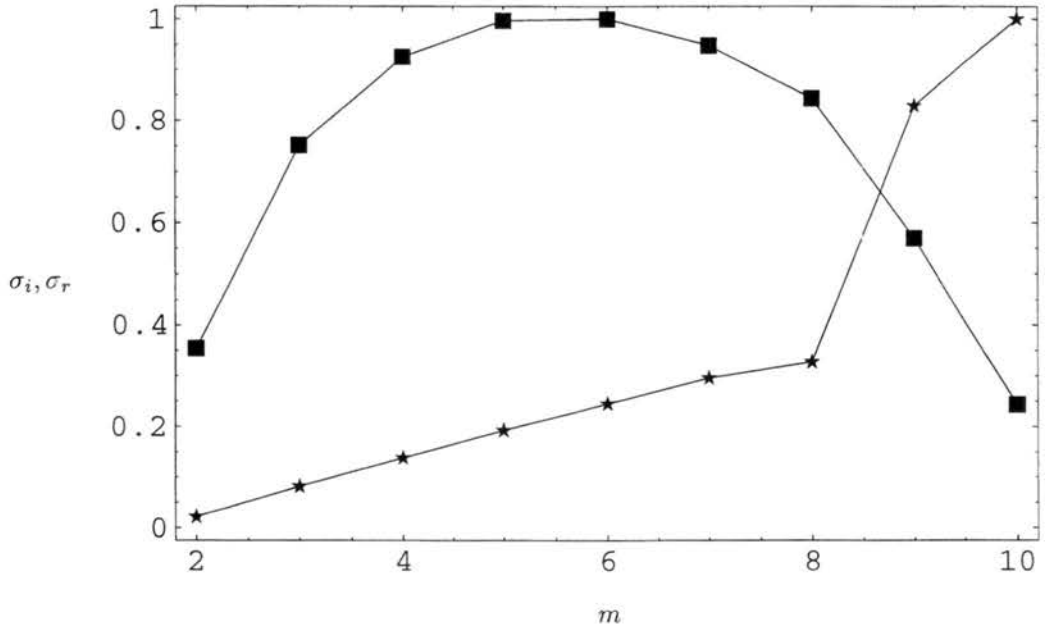

Figure 5.12: Linear stability analysis results for the normalized frequencies: Normalized σ_i (squares) and σ_r (stars) as a function of zonal wavenumber m. Experiment 2.

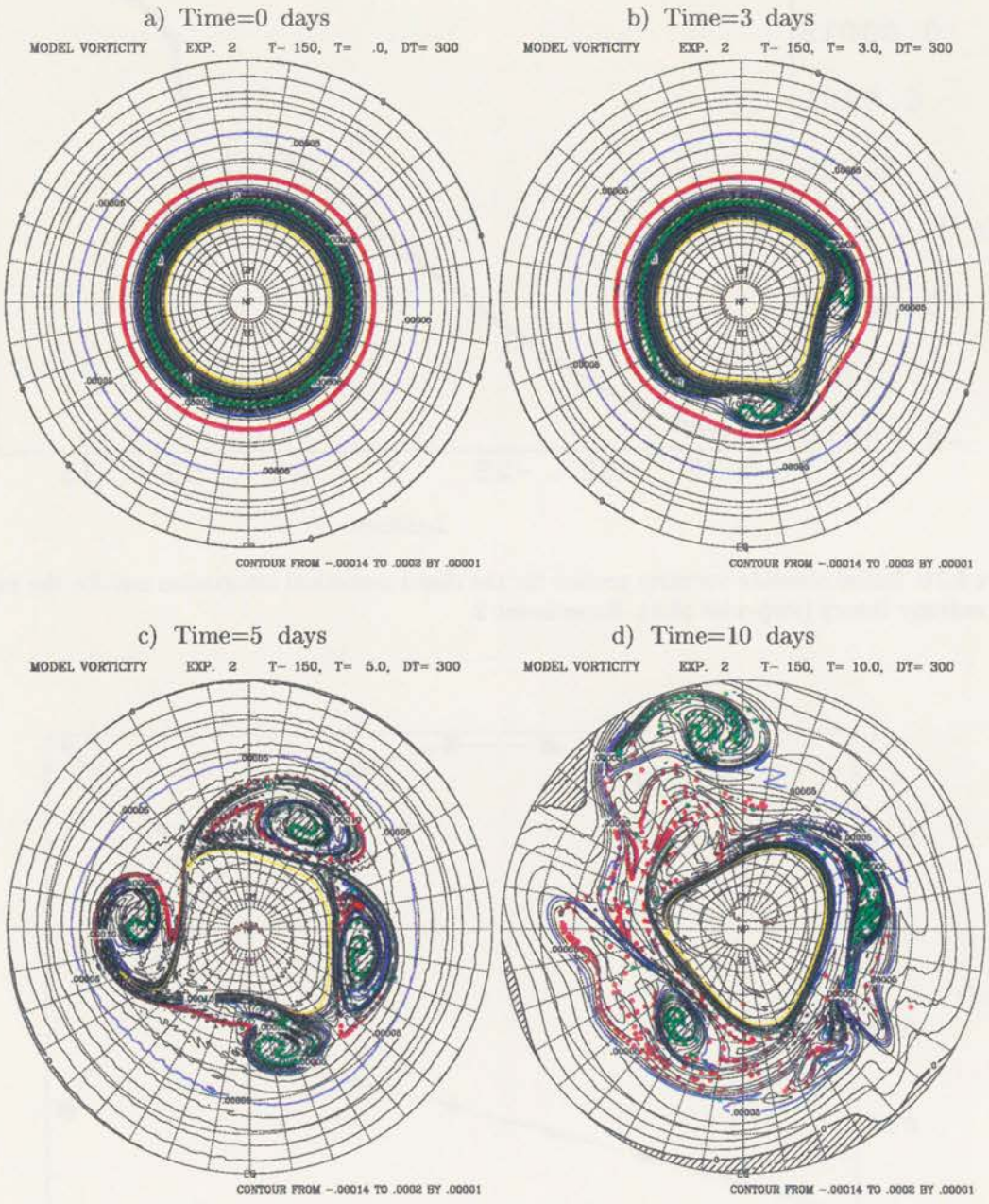

Figure 5.13: Northern Hemisphere polar stereographic plots of the absolute vorticity field (in s^{-1}) and tracer positions for selected snapshots of experiment number 2.

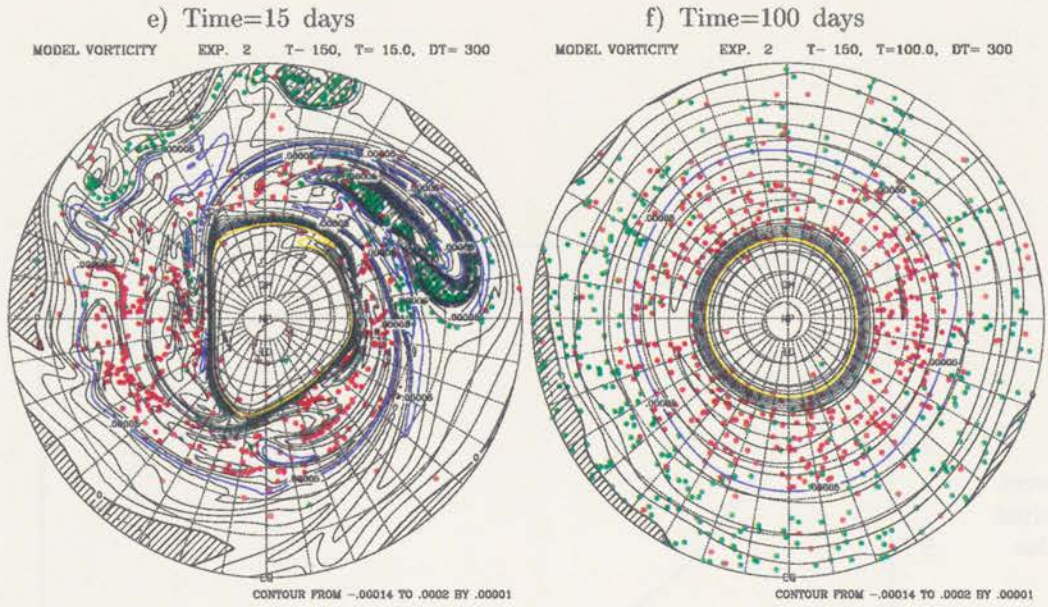

Figure 5.13: Continuation.

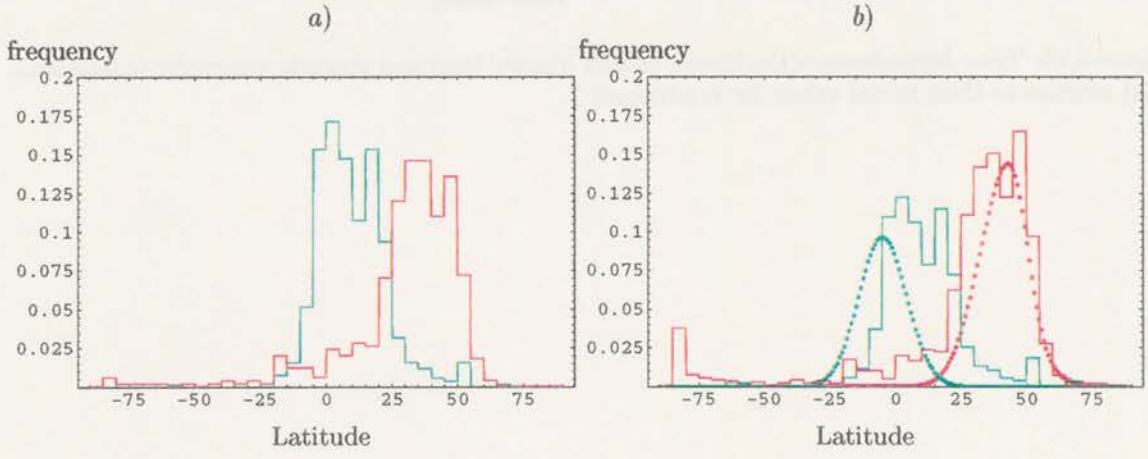

Figure 5.14: a) Tracer positions as a function of latitude for time = 100 days of direct numerical integration. Positions counted at 5 degrees latitude intervals. b) Same as a) but taking into account zonal coverage relative to initial position, displayed together with their respective density function. Experiment 2.

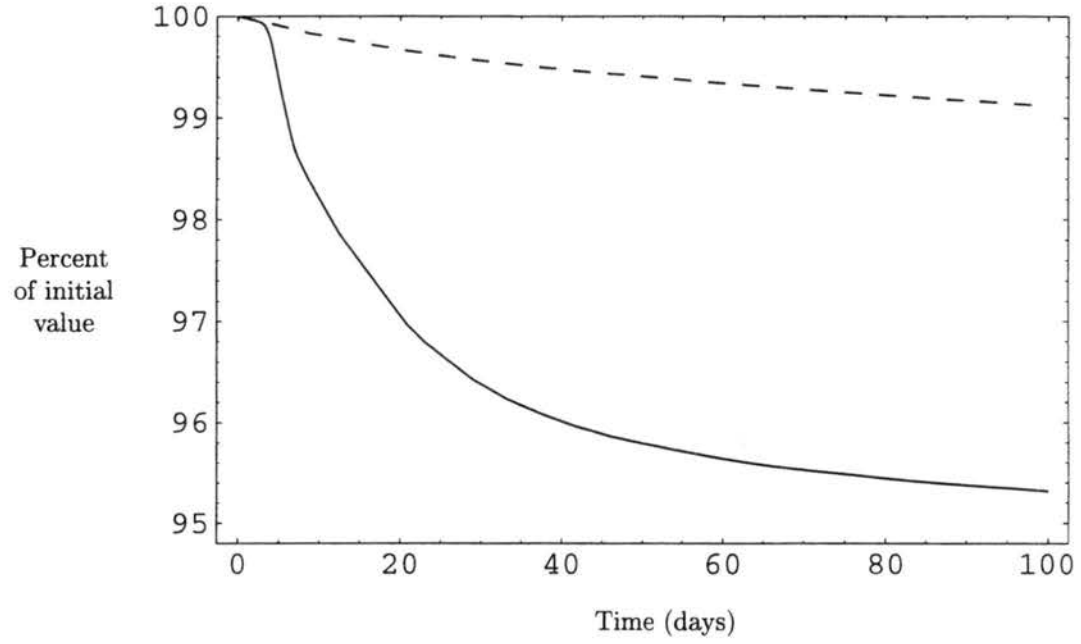

Figure 5.15: Time dependence of the kinetic energy (dashed line) and absolute enstrophy (continuous line) relative to their initial values for experiment 2.

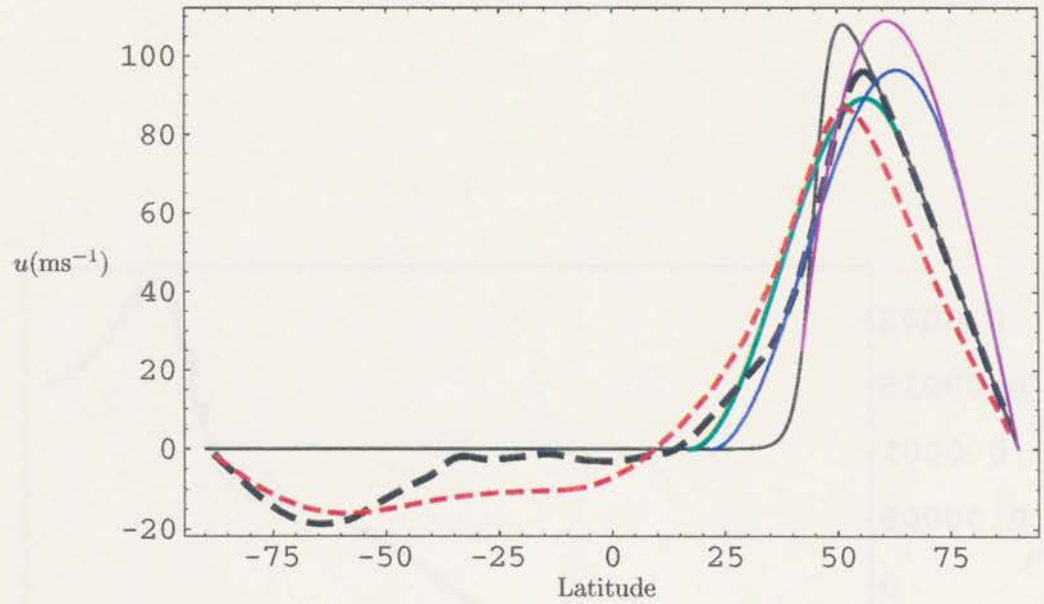

Figure 5.16: Zonal wind profiles. Initial condition: black solid line. Direct numerical integration at t=100 days: black dashed line. MinEF-$\mathcal{E}$ with two edges: green line. Maximum entropy prediction: red dashed line. MinEF-$\mathcal{E}$ with one edge: blue line. MinEF-$\mathcal{M}$ with one edge: violet line. Experiment 2.

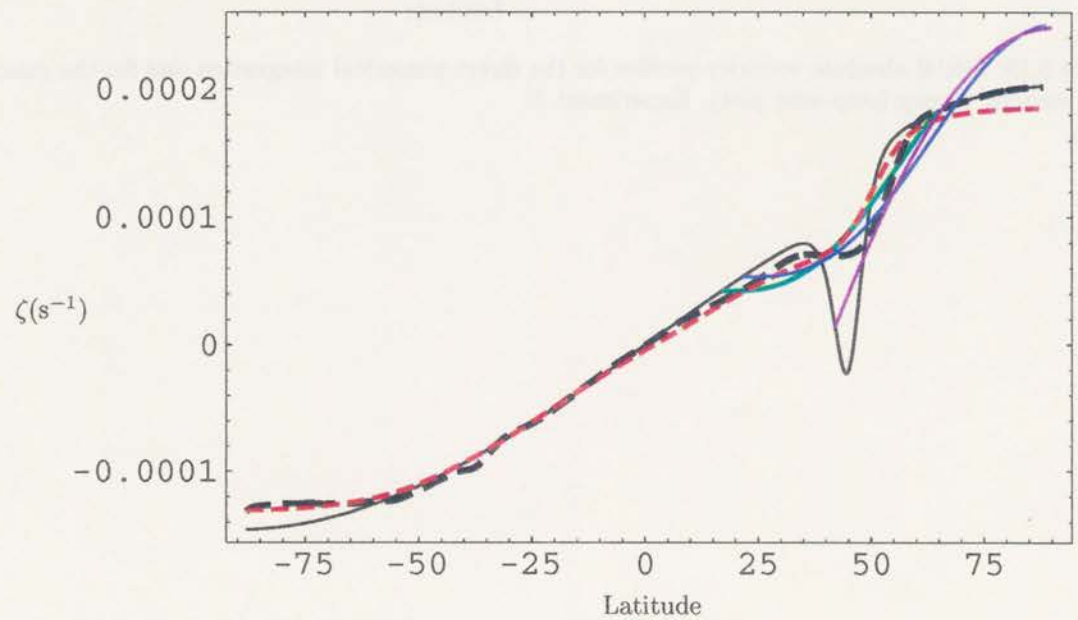

Figure 5.17: Same than Fig. 5.16 but for absolute vorticity profiles. Experiment 2.

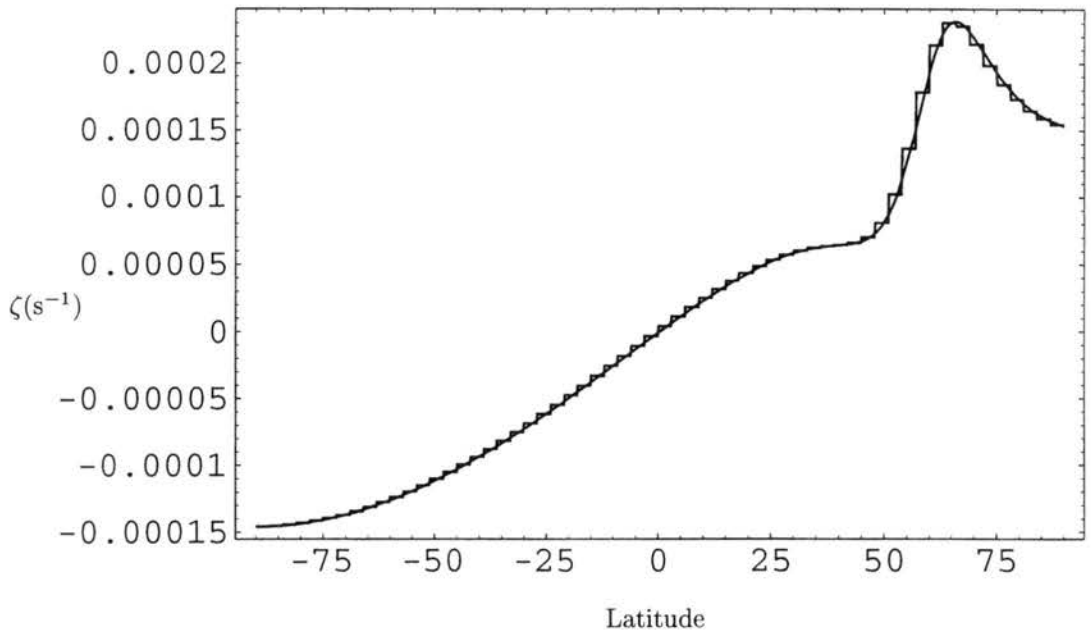

Figure 5.18: Initial absolute vorticity profiles for the direct numerical integration and for the maximum entropy theory (step-wise plot). Experiment 3.

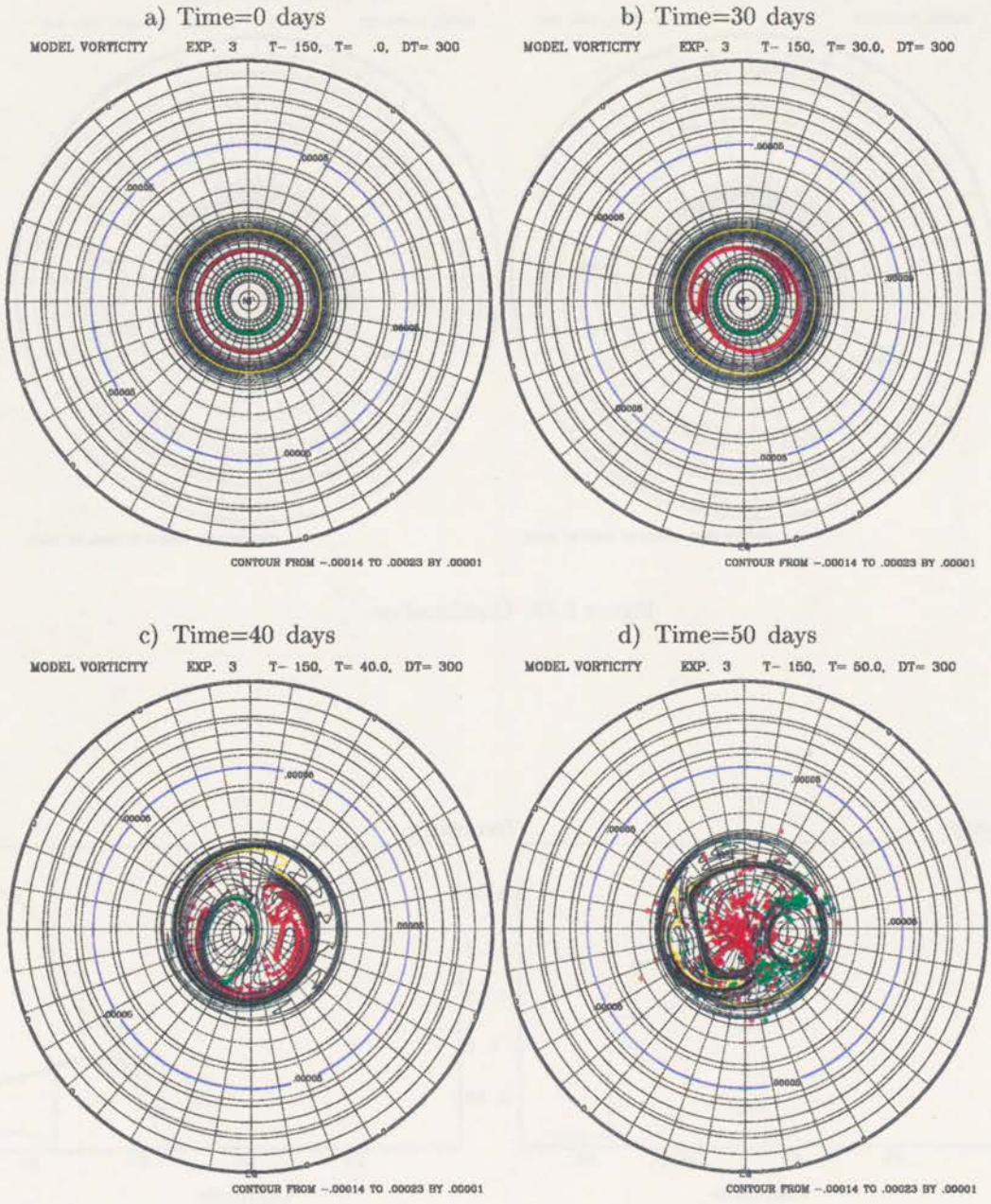

Figure 5.19: Northern Hemisphere polar stereographic plots of the absolute vorticity field (in s^{-1}) and tracer positions for selected snapshots of experiment number 3.

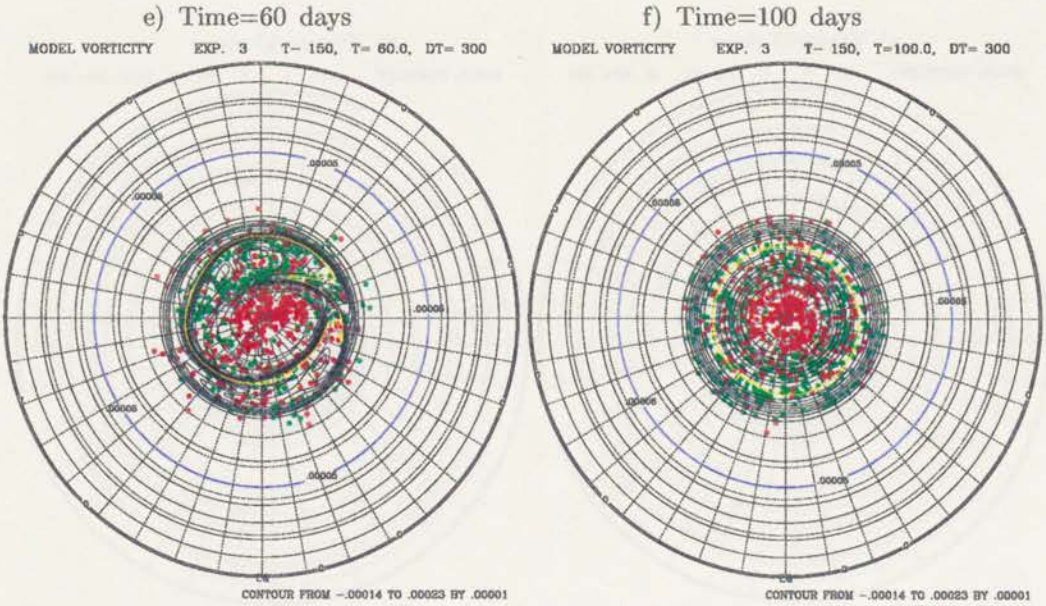

Figure 5.19: Continuation.

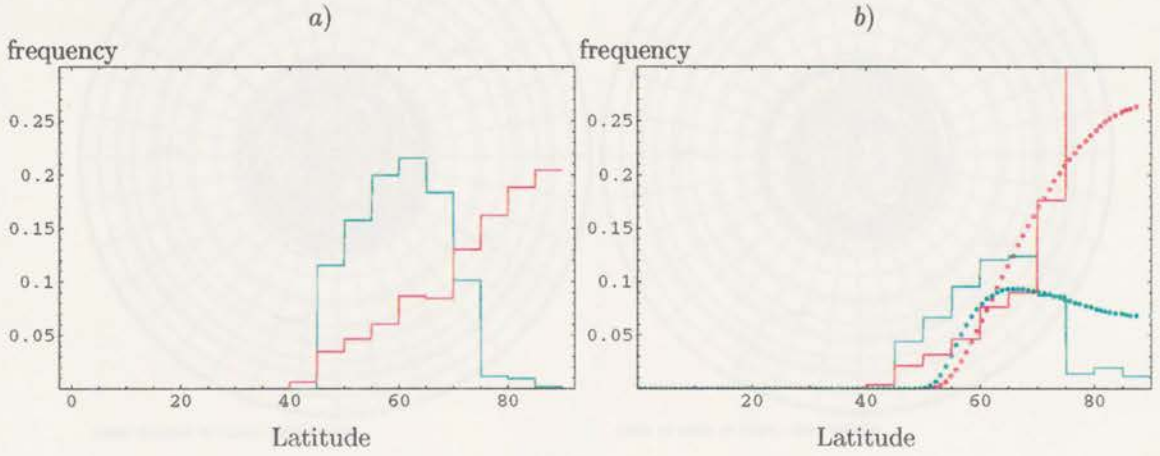

Figure 5.20: a) Tracer positions as a function of latitude for time = 100 days of direct numerical integration. Positions counted at 5 degrees latitude intervals. b) Same as a) but taking into account zonal coverage relative to initial position, displayed together with their respective density function. Experiment 3.

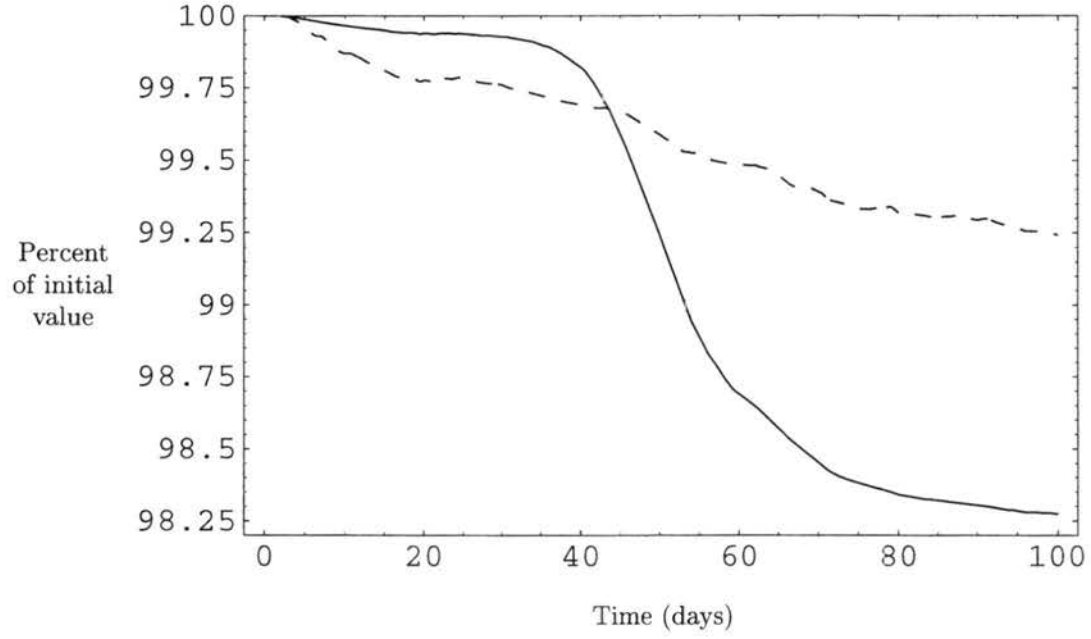

Figure 5.21: Time dependence of the kinetic energy (dashed line) and absolute enstrophy (continuous line) relative to their initial values for experiment 3.

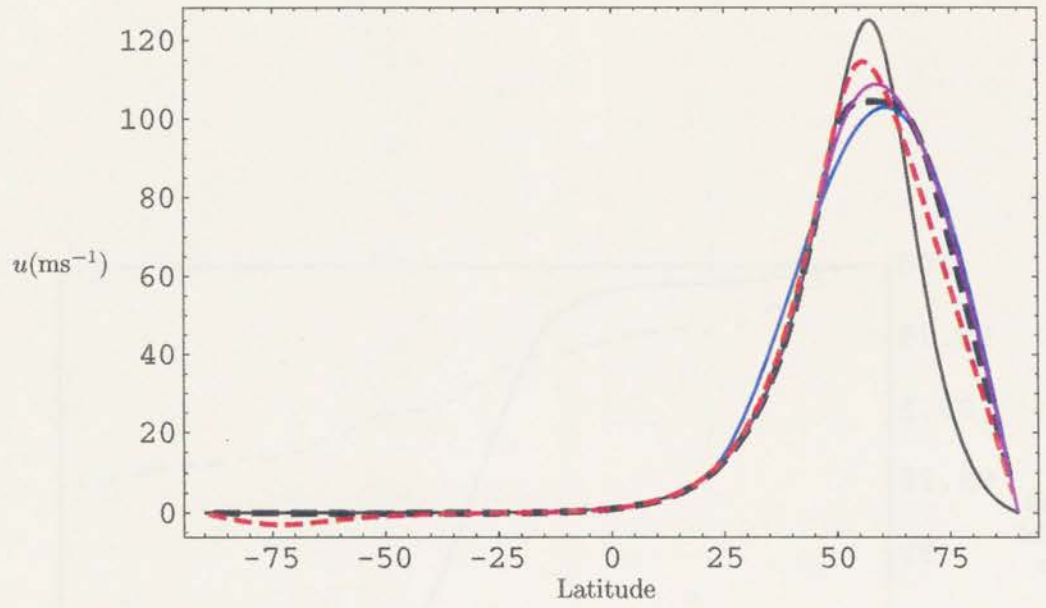

Figure 5.22: Zonal wind profiles. Initial condition: black solid line. Direct numerical integration at t=100 days: black dashed line. MinEF-$\mathcal{E}$: blue line. Maximum entropy prediction: red dashed line. MinEF-$\mathcal{M}$: violet line. Experiment 3.

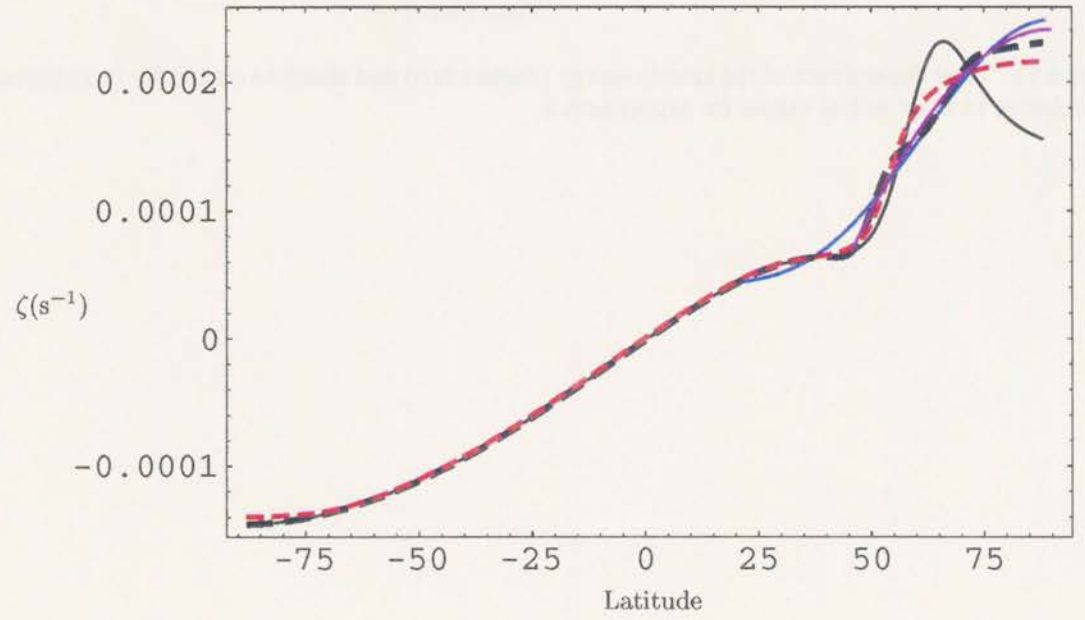

Figure 5.23: Same than Fig. 5.22 but for absolute vorticity profiles. Experiment 3.

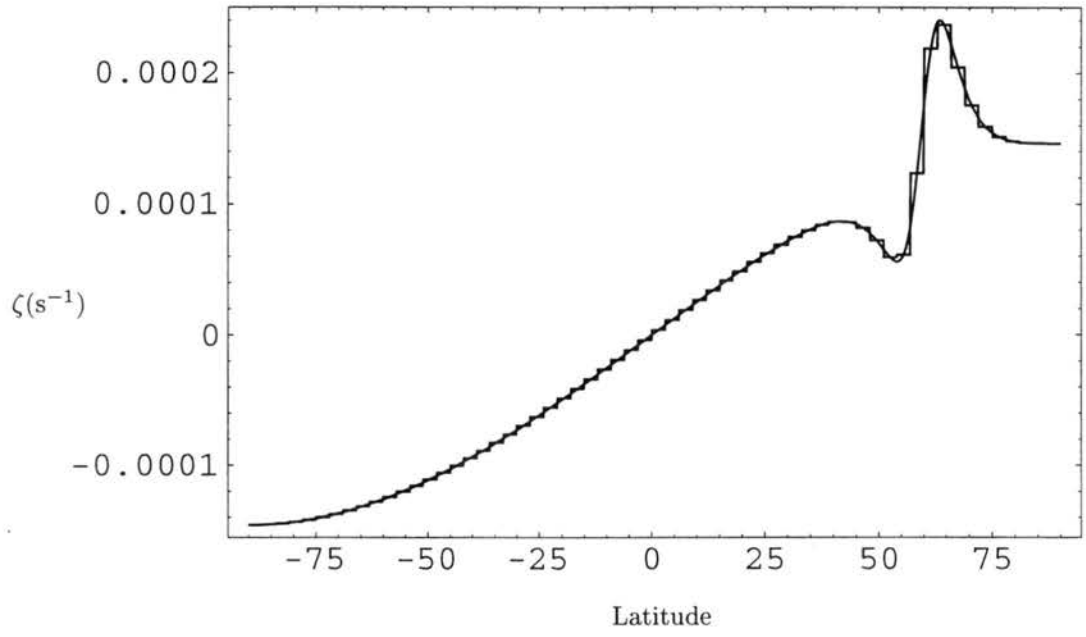

Figure 5.24: Initial absolute vorticity profiles for the direct numerical integration and for the maximum entropy theory (step-wise plot). Experiment 4.

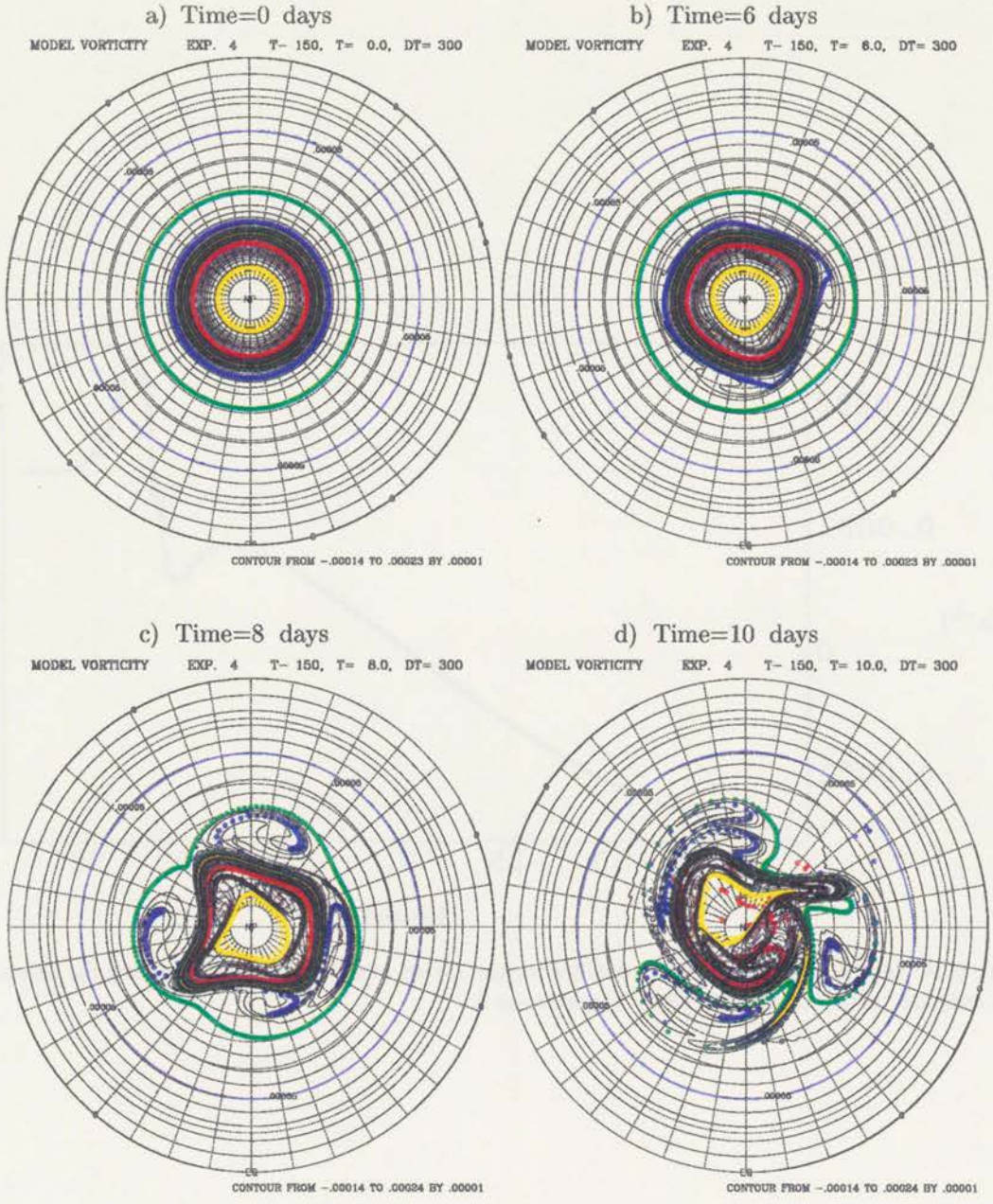

Figure 5.25: Northern Hemisphere polar stereographic plots of the absolute vorticity field (in s^{-1}) and tracer positions for selected snapshots of experiment number 4.

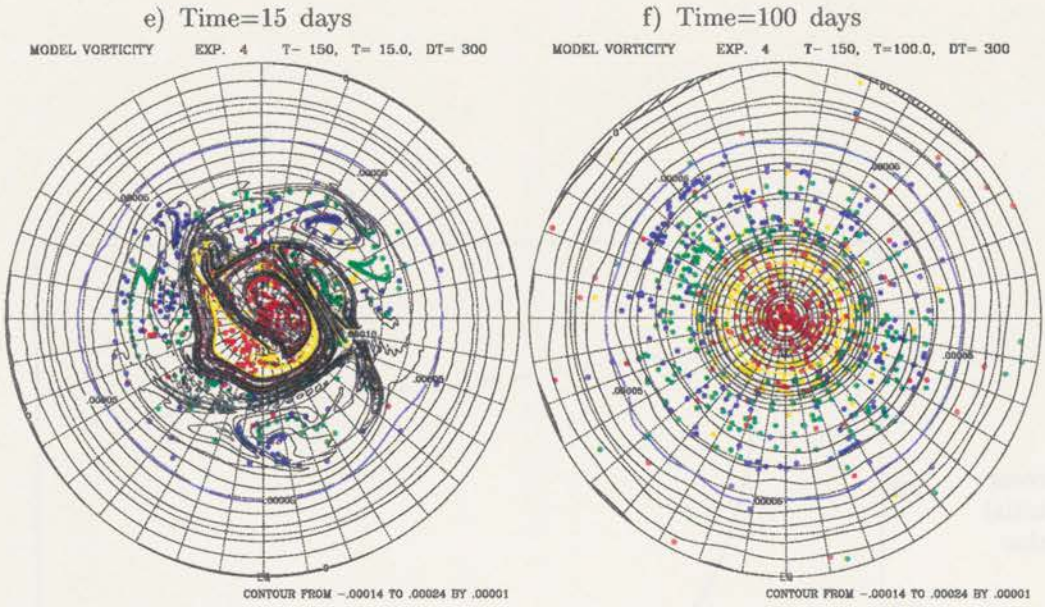

Figure 5.25: Continuation.

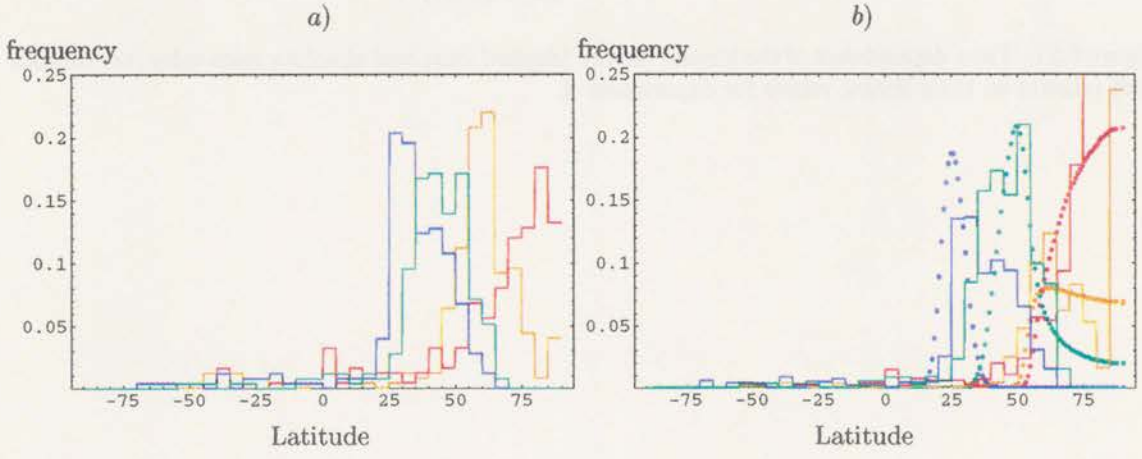

Figure 5.26: a) Tracer positions as a function of latitude for time = 100 days of direct numerical integration. Positions counted at 5 degrees latitude intervals. b) Same as a) but taking into account zonal coverage relative to initial position, displayed together with their respective density function. Experiment 4.

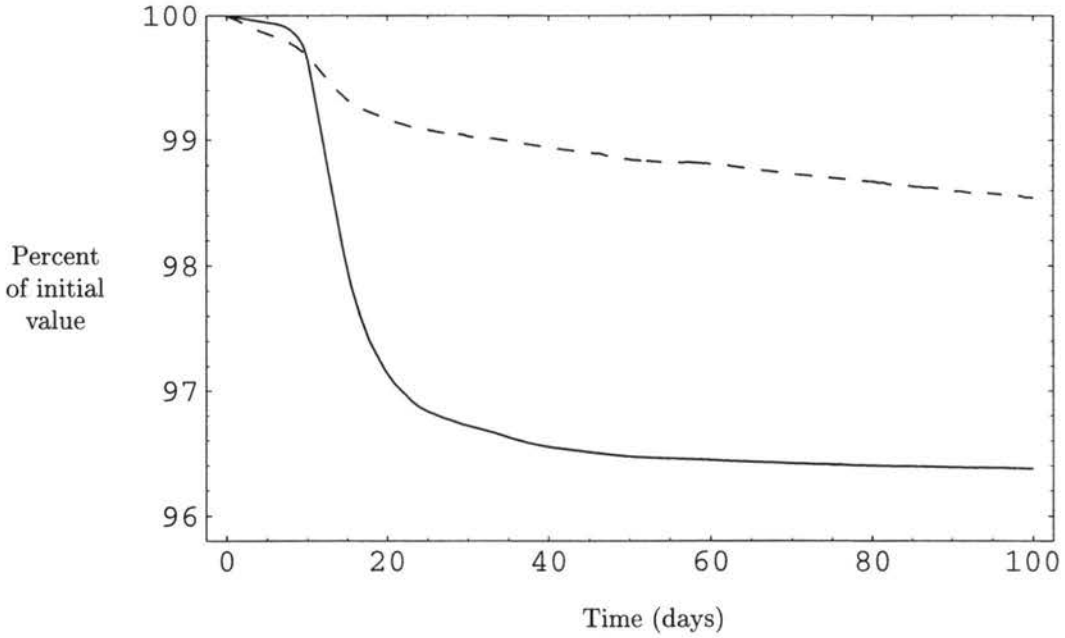

Figure 5.27: Time dependence of the kinetic energy (dashed line) and absolute enstrophy (continuous line) relative to their initial values for experiment 4.

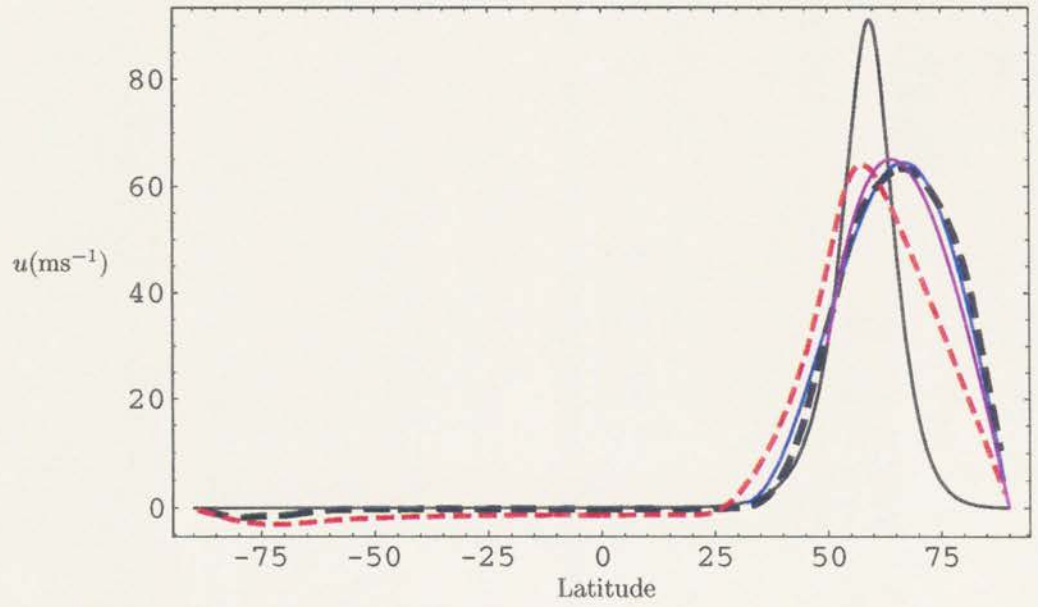

Figure 5.28: Zonal wind profiles. Initial condition: black solid line. Direct numerical integration at t=100 days: black dashed line. MinEF-$\mathcal{E}$: blue line. Maximum entropy prediction: red dashed line. MinEF-$\mathcal{M}$: violet line. Experiment 4.

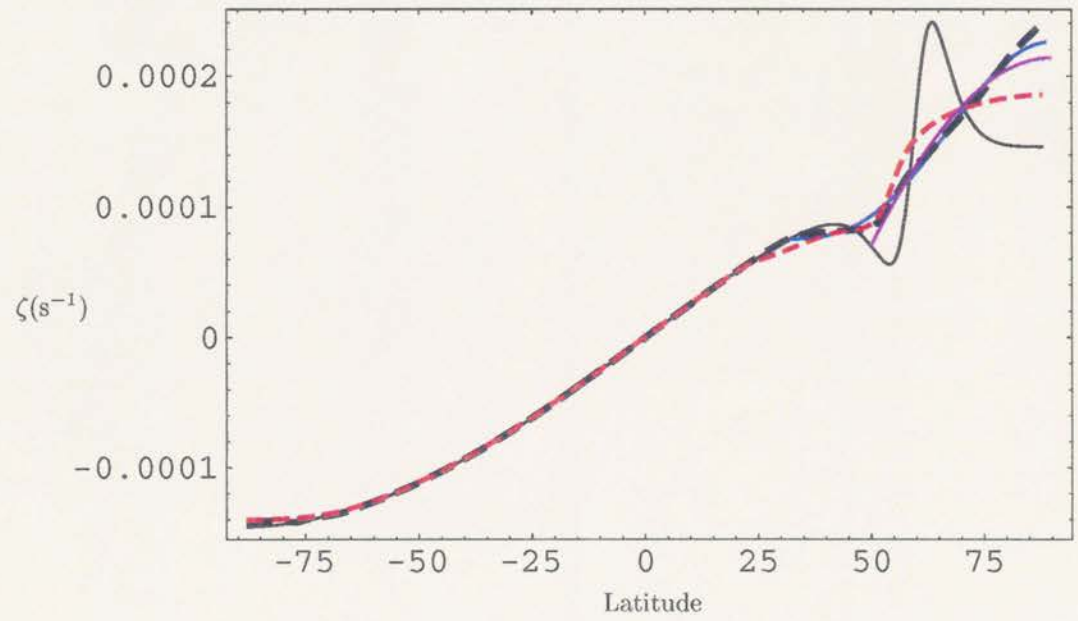

Figure 5.29: Same than Fig. 5.28 but for absolute vorticity profiles. Experiment 4.

Chapter 6

TROPICAL SHEAR LAYERS

6.1 Introduction

The Intertropical Convergence Zone (ITCZ) is a region of enhanced cloudiness and rainfall that constitutes the upward branch of the Hadley circulation. The conversion of latent and sensible heat to potential energy in the convecting systems of the ITCZ acts to stabilize the tropical troposphere, which is heated from the ocean below, and plays an important role in the atmospheric energy cycle, particularly in the transport of heat to the extratropics (Waliser and Somerville 1994).

On a global scale the ITCZ could be described as a near-solid convective cloud band encircling the Earth near the equator. Over the Atlantic and eastern Pacific oceans the ITCZ is characterized by a narrow well-defined cloud band. The ITCZ extending from the western Pacific to the Indian Ocean is broader in latitude with significantly more horizontal spatial variation. The central Pacific is a transition region between the different ITCZ structures to the east and west; it contains a southeastward-pointing extension called the South Pacific convergence zone. The ITCZs over tropical landmasses are broad and irregular, and are often disconnected from their oceanic counterparts by the convection-suppressing influence of cold water brought to the surface by coastal upwelling (Waliser and Gautier 1993).

Using a dataset derived from satellite observations, Waliser and Gautier (1993) studied the climatological characteristics of the ITCZ. They found that the ITCZ over the eastern Pacific and

Atlantic oceans remains primarily in the Northern Hemisphere throughout the year, with weak convection occurring south of the equator in the boreal spring. The bulk of the convection for these regions is between about 4°N and 12°N. The phase of the annual cycle in these regions lags behind the surface solar heating cycle by approximately two months, and each produces the most intense ITCZ in the boreal fall.

During the month of August and in regions of the tropical oceans such as the northwest and northeast Pacific and the northeast Atlantic, weak westerly or southwesterly surface winds are typically present of the equatorward side of the ITCZ (see, e.g., Gray, 1968, Hastenrath and Lamb, 1978), while easterly trade winds are present on the poleward side. The poleward side of this shear layer regions has been recognized (Gray, 1968) as a typical location of storm genesis. These regions are areas of large-scale surface cyclonic wind shear and, therefore, large-scale relative vorticity.

Nitta and Yanai (1969) analyzed latitudinal distributions of the average zonal velocity and absolute vorticity at various atmospheric levels over the Marshall Islands for June of 1958. They found that at the surface and at the 1000 mb level the gradient of absolute vorticity changed sign at about 8°N, therefore satisfying the necessary condition for barotropic instability. Using a linear model, Nitta and Yanai (1969) computed the growth rate of unstable disturbances, finding a wave-scale of about 2,000 km and an e-folding time of the most unstable wave of 5.2 days. In another study, Molinari et al. (1997) found a significant sign reversal in the meridional potential vorticity gradient during the summer of 1991 on the 310-K isentropic surface (near 700 mb) over the Caribbean Sea; as noted by Burpee (1972), this potential vorticity structure satisfies the Charney-Stern necessary condition for instability of the mean flow.

Agee (1972) proposed that the existence of appreciable cyclonic shear in the horizontal wind field has an important role for the spawning of wavelike perturbations in the ITCZ, and that these perturbations are capable of amplifying, breaking and shedding vortices that could be the initial stage of hurricane genesis, depending on the existence of favorable environmental conditions. Agee (1972) analyzed satellite images for the period May through July of 1969, finding a series or train of waves on the ITCZ that move toward the west at an estimated velocity of 250 n mi day^{-1} (463

km day^{-1}).

Wavelike perturbations or undulations of the ITCZ has been recognized (Nieto Ferreira and Schubert 1997) as the signature of easterly waves in the tropical troposphere. Easterly waves occur in the lower tropical troposphere and have typical wavelengths and speeds that range from 2000 to 4000 km and 5 to 8 ms^{-1} respectively (Nieto Ferreira and Schubert 1997).

Burpee (1972) studied the structure of easterly waves that form in the lower troposphere of North Africa, finding that these waves are directly related to the mid-tropospheric easterly jet that is situated over North Africa in the summer. Observations (e.g., Carlson 1969) suggest that African easterly waves probably form somewhere between 14°E and 30°W, and reach their largest amplitude at or near the west coast of Africa with most development occurring between 10°E and the west coast.

The African easterly jet has a maximum wind speed of about 15 ms^{-1} at about 15°N. Meridional cross-sections showing the typical zonal wind structure in the west African region during the northern hemisphere summer are shown in Fig. 6.1. The mean features are: a) A 600 mb African easterly jet (AEJ) at about 15°N with a peak strength of 12-15 ms^{-1}; b) an upper-level tropical easterly jet at about 200 mb and equatorward of the AEJ; c) a low-level monsoon westerly flow south of this; d) a mid-latitude westerly jet to the north; e) a near-surface easterly flow north of the AEJ, and f) a second 600 mb easterly jet in the southern hemisphere (Thorncroft and Hoskins 1994a).

Simmons (1977) performed a linear stability analysis for an easterly lower tropospheric jet, finding that the most unstable disturbance has a growth rate of 0.27 day^{-1}, a wavelength close to 4000 km and a phase speed of about 9ms^{-1}.

Thorncroft and Hoskins (1994a) re-examined the analytically defined flow used by Simmons (1977). They used a baroclinic spectral model with horizontal resolution of triangular truncation T95, giving a resolvable scale of about 67 km and 15 sigma levels in the vertical resolution. The most unstable mode for a particular wavenumber was found in this study by integrating the primitive equations on a hemisphere, using as initial condition the zonal flow of Simmons (1977) and a small

perturbation confined to the wavenumber of interest; the perturbation is allowed to grow while keeping the zonal mean constant. The growth rate obtained is similar to that of Simmons (1977) with a maximum at zonal wavenumbers 10 and 11. At a latitude of 15°N, $m = 11$ is equivalent to a wavelength of about 3500 km; the growth rate for $m = 11$ is 0.28 days^{-1} and it has a westward phase speed of 6.8° per day, implying a period of 4.8 days.

The linear global energy conversions for wavenumber $m = 10$ were also studied by Thorncroft and Hoskins (1994a), with the conclusion that the dominant energy conversion is through the barotropic term, with a ratio 5.6 to 1 with respect to the baroclinic term.

Using a nonlinear model Thorncroft and Hoskins (1994b) examined the finite amplitude behaviour of an easterly wave. The nonlinear easterly wave energetics and structure differ from those of the linear study. The easterly wave is initially dominated by barotropic energy conversions, but later grows mainly through baroclinic energy conversions; these results are in agreement with those found in GATE studies over west Africa and in GCM integrations.

Nieto Ferreira and Schubert (1997) proposed that ITCZ undulation an breakdown results from a convectively modified form of combined barotropic and baroclinic instability of the mean flow. They used a nonlinear shallow-water model on the sphere to simulate barotropic aspects of ITCZ breakdown; their results suggest that ITCZ breakdown may play a role in producing the observed tendencies for tropical storms to cluster in time and form poleward of the central latitude of the ITCZ.

In this chapter, we will study the evolution of tropical shear layers using the barotropic non-divergent model described in chapter 2, and we will compare the equilibrium state for this kind of flow with the predictions given by the maximum entropy and minimum enstrophy theories.

6.2 Experiments

The initial condition that we have selected to produce a zonally symmetric tropical shear layer is given by a cosine-shaped vorticity strip placed in tropical regions of the Northern Hemisphere:

$$\zeta(\lambda,\phi) = \begin{cases} A\left[1+\cos\left[\frac{2\pi(\phi-\phi_o)}{b}\right]\right] + 2\Omega\sin\phi - c + \zeta_d(\lambda,\phi) & \text{if } |\varphi-\phi_o| \le \frac{b}{2} \\ 2\Omega\sin\phi - c + \zeta_d(\lambda,\phi) & \text{otherwise,} \end{cases} \tag{6.1}$$

where A is the magnitude of the vorticity strip, ϕ_o the latitude where it is centered, b its width, $\zeta_d(\lambda,\phi)$ the disturbance given by (5.4), and c a constant chosen in such a way that the absolute vorticity integrated over the whole sphere is zero.

This initial condition is designed to model the behaviour of a zonally symmetric ITCZ without any other major flow feature on the sphere. This idealized condition was chosen to isolate the dynamical behaviour of the ITCZ and its equilibrium state, while a more realistic initial condition could mask the fundamental processes we are trying to understand.

In this section we present the results of four experiments with different parameter values in (6.1), which are summarized in Table 6.1. The vorticity field of (6.1) produces a shear zone with westerlies on the south side of the local vorticity maximum and easterlies northward. Positions for the westerly/easterly maxima as well as their magnitude are also shown in Table 6.1.

6.2.1 Experiment 5

Figure 6.2 shows the initial absolute vorticity profile for the direct numerial integration and the maximum entropy flow. For the time integration, the cosine-shaped strip is centered at 7.5°N with an amplitude (A in equation 6.1) of $2.5 \times 10^{-5}\text{s}^{-1}$ and a width of 8° latitude. This initial condition creates a shear of the order of 20.8ms^{-1} in a region of about 7° latitude from which the wind decreases monotonically towards zero at the poles (see Fig. 6.7).

The linear stability analysis of section 2.1 is applied to this initial condition. Figure 6.3 shows the results for the real and imaginary parts of the complex frequencies (σ_r and σ_i respectively) as a function of the zonal wavenumber m, for m between 1 and 10. Ill-conditioned matrices for the linear

stability analysis were obtained for zonal wavenumbers $m > 10$, so our conclusions in this respect are restricted to the range $1 \leq m \leq 10$. Wavenumber 8 was the most unstable with and e-folding time $\tau_i = 3.89$ days and period $\tau_r = 37.2$ days (See Table 6.2).

For the nonlinear time integration we used a triangular truncation T213, with a timestep of 600s and hyperdiffusion coefficient $\nu = 4 \times 10^{13} \mathrm{m}^4\mathrm{s}^{-1}$, which corresponds to an e-folding time of the highest total wavenumber $N = 213$ of $\tau_{213} = 5.5$ hours.

Figure 6.4a is a Northern Hemisphere polar stereographic projection of the initial absolute vorticity field. This run includes the calculation of 1000 air parcel trajectories initially uniformily distributed in two latitudinal rings, 500 of them at the relative maximum of the vorticity field ($\phi = 7.5^o$N) shown in red, and the other 500 green parcels just north of the vorticity strip, at $\phi = 11.5^o$N.

At $t = 11$ days some deformation of the vorticity lines is present; this behaviour continues with folding, elongation and breaking of absolute vorticity contours and with the creation of a series of vortices with relatively high absolute vorticity and red parcels in their core, and with the advection of green air parcels equatorward (Fig. 6.4c,d). The whole pattern of vortices tends to move towards the west and slightly towards the north, while the instability of the original zonal flow is moving towards the east. During the simulation, there is evidence of at least three vortex mergers; the beginning of one of them is seen at the top of Fig. 6.4d.

At $t = 25$ days the whole shear layer has been broken into 11 vortices, one merger had occurred and a secondary breakown of a zonally elongated vortex has been detected. Most of the activity takes place in the band between about 30°N and the Equator. During the rest of the simulation, two other mergers occurred with the ejection of vorticity filaments; mutual vortex orbiting is also present without final merging.

The vortices continue to move westward and suffer major deformations until they lose identity, and by about $t = 50$ to 60 days the colored air parcels have mixed over the whole tropical region. At the end of the simulation ($t = 100$ days) no major vortex is present and the absolute vorticity

field is relatively zonally symmetric. Most of the colored air parcels are between 10 and 20°N, but there are a few which have traveled into the midlatitudes.

Tracer positions as a function of latitude at $t = 100$ days are shown in Fig. 6.5a; the counting is done within 5^o latitude rings dividing by the total number of parcels (500) of each color. The maximum frequency of red parcel positions is between 10 and 25°N, north of their initial position at 7.5°N; most of the green parcel positions are between 5 and 15°N. Figure 6.5b shows the histogram of the colored air parcels positions at $t = 100$ days but taking into account the zonal coverage relative to the initial position; the respective density functions obtained from the maximum entropy solution are also plotted. The density function for the green parcels is in good agreement with its respective histogram, while the maximum of the density function for the red air parcels is displaced about 5^o north of the respective histogram.

A plot of the time series of total kinetic energy change and total absolute enstrophy change is shown in Fig. 6.6; the kinetic energy has a decay of 0.43%, at $t = 100$ days, while the absolute enstrophy decays 0.36%. Since the energy decay is larger than the enstrophy decay, this is an indication that the diffussion we are using in the time integration model has a considerable effect on the evolution of the flow, and therefore this numerical experiment is not consistent with the selective decay hypothesis discussed in chapter 4. However, we are still going to compare the minimum enstrophy predictions with the direct numerical integration and see what is the predictive skill of the theory for this kind of flow.

Since the whole flow over the sphere is mostly produced by the vorticity strip (which is relatively small in meridional extent) placed at the tropics, a satisfactory initial condition for the maximum entropy code with values of energy, angular momentum and circulation close enough to the smooth profile (Fig. 6.2) was obtained with a relatively high number of vorticity levels, which in this case was 60. A lower number of vorticity levels (~ 30) produced a flow that was not representative of the initial condition.

The zonal wind profiles of three different predictions together with the initial condition and the zonal average of the direct numerical integration at $t = 100$ days are presented in Fig. 6.7. The

direct numerical integration (black dashed line) shows some changes compared to the initial condition (black solid line). The initial separation of 7^o of latitude between the maximum and minimum of the zonal wind, has increased to a separation of 16.8^o latitude, with most of it towards the north (the zonal wind minimum is at 18.8^oN); the prediction that best captures this change is MinEF-$\mathcal{E}$ with two edges (green line), but its velocity minimum is about 1.4 ms^{-1} lower than the time integration line.

The other major change to the initial flow produced by the direct numerical integration is at high latitudes in the Southern Hemisphere; the flow there, initially westerly, changed to weak easterlies of the order of $2ms^{-1}$ at about 78^oS. The maximum entropy prediction gives a similar change of the flow in the Southern Hemisphere, but its prediction is consistently more easterly by 1 to 2 ms^{-1}. The maximum entropy prediction and MinEF-$\mathcal{M}$ with one edge showed little skill predicting the equilibrium state of the zonal wind for the northern hemisphere. The MinEF-$\mathcal{M}$ with two edges gives a solution that is no different that the initial condition, while the MinEF-$\mathcal{E}$ with one edge (not shown) gives a solution with irrealistic oscillations in the zonal wind that clearly violates the conservation of angular momentum.

A comparison among the absolute vorticity profiles is presented in Fig. 6.8, where it can be seen that the predictions and the time integration lines remove the sign reversal of the absolute vorticity gradient, therefore stabilizing the flow. The best prediction in the equatorial regions of the Northern Hemisphere is that of MinEF-$\mathcal{E}$ with two edges. There is a good agreement between maximum entropy and the time integration in the Southern Hemisphere, while in the Northern Hemisphere MinEF-$\mathcal{M}$ with one edge and maximum entropy have some differences with the direct numerical integration line.

6.2.2 Experiments 6, 7 and 8

Three other experiments were performed by changing the magnitude of the vorticity strip (A), its position (ϕ_o) and its width (b), which produced variations in the magnitude and position of the zonal wind maximum and minimum (Table 6.1), all of them similar to the kind of variations observed in

tropical tropospheric regions of the Earth. Nonlinear time integrations of the nondivergent numerical model of chapter 2 were performed for these three experiments using a triangular truncation T170 with timestep of 600s and hyperdifussion coefficient $\nu = 9 \times 10^{13}\mathrm{m}^4\mathrm{s}^{-1}$, which corresponds to an e-folding time of the highest total wavenumber $N = 170$ of τ_{170}= 6 hours.

The nonlinear behaviour for experiments 6, 7 and 8 was quite similar to experiment 5, so plots are not shown. However, there were some detectable differences such as the initial folding of vorticity contours being detected 2 and 3 days earlier in experiments 6 and 7 respectively. In experiment 6, which has the sharpest vorticity strip, there were a total of 12 vortices after the breakdown of the shear layer, instead of 11 as in experiment 5. The kinetic energy decay was 1.55%, 1.00% and 1.05% for experiments 6, 7 and 8, with respective absolute enstrophy decay of 0.87%, 1.30% and 0.39%.

The comparison between the colored parcel positions at $t = 100$ days of simulation and the respective density functions obtained from the maximum entropy prediction, have a similar spatial structure that the one shown in Fig. 6.5b, except that the red solid line is narrower and with higher peak in experiments 6, 7 and 8, which is the reflection of some clusters of red parcels in the numerical simulation. That behaviour was also observed in a run of experiment 5 at resolution T170 (the results presented in section 6.2.1 were at resolution T213).

Comparisons for the zonal average of the nonlinear time integration at $t = 100$ days and the predictions of maximum entropy theory, MinEF-$\mathcal{E}$ with two edges and MinEF-$\mathcal{M}$ with one edge for experiments 6, 7 and 8 are shown in Figs. 6.9 to 6.14. In general, MinEF-$\mathcal{E}$ with two edges predicts that the easterlies move northward by about 10^o of latitude, behaviour that is consistent with the nonlinear time integration, especially in experiment 8; but since MinEF-$\mathcal{E}$ with two edges predicts just local changes, it fails to reproduce the changes that happen in the flow in regions close to the poles. The zonal wind predictions given by maximum entropy showed some ability detecting the changes that occurred in the flow in the southern hemisphere; however, it did less well in the Northern Hemisphere. The zonal wind given by MinEF-$\mathcal{M}$ with one edge was the poorest prediction of the three plotted.

For the absolute vorticity profiles, the predictions of maximum entropy, MinEF-$\mathcal{E}$ with two edges

and MinEF-$\mathcal{M}$ with one edge remove the reversal of the absolute vorticity gradient, being consistent with the direct numerical integration profile. However, none of the predictions have close agreement with the direct numerical integration.

6.3 Discussion

In this chapter we have studied nonlinear simulations of tropical shear layers and compared them with the predictions of maximum entropy and minimum enstrophy theories. The numerical simulations, such the one presented in Fig. 6.4, have a behaviour that is consistent with observations of the intertropical convergence zone (see, e.g., Agee 1972, and Nieto Ferreira and Schubert 1997). In general, the theoretical predictions were deficient for the experiments discussed; however they showed some ability at detecting localized changes in the flow, as in the case of MinEF-$\mathcal{E}$ with two edges, which was able to capture the northward displacement of the easterly wind maximum, and the maximum entropy prediction, which captured changes in the flow for the southern hemisphere. The main factors that we think contributed to poor theoretical predictions for the experiments 5 to 8 are discussed below.

The scale of the vorticity strip: The initial global wind distribution is a result of the vorticity strip placed at low latitudes which has a width at its base of 6 or 8 degrees of latitude. The maximum entropy code showed a substantial sensitivity to conditions of this type, being unable to reproduce such a flow with a discretized vorticity field of 30 levels; besides a strong sensitivity of the flow invariants (total kinetic energy and angular momentum) with respect to small variations in the parameters controling the amplitude, width and location of the vorticity strip.

The effect of diffusion and resolution in the nonlinear time integration: For three out of the four numerical simulations of this chapter we have seen that the absolute enstrophy decay is larger than the kinetic energy decay; therefore these experiments are not consistent with the selective decay hypothesis that gave origin to the minimum enstrophy theory. Some improvement of the predictions with respect to the numerical simulations was observed in experiment 5 when comparing a run at

resolution T213 (where the kinetic energy decayed 0.43%) with a run at T170 (with a kinetic energy decay of 1.2%).

Deviations from axisymmetry: The theoretical predictions presented consider a flow that is zonally symmetric and we are comparing them with the direct numerical integration after 100 days of evolution, which has some energy and angular momentum in its meridional wind component.

Table 6.1: Summary of parameter values for the experiments 5 to 8: A, ϕ_o and b; together with the resultant maximum zonal wind (u_{max}), latitude of maximum zonal wind (ϕ_{max}), minimum zonal wind (u_{min}) and latitude of minimum zonal wind (ϕ_{min}).

Exp. number	A ($\times 10^{-5}$s^{-1})	ϕ_o (^{o})	b (^{o})	u_{max} (ms^{-1})	ϕ_{max} (^{o}N)	u_{min} (ms^{-1})	ϕ_{min} (^{o}N)
5	2.50	7.5	8.0	11.8	3.9	-9.0	10.9
6	3.65	10.0	6.0	13.6	7.4	-9.5	13.0
7	3.65	10.0	8.0	17.8	6.7	-12.5	13.7
8	2.50	10.0	8.0	12.2	6.7	-8.6	13.7

Table 6.2. e-folding time τ_i and period τ_r as a function of zonal wavenumber m for unstable modes obtained in the linear stability analysis for experiment number 5.

e-folding time τ_i (days)

m	1	2	3	4	5	6	7	8	9	10
Exp. 5	46.25	23.39	16.14	12.12	10.76	8.77	7.96	3.89	7.79	7.14

Period τ_r (days)

m	1	2	3	4	5	6	7	8	9	10
Exp. 5	905.5	559.9	399.6	516.4	1030.8	1216.6	142.1	37.2	5.6	4.9

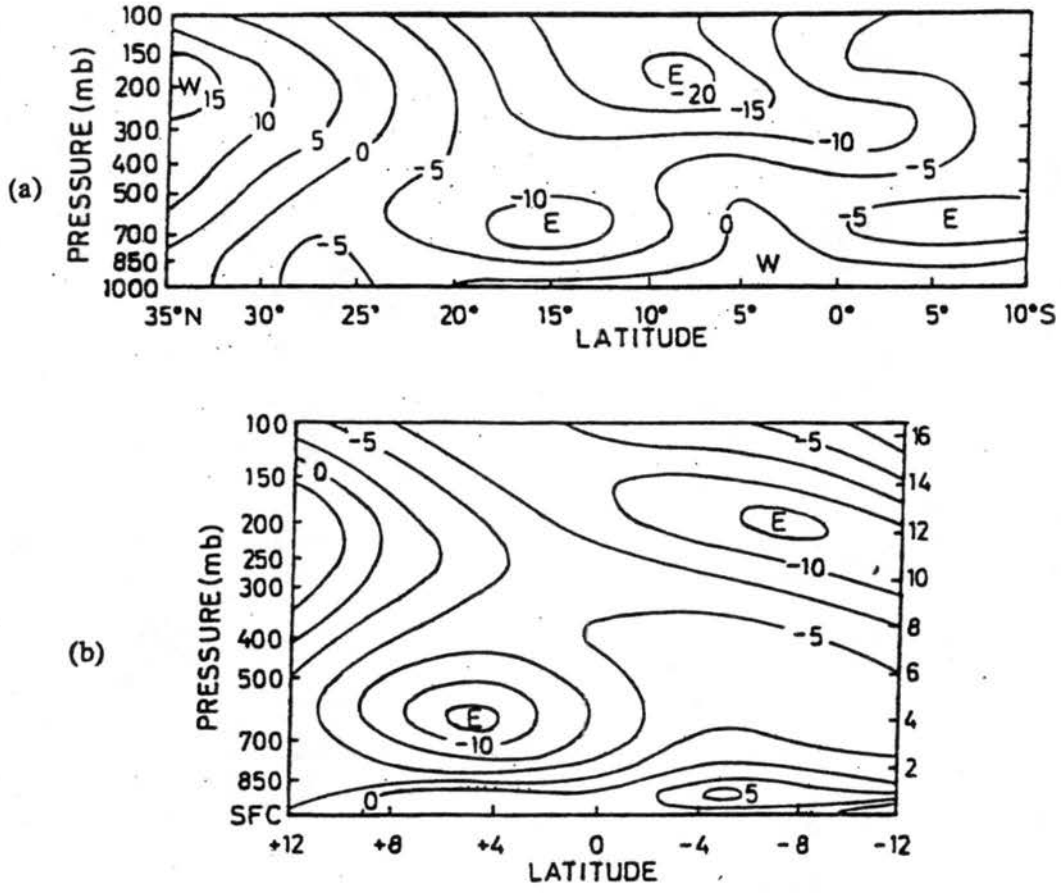

Figure 6.1: Mean zonal wind over west Africa from two observational studies: a) the mean zonal wind for August at 5°E from Burpee (1972), contour interval 5 ms^{-1}; b) the mean zonal wind from GATE between 23 August and 19 September 1974 from Reed et al. (1977), contour interval 2.5 ms^{-1}. This is averaged between 10°E and 31°W; the 'zero' latitude corresponds to the average latitude of a disturbance path which was 11°N over land and 12°N over the ocean. Taken from Thorncroft and Hoskins (1994a).

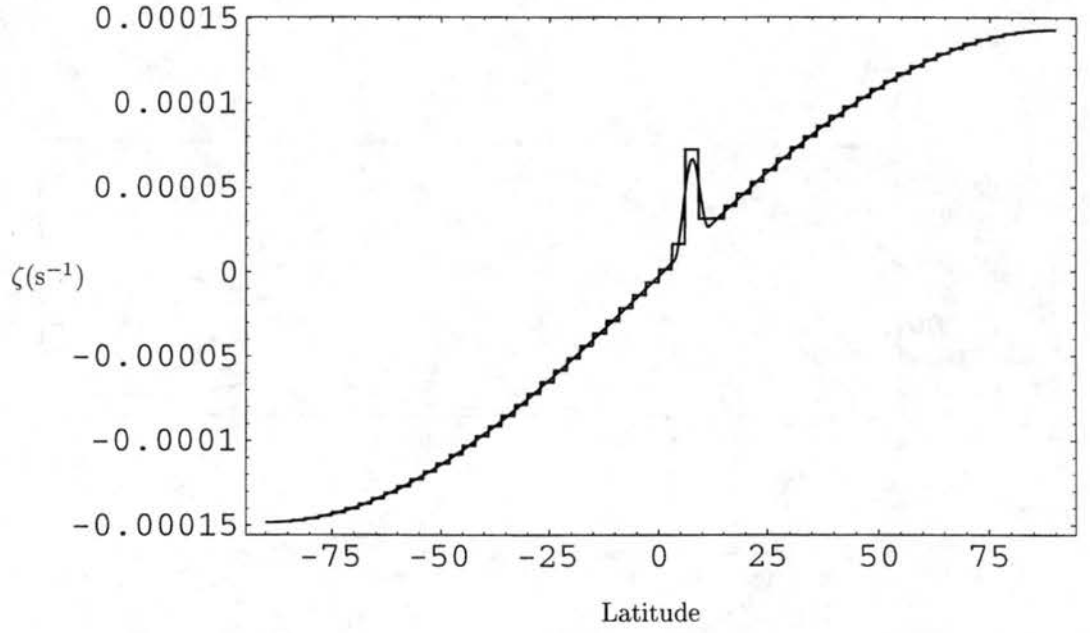

Figure 6.2: Initial absolute vorticity profiles for the direct numerical integration and for the maximum entropy theory (step-wise plot). Experiment 5.

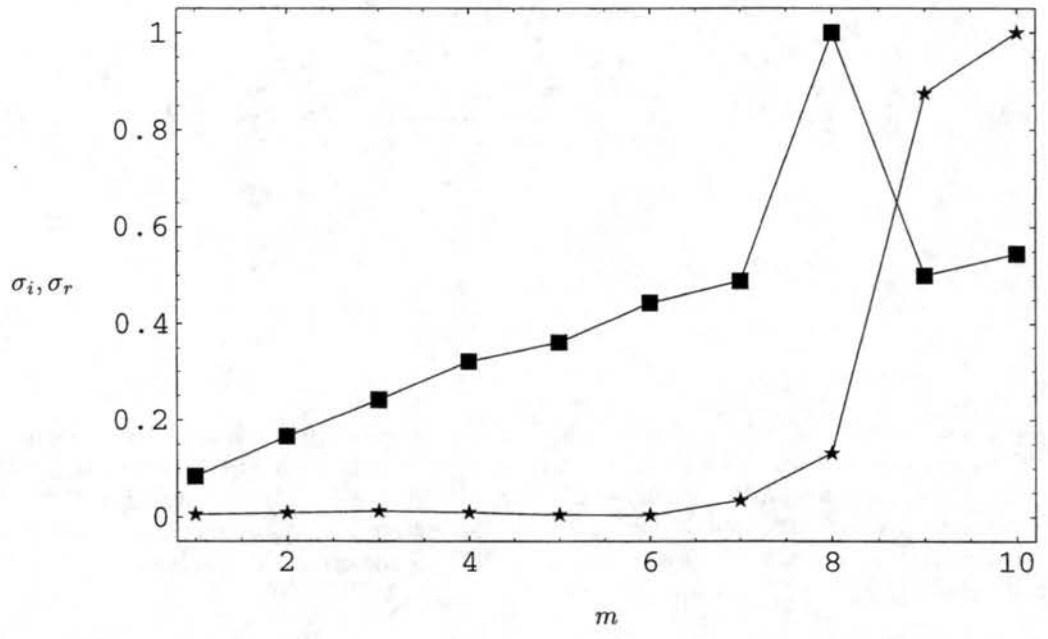

Figure 6.3: Linear stability analysis results for the normalized frequencies: Normalized σ_i (squares) and σ_r (stars) as a function of zonal wavenumber m. Experiment 5.

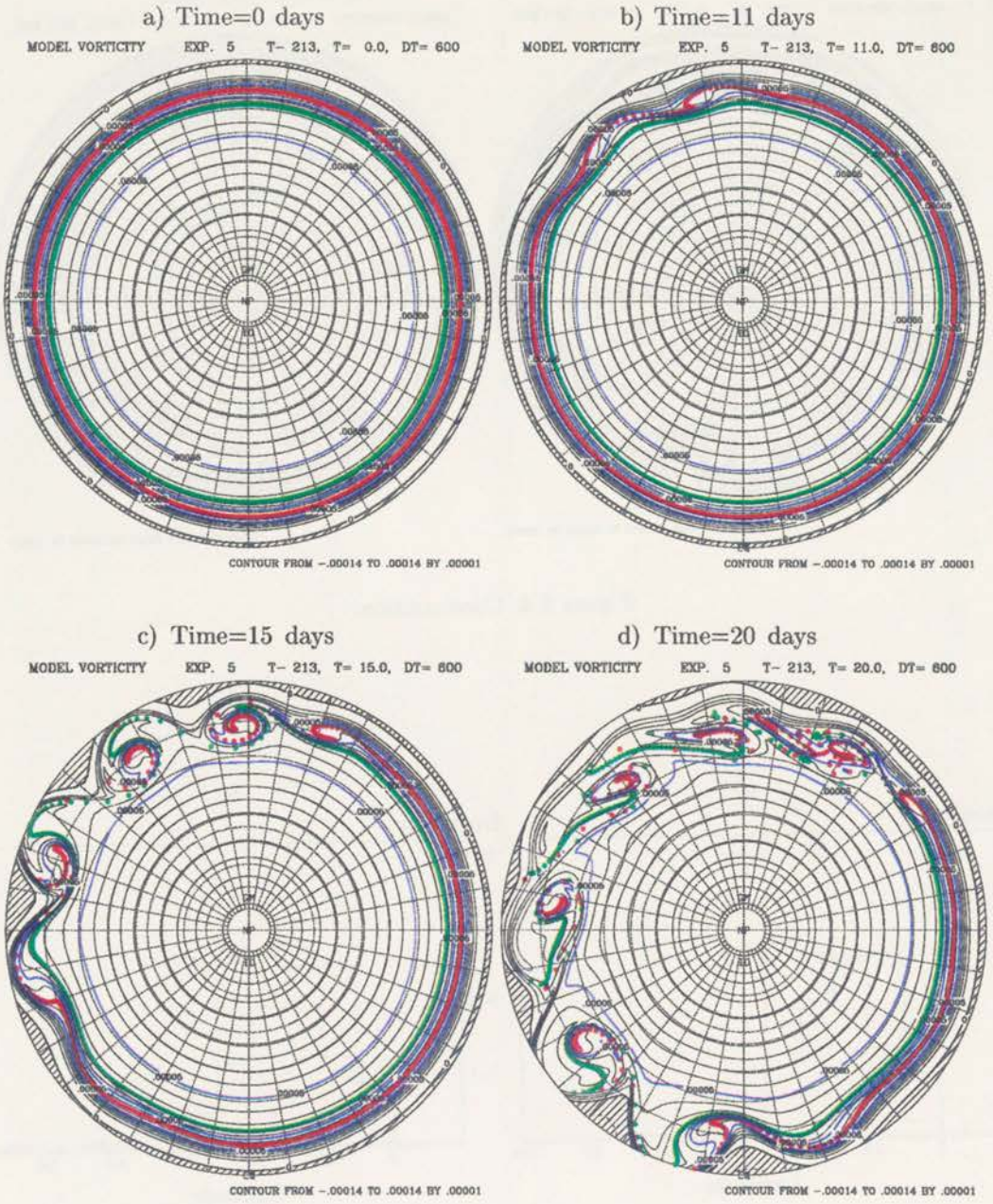

Figure 6.4: Northern Hemisphere polar stereographic plots of the absolute vorticity field (in s^{-1}) and tracer positions for selected snapshots of experiment number 5.

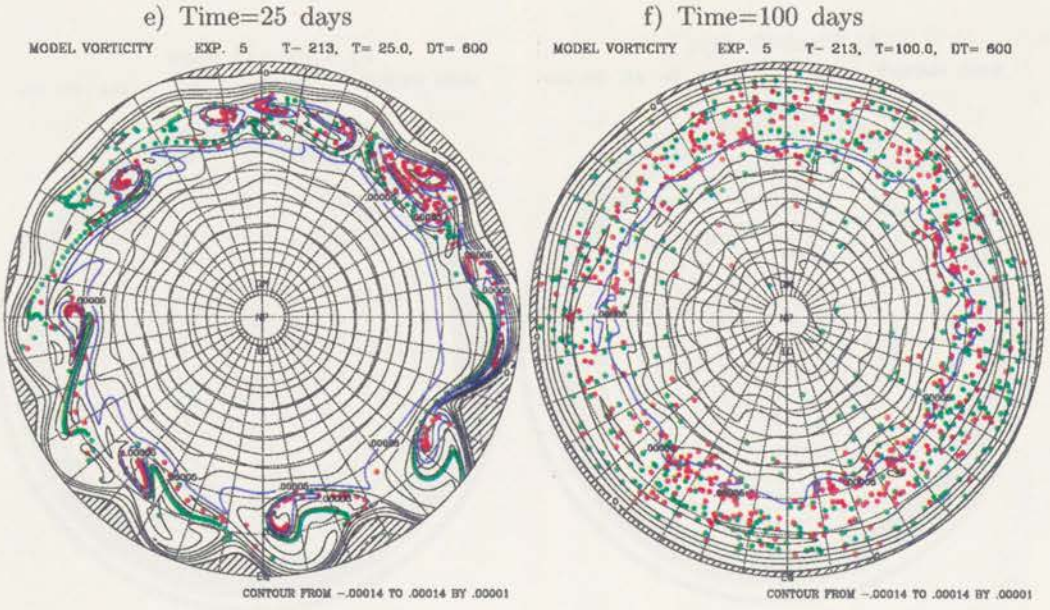

Figure 6.4: Continuation.

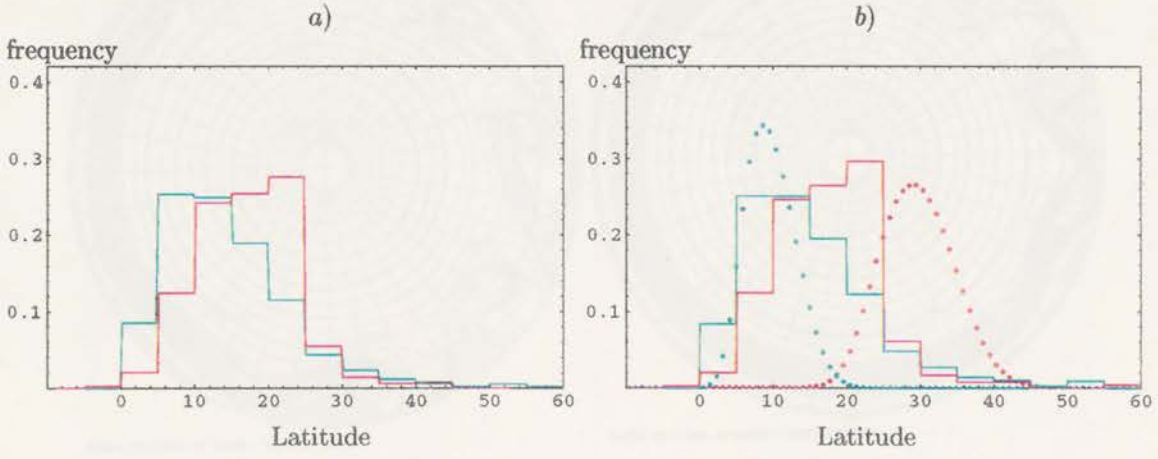

Figure 6.5: a) Tracer positions as a function of latitude for time = 100 days of direct numerical integration. Positions counted at 5 degrees latitude intervals. b) Same as a) but taking into account zonal coverage relative to initial position, displayed together with their respective density function. Experiment 5.

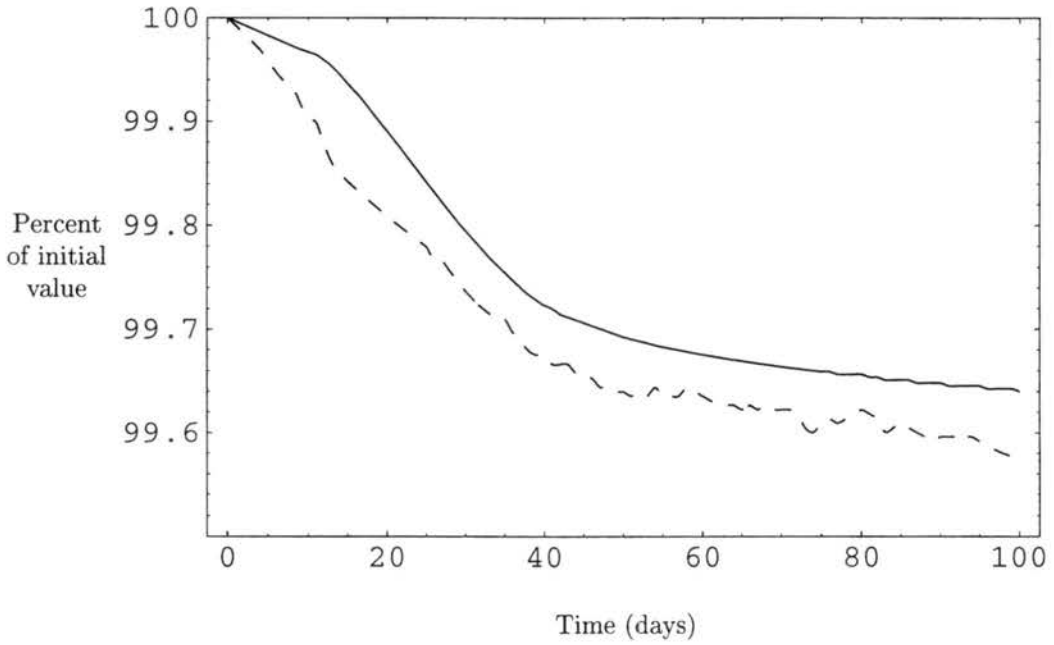

Figure 6.6: Time dependence of the kinetic energy (dashed line) and absolute enstrophy (continuous line) relative to their initial values for experiment 5.

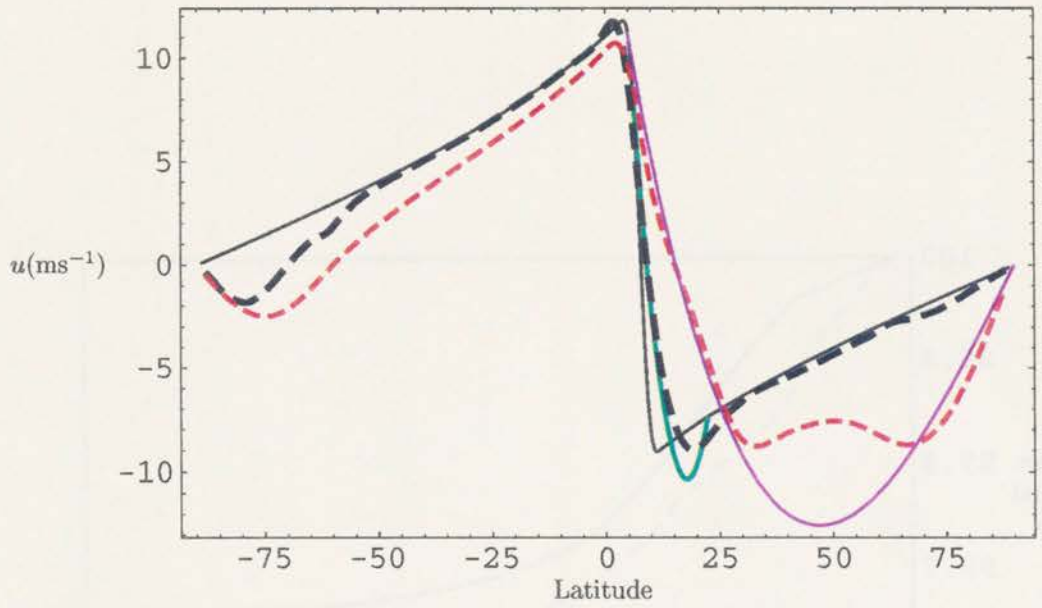

Figure 6.7: Zonal wind profiles. Initial condition: black solid line. Direct numerical integration at t=100 days (zonal average): black dashed line. MinEF-$\mathcal{E}$ with two edges: green line. Maximum entropy prediction: red dashed line. MinEF-$\mathcal{M}$ with one edge: violet line. Experiment 5.

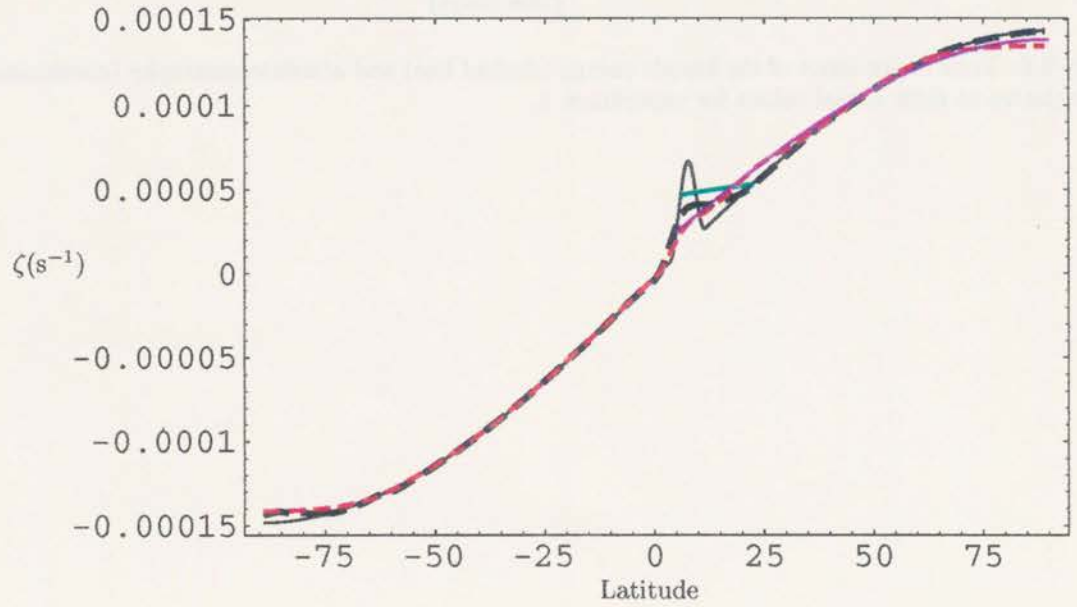

Figure 6.8: Same than Fig. 6.7 but for absolute vorticity profiles. Experiment 5.

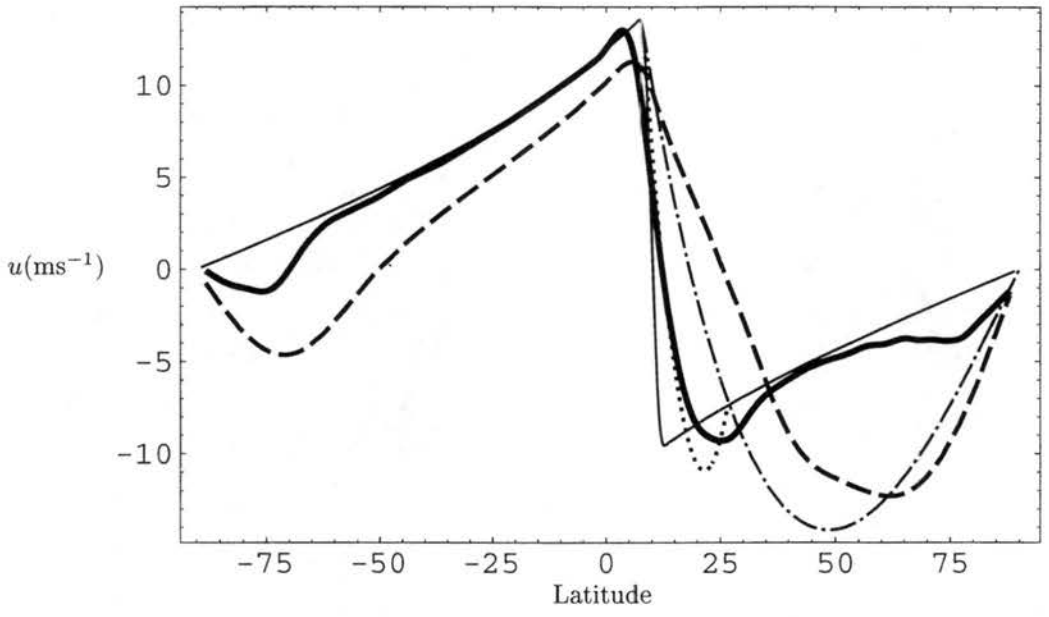

Figure 6.9: Zonal wind profiles. Initial condition: thin solid line. Direct numerical integration at t=100 days (zonal average): thick solid line. MinEF-$\mathcal{E}$ with two edges: dotted line. Maximum entropy prediction: dashed line. MinEF-$\mathcal{M}$ with one edge: dash-dotted line. Experiment 6.

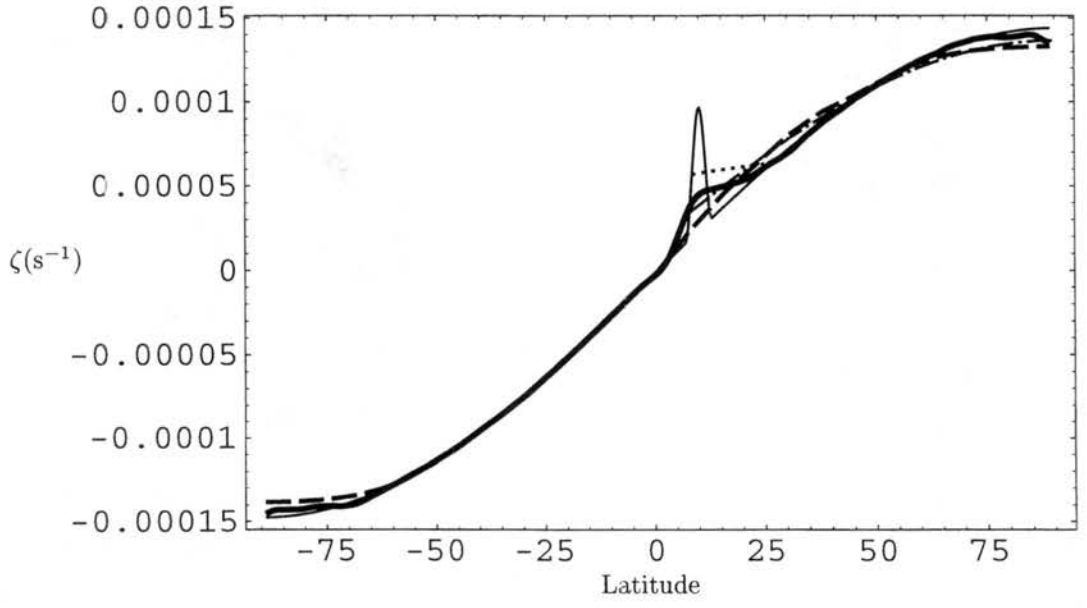

Figure 6.10: Same than Fig. 6.9 but for absolute vorticity profiles. Experiment 6.

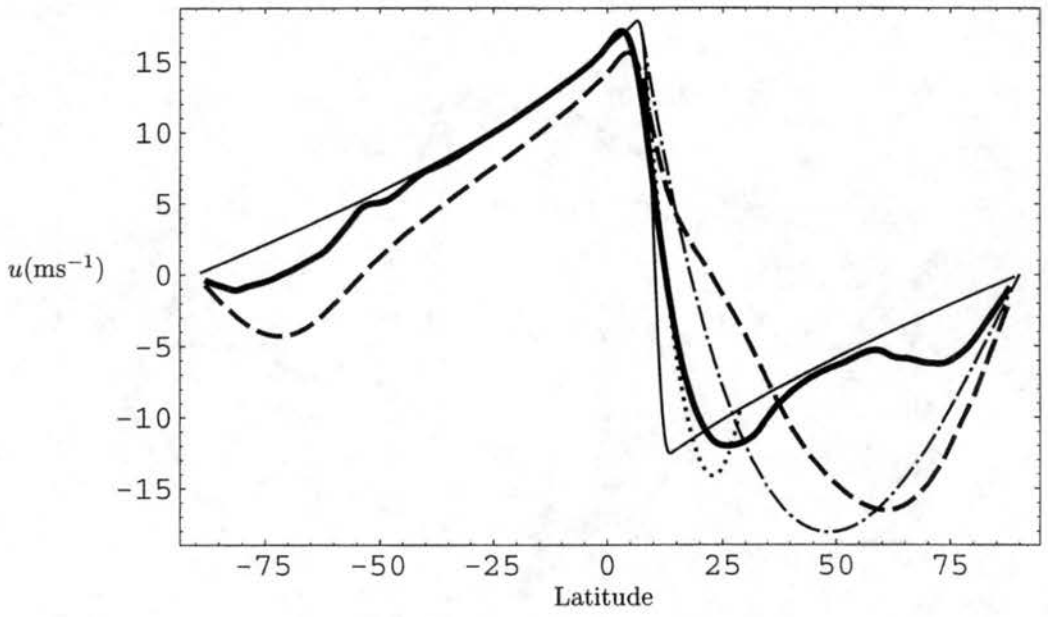

Figure 6.11: Zonal wind profiles. Initial condition: thin solid line. Direct numerical integration at t=100 days (zonal average): thick solid line. MinEF-$\mathcal{E}$ with two edges: dotted line. Maximum entropy prediction: dashed line. MinEF-$\mathcal{M}$ with one edge: dash-dotted line. Experiment 7.

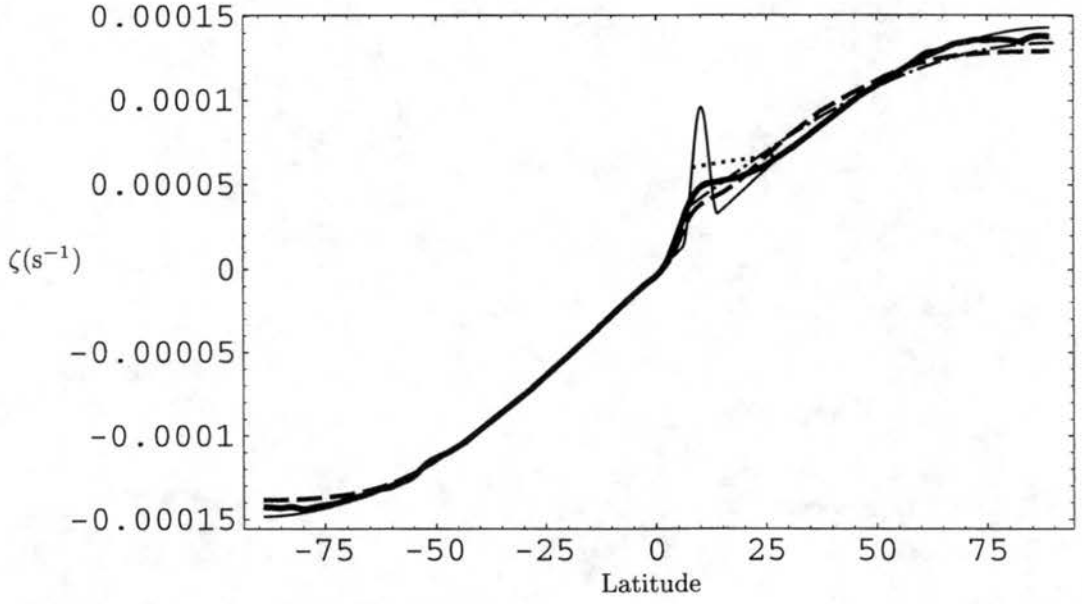

Figure 6.12: Same than Fig. 6.11 but for absolute vorticity profiles. Experiment 7.

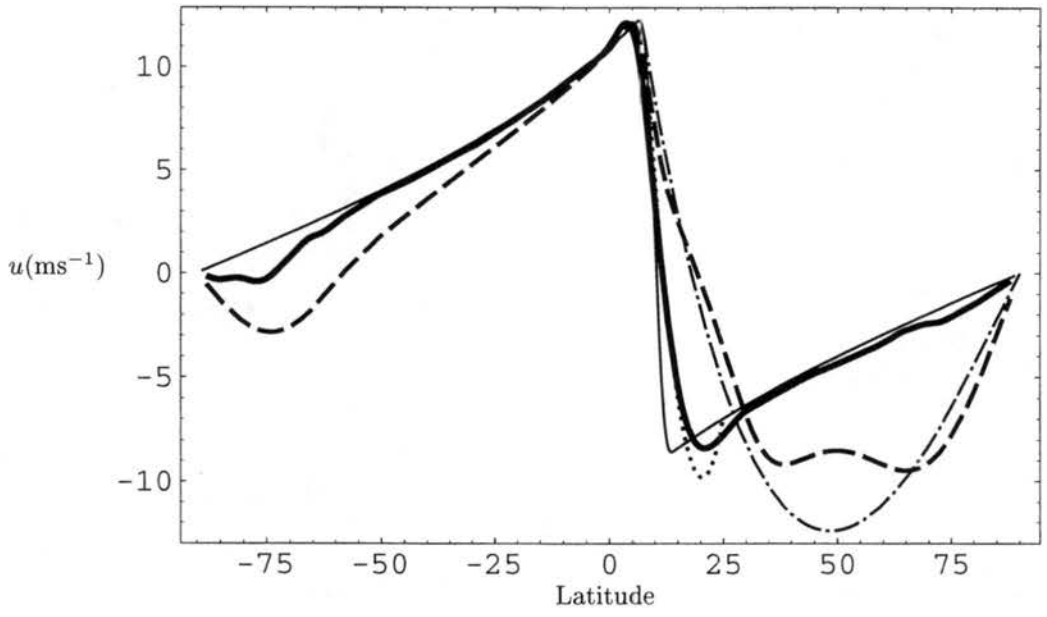

Figure 6.13: Zonal wind profiles. Initial condition: thin solid line. Direct numerical integration at t=100 days (zonal average): thick solid line. MinEF-$\mathcal{E}$ with two edges: dotted line. Maximum entropy prediction: dashed line. MinEF-$\mathcal{M}$ with one edge: dash-dotted line. Experiment 8.

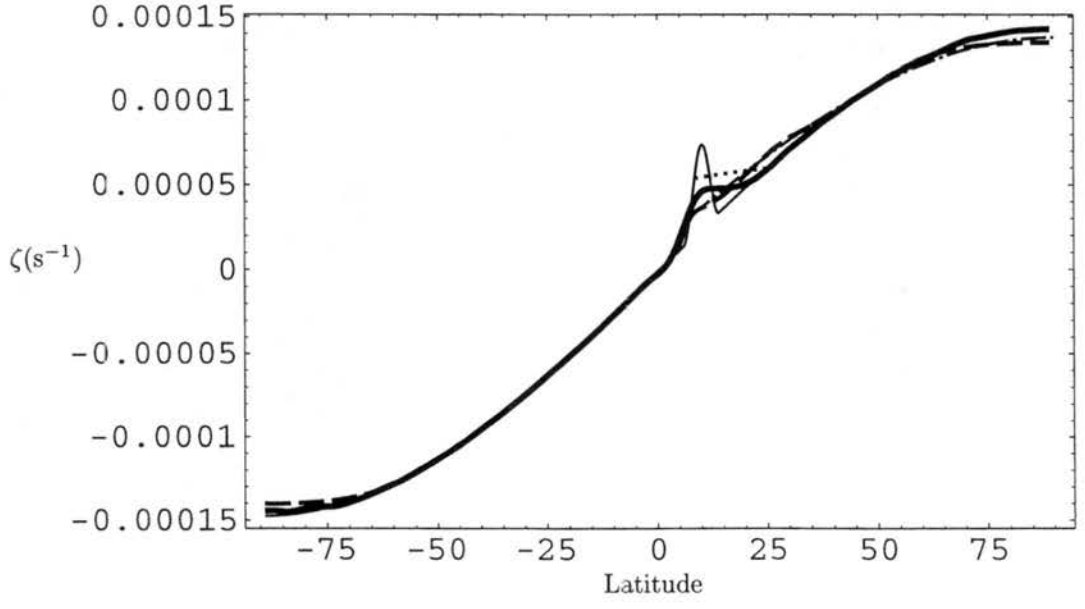

Figure 6.14: Same than Fig. 6.13 but for absolute vorticity profiles. Experiment 8.

Chapter 7

TWO-DIMENSIONAL TURBULENCE ON THE SPHERE

7.1 Introduction

Two-dimensional turbulence is usually understood as the study of high-Reynolds-number solutions of the incompressible Navier-Stokes equations which depend only on two coordinates, for spherical geometry, longitude (λ) and latitute (ϕ). For large-scale and planetary-scale atmospheric motions, the large ratio of horizontal to vertical scale in the atmosphere is an argument to consider such flows as quasi-two-dimensional.

Two-dimensional turbulence has a tendency for a transfer of energy towards larger scales, while enstrophy tends to be transfer towards smaller scales. Merilees and Warn (1975) showed that for interactions among three wave components of a flow on the sphere, the majority of interactions (in a statistical sense) are such that more energy flows to larger scales while more enstrophy flows to smaller scales.

Boer and Shepherd (1983) analyzed meteorological observations in a manner consistent with two-dimensional theory in order to clarify the degree to which large-scale atmospheric turbulence resembles that of two-dimensional turbulence theory. They obtained spectra of kinetic energy, enstrophy and available potential energy for both stationary and transient parts of the flow, finding two different flow regimes in wavenumber space. The high-wavenumber regime is dominated by the transient component of the flow, approximately exhibits several of the conditions characterizing homogeneous

and isotropic turbulence (such as the approximate independence of the spherical harmonic expansion of the streamfunction amplitude $|\psi_n^m|^2$ on the zonal wavenumber m) and displays some of the features of the enstrophy-cascade inertial subrange (Kraichnan, 1967). The low-wavenumber regime is dominated by the stationary component of the flow, exhibits marked anisotropy and displays large changes between January and July.

Rhines (1975) showed that, in the presence of the the beta-effect, the two-dimensional turbulence inverse cascade produces a field of Rossby waves, and the turbulent migration of the dominant scale ceases at a wavenumber $k_\beta = (\beta/2U)^{1/2}$ dependent only on the root-mean-square particle speed (U) and β, the northward gradient of the Coriolis parameter. In Rhines' (1975) numerical simulations, the homogeneous cascade passes through a state of propagating waves with tendency towards a flow of alternating zonal jets which he suggested are almost perfectly steady. This wave-turbulence interaction and the blocking of the energy inverse cascade at k_β has been called the "Rhines effect". The effect helps explain why the energy-containing eddies in the ocean and atmosphere fail to reach the size of their respective domains, and are much smaller. For typical ocean flows $k_\beta^{-1} = 70$ km, while for the atmosphere $k_\beta^{-1} = 1000$ km.

Williams (1978) used a numerical model of the spherical barotropic vorticity equation subjected to a stochastic representation of baroclinic processes, for conditions representing the planetary circulations of Jupiter and Earth. For the Jovian parameters, Williams' model solutions support the zonal symmetry and $L_\beta = \pi k_\beta^{-1}$ scale of the bands, producing zonally oriented flows composed of a series of alternating easterly and westerly jets, between which lie characteristic ovals. For the Earth regime, Williams numerical integrations formed westerly jets in the forced midlatitude zones, while Rossby wave propagation from those zones caused broad areas of easterly winds at low latitudes. Williams (1978) hypothesized that cascade blocking by a stronger surface drag prevents terrestrial flows from approaching the same degree of zonality as Jovian flows.

Vallis and Maltrud (1993) used scaling relationships and theoretical arguments to show that the inverse energy cascade of geostrophic turbulence is inhibited by a mean gradient of potential vorticity. Vallis and Maltrud predicted a dumbbell shape in spectral space (k_x, k_y) into which energy transfer is inhibited. This feature is produced both by two-point closure and by direct numerical

simulations on a beta plane, demonstrating that the transition wavenumber between waves and turbulence is anisotropic, and that the formation of zonal jets can be a direct consequence of the anisotropic turbulent inverse energy cascade.

A series of numerical simulations were performed by Cho and Polvani (1996) in freely evolving turbulence on a sphere. Their results show that the turbulent evolution is strongly dependent on numerical and physical conditions such as the dissipation, the initial spectrum, the rotation rate, and the Rossby deformation radius. In the nondivergent and nonrotating case, and initially turbulent flow evolves into a vorticity quadrupole at long times. This is a direct consequence of angular momentum conservation on the sphere, which forbids the flux of energy in or out of the $n = 1$ mode (see Tang and Orszag, 1978), thus forcing a pile-up at the $n = 2$ modes. In the presence of sufficiently strong rotation, the nondivergent long-time behaviour yields a field dominated by polar vortices, while in the case with a finite deformation radius (shallow-water model) the flow evolves toward a banded configuration, in which the number of bands increased with the rotation rate.

Nozawa and Yoden (1997) studied forced two-dimensional turbulence on a rotating sphere, finding three different flow regimes. In the case without rotation, a very large flow pattern, characterized by total wave number $n = 2$, was obtained due to the inverse energy cascade. With an increase in the rotation rate, a zonally banded structure consistent of alternating easterly and westerly jets becomes dominant; the width of the jets decreases and the number of jets increases as the rotation rate increases. The third flow regime was found when the forcing wavenumber is small and the rotation rate is large, and consists of a banded structure confined to high latitudes, yielding a circumpolar vortex with a strong easterly jet and a wavy structure in middle and low latitudes.

Using a global barotropic model, Huang and Robinson (1998) investigated the dynamics of two-dimensional turbulence on a rotating sphere. From the spectral form of the barotropic vorticity equation on the sphere, Huang and Robinson derived an expression for the anisotropic Rhines scale, which was compared and verified with decaying turbulence simulations. The "Rhines barrier" separates the regions where wave propagation dominates, from the regions where turbulent behaviour is dominant; due to the anisotropic nature of the Rossby waves, the Rhines barrier is displaced toward small total wavenumber n with decreasing zonal wavenumber m, having the consequence that the

inverse energy cascade in purely zonal modes is not affected by beta.

Huang and Robinson (1998) used a forced dissipative model with high wavenumber forcing to study the dynamics of persistent zonal jets, which form in relatively strong rotation cases (i.e., r.m.s. $U << a\Omega$). They concluded that the jet scale decreases with decreasing energy under a fixed rotation rate, the equilibrated jets generally stay at fixed latitudes, and that the zonal bands are nearly uniformly distributed in latitude, except that bands in high latitudes tend to be wider and weaker, due to the decrease of beta with latitude. The adjustment of the zonal jets to their equilibrium configuration can take a very long time, as they showed in their Fig. 5, where there is an early stage with six easterly jets that lasts for almost 1000 days before changing into a four-easterly jet configuration. Also, they pointed out the possibility that for some cases, depending of the energy level, the long term variability of the flow might vacillate between an n-jet configuration and an (n+1)-jet configuration.

This chapter will be dedicated to verification of the predictions given by the maximum entropy theory for an initial condition which represents several barotropically unstable jets, on both rotating and nonrotating spheres. The main difference with the previous experiments is that we will considerer full two-dimensional maximum entropy predictions, that is, maximum entropy solutions which depend in both longitude (λ) and latitude (ϕ).

There are two questions that we will try to answer with these experiments: 1) Is maximum entropy theory able to produce a quadrupole as an end-state for the nonrotating case? 2) For the case with rotation, are the alternating zonal jets a maximum entropy state for atmospheric flows?

7.2 Angular Momentum Conservation

The area-integrated angular momentum of a two-dimensional flow on a rotating sphere is a three-dimensional vector, which can be defined (Appendix C) with respect to an inertial reference frame (x, y, z), with origin at the center of the sphere, and where, at $t = 0$, the x-axis coincides with $(\lambda, \phi) = (0, 0)$ and the y-axis coincides with $(\lambda, \phi) = (\frac{\pi}{2}, 0)$. The sphere rotates around the z axis with rate Ω. In Appendix C we have derived the angular momentum conservation law for this

system, given by

$$\frac{d\vec{M}}{dt} = 0, \tag{7.1}$$

where $\vec{M}$ is the area integrated angular momentum of the two-dimensional flow plus the angular momentum due to the rotation of the sphere. Therefore, each component of $\vec{M}$ remains constant over time:

$$M_x = \int_{-\frac{\pi}{2}}^{\frac{\pi}{2}} \int_0^{2\pi} -a[u + \Omega a \cos\phi] \sin\phi \cos(\lambda + \Omega t) + av \sin(\lambda + \Omega t) d\lambda \cos\phi d\phi = M_x(t=0), \tag{7.2a}$$

$$M_y = \int_{-\frac{\pi}{2}}^{\frac{\pi}{2}} \int_0^{2\pi} -a[u + \Omega a \cos\phi] \sin\phi \sin(\lambda + \Omega t) - av \cos(\lambda + \Omega t) d\lambda \cos\phi d\phi = M_y(t=0), \tag{7.2b}$$

$$M_z = \int_{-\frac{\pi}{2}}^{\frac{\pi}{2}} \int_0^{2\pi} a[u + \Omega a \cos\phi] \cos\phi d\lambda \cos\phi d\phi = M_z(t=0). \tag{7.2c}$$

An alternative representation of the $\vec{M}$-components can be written in terms of the relative vorticity ζ_r:

$$M_x = \int_{-\frac{\pi}{2}}^{\frac{\pi}{2}} \int_0^{2\pi} a^2 \zeta_r \cos\lambda \cos\phi d\lambda \cos\phi d\phi \cos\Omega t - \int_{-\frac{\pi}{2}}^{\frac{\pi}{2}} \int_0^{2\pi} a^2 \zeta_r \sin\lambda \cos\phi d\lambda \cos\phi d\phi \sin\Omega t, \tag{7.3a}$$

$$M_y = \int_{-\frac{\pi}{2}}^{\frac{\pi}{2}} \int_0^{2\pi} a^2 \zeta_r \sin\lambda \cos\phi d\lambda \cos\phi d\phi \cos\Omega t + \int_{-\frac{\pi}{2}}^{\frac{\pi}{2}} \int_0^{2\pi} a^2 \zeta_r \cos\lambda \cos\phi d\lambda \cos\phi d\phi \sin\Omega t, \tag{7.3b}$$

$$M_z = \int_{-\frac{\pi}{2}}^{\frac{\pi}{2}} \int_0^{2\pi} a^2 \zeta_r \sin\phi d\lambda \cos\phi d\phi. \tag{7.3c}$$

In order to eliminate the explicit dependence of M_x and M_y on time, we combine them as $M_x^2 + M_y^2$ to get

$$\left[\int_{-\frac{\pi}{2}}^{\frac{\pi}{2}} \int_0^{2\pi} a^2 \zeta_r \sin\lambda \cos\phi d\lambda \cos\phi d\phi\right]^2 + \left[\int_{-\frac{\pi}{2}}^{\frac{\pi}{2}} \int_0^{2\pi} a^2 \zeta_r \cos\lambda \cos\phi d\lambda \cos\phi d\phi\right]^2 = \text{constant}^2, \tag{7.4}$$

meaning that, from the point of view of our rotating reference frame (λ, ϕ), the total angular momentum component on the $\phi = 0$ plane has a constant magnitude, while its direction rotates with frequency Ω.

In the case without rotation ($\vec{\Omega} \equiv 0$) we can express the conservation of the angular momentum in component form as

$$M_x = \int_{-\frac{\pi}{2}}^{\frac{\pi}{2}} \int_0^{2\pi} a^2 \zeta \cos\lambda \cos\phi d\lambda \cos\phi d\phi = \int_{-\frac{\pi}{2}}^{\frac{\pi}{2}} \int_0^{2\pi} a^2 \zeta_0 \cos\lambda \cos\phi d\lambda \cos\phi d\phi, \tag{7.5a}$$

$$M_y = \int_{-\frac{\pi}{2}}^{\frac{\pi}{2}} \int_0^{2\pi} a^2 \zeta \sin\lambda \cos\phi d\lambda \cos\phi d\phi = \int_{-\frac{\pi}{2}}^{\frac{\pi}{2}} \int_0^{2\pi} a^2 \zeta_0 \sin\lambda \cos\phi d\lambda \cos\phi d\phi, \tag{7.5b}$$

$$M_z = \int_{-\frac{\pi}{2}}^{\frac{\pi}{2}} \int_0^{2\pi} a^2 \zeta \sin\phi d\lambda \cos\phi d\phi = \int_{-\frac{\pi}{2}}^{\frac{\pi}{2}} \int_0^{2\pi} a^2 \zeta_0 \sin\phi d\lambda \cos\phi d\phi, \tag{7.5c}$$

where ζ_0 is the vorticity at $t = 0$.

We should note that equations (7.5) represent the real and imaginary parts of the vorticity field for the total wavenumber $n = 1$, and they are constant over time. This is consistent with the Tang and Orszag (1978), and Cho and Polvani (1996) argument that angular momentum conservation on the sphere forbids the flux of energy to or from of the $n = 1$ mode.

7.3 Maximum Entropy numerical method

7.3.1 Case 1: $\Omega \neq 0$

Since the (λ, ϕ) reference frame is rotating with respect to an inertial reference frame, we should note that any rotation with respect to λ of the maximum entropy solution is a maximum entropy flow too.

In order to incorporate the new angular momentum constraints to the numerical method described in section 3.3, and using the same notation, we write (7.4) as

$$\int_{-1}^{1} \int_0^{2\pi} (1-\mu^2)^{\frac{1}{2}} \left(\sum_{\ell=1}^{L} \hat{\zeta}_\ell \rho_\ell \right) \cos\lambda d\lambda d\mu =$$

$$\left[\left(\int_{-1}^{1} \int_0^{2\pi} (1-\mu^2)^{\frac{1}{2}} \zeta_0 \cos\lambda d\lambda d\mu \right)^2 + \left(\int_{-1}^{1} \int_0^{2\pi} (1-\mu^2)^{\frac{1}{2}} \zeta_0 \sin\lambda d\lambda d\mu \right)^2 \right]^{\frac{1}{2}}, \tag{7.6a}$$

with

$$\int_{-1}^{1} \int_0^{2\pi} (1-\mu^2)^{\frac{1}{2}} \left(\sum_{\ell=1}^{L} \hat{\zeta}_\ell \rho_\ell \right) \sin\lambda d\lambda d\mu = 0. \tag{7.6b}$$

Then we have two additional constraints to incorporate in the variational analysis of equations (3.12), with two new Lagrange multipliers ϵ_1, ϵ_2. The resulting expressions for the density functions ρ_ℓ, the partition function Z, and the macroscopic absolute vorticity ζ, that replace (3.14)–(3.16) are

$$\rho_\ell(\lambda, \mu) = \frac{1}{Z} \exp[\alpha_\ell + \hat{\zeta}_\ell(\beta\psi + \gamma\mu + \epsilon_1(1-\mu^2)^{\frac{1}{2}} \cos\lambda + \epsilon_2(1-\mu^2)^{\frac{1}{2}} \sin\lambda)], \tag{7.7}$$

$$Z = \sum_{\ell=1}^{L} \exp[\alpha_\ell + \hat{\zeta}_\ell(\beta\psi + \gamma\mu + \epsilon_1(1-\mu^2)^{\frac{1}{2}} \cos\lambda + \epsilon_2(1-\mu^2)^{\frac{1}{2}} \sin\lambda)], \tag{7.8}$$

$$\zeta = \frac{1}{Z}\sum_{\ell=1}^{L} \hat{\zeta}_\ell \exp[\alpha_\ell + \hat{\zeta}_\ell(\beta\psi + \gamma\mu + \epsilon_1(1-\mu^2)^{\frac{1}{2}}\cos\lambda + \epsilon_2(1-\mu^2)^{\frac{1}{2}}\sin\lambda)]. \tag{7.9}$$

The maximum entropy flow is that resulting from solving the nonlinear system of equations given by (3.9), (3.10), (3.11), (3.17), (7.6), (7.9) for $\alpha_\ell, \beta, \gamma, \epsilon_1, \epsilon_2, \zeta(\lambda,\mu), \psi(\lambda,\mu)$ given the initial flow. The iterative method used for this specific case is analogous to the one described by (3.18)–(3.25).

7.3.2 Case 2: $\Omega \equiv 0$

For the nonrotating case we write the conservation laws for the x and y angular momentum components as

$$\int_{-1}^{1}\int_{0}^{2\pi}(1-\mu^2)^{\frac{1}{2}}\left(\sum_{\ell=1}^{L}\hat{\zeta}_\ell\rho_\ell\right)\cos\lambda d\lambda d\mu = \int_{-1}^{1}\int_{0}^{2\pi}(1-\mu^2)^{\frac{1}{2}}\zeta_0\cos\lambda d\lambda d\mu, \tag{7.10a}$$

$$\int_{-1}^{1}\int_{0}^{2\pi}(1-\mu^2)^{\frac{1}{2}}\left(\sum_{\ell=1}^{L}\hat{\zeta}_\ell\rho_\ell\right)\sin\lambda d\lambda d\mu = \int_{-1}^{1}\int_{0}^{2\pi}(1-\mu^2)^{\frac{1}{2}}\zeta_0\sin\lambda d\lambda d\mu. \tag{7.10b}$$

We have again two additional constraints that are incorporated into the variational problem and iterative numerical method in the same way as described in section 7.3.1.

7.4 Experiments

The initial condition for the experiments of this chapter corresponds to a series of alternating westerly and easterly jets, with a maximum wind of the order of 20 ms^{-1}. Figure 7.1 shows the initial wind profile which consists of 5 westerly jets with wind maxima at high latitudes (around $75^o N, S$), the subtropics (around $37^o N, S$) and the Equator, and 4 easterly jets with wind maxima at middle latitudes (around $55^o N, S$) and the tropics (around $18^o N, S$). The initial relative vorticity profile is given by a sine function of latitude:

$$\zeta_r(\lambda,\phi) = 3\times 10^{-5}\text{s}^{-1}\sin(10\phi), \tag{7.11}$$

plotted in Fig. 7.2.

7.4.1 Experiment 9

Experiment 9 is performed on a rotating sphere with the rotation rate equal to that of the Earth ($\Omega = 7.292 \times 10^{-5}\mathrm{s}^{-1}$); the initial absolute vorticity profile is

$$\zeta(\lambda, \phi) = 3 \times 10^{-5}\mathrm{s}^{-1} \sin(10\phi) + 2\Omega \sin\phi, \tag{7.12}$$

which has several reversals of the latitudinal absolute vorticity gradient, satisfying Kuo's (1949) necessary condition for barotropic instability. The same localized perturbation $\zeta_d(\lambda, \phi)$ of chapters 5 and 6 (equation 5.4) is added to (7.12). Then, during a time integration of this flow, we expect the emergence of an instability with rearrangement of the vorticity field towards a stable configuration.

Numerical integration of this initial condition is done using the nonlinear barotropic nondivergent model described in chapter 2, with a triangular truncation of $N = 170$, $\nu = 9 \times 10^{13}\mathrm{m}^4\mathrm{s}^{-1}$, and timestep of 600s. The value of the hyperdifussion coefficient ν corresponds to an e-folding time for the highest wavenumber $N = 170$ of $\tau_{170} = 6$ hours.

Figure 7.3 presents Northern Hemisphere polar stereographic plots of the absolute vorticity field at different times of the numerical integration. At $t = 0$ (Fig. 7.3a) contours of absolute vorticity are concentric with respect to the rotation axis of the sphere. Deformation of the absolute vorticity contours begins to become apparent at $t = 9$ days (not shown); thinning and breakdown of contours around 70^oN is observed at $t = 13$ days (not shown) with wavy contours at other latitudes.

At $t = 20$ days (Fig. 7.3b) folding and breaking of vorticity contours is present in the tropics ($0 - 30^oN$) and midlatitudes ($40 - 70^oN$) separated by a region of high absolute vorticity gradient which has a wavenumber 6 shape and is located at about 40°N. A wavenumber 3 feature is observed at high latitudes, and the zero line has a wavenumber 7 structure close to the Equator.

Quite turbulent behaviour of the flow is observed between $t = 20$ days and $t = 70$ days, an example of which is shown if Fig. 7.3c. During the animation it is possible to detect strong mixing in the tropics and at high latitudes, but these two regions appear to remain discernibly separated by a ring of high absolute vorticity gradient located between 30°N and 40°N. In simulations where the relative vorticity field is plotted, extrusions of the ring of high absolute vorticity gradient (like the one at the lower-left side of Fig. 7.3b) break the relative vorticity contours, momentarily joining

same-sign relative vorticity regions.

During the rest of the simulation ($t = 70 - 150$ days), axisymmetrization of the flow takes place with smoothing and rearrangement of vorticity contours. A small scale vortex appears at high latitudes ($60 - 70^o N$) around day 40, merging with smaller scale vortices but preserving its identity until the end of the simulation at $t = 150$ days (Fig. 7.3d). The kinetic energy of the flow has a decay of 1.75% during the 150 days of the numerical integration, while the absolute enstrophy decays 2.43% (see Fig. 7.4).

We solved the 2-D maximum entropy method of section 7.3.1 with a total of $L = 10$ vorticity levels, a domain resolution of $T42$, and with the same energy, circulation and angular momentum of the initial condition for the numerical integration. A comparison of the flow at $t = 150$ days and a maximum entropy prediction in two dimensions is presented in Fig. 7.5, where the relative vorticity field is plotted for the Northern and Southern Hemispheres. In all plots of Fig. 7.5 we can see a series of structures with closed relative vorticity contours; the most significant difference is the magnitude of the relative vorticity maximum amplitude, which is $4 \times 10^{-5} s^{-1}$ for the direct numerical integration in contrast with $2 \times 10^{-5} s^{-1}$ for the maximum entropy prediction.

Plotting the relative vorticity field for the direct numerical integration with a contour interval of $2 \times 10^{-5} s^{-1}$ (Fig. 7.6a,b) allows us to have a better view of the structures that are commom with the maximum entropy prediction (Fig. 7.6c,d). In both cases there are alternating zones of positive and negative relative vorticity, which enclose large scale zonally-elongated vortices. A wavenumber 3-4 pattern is present at low and middle latitudes of Fig. 7.6a,b, contrasting with the wavenumber 2 pattern of Fig 7.6c,d. The polar regions have negative relative vorticity for the Northern Hemisphere, and positive relative vorticity for the Southern Hemisphere in both cases, meaning that the relative vorticity present at the poles in the initial condition (Fig. 7.2) has moved equatorward.

The maximum entropy prediction has regions of negative relative vorticity joined together at about $60^o N$ and $25^o S$. The direct numerical integration at $t = 150$ days does not reveal those features, however, during the first 100 days of time integration; momentary (1-2 days) attaching of same sign relative vorticity regions was observed several times.

The solution obtained from the maximum entropy prediction was used as an initial condition for

the numerical model of chapter 2 in order to observe its behaviour in time. The whole pattern has a westward solid body rotation with a period of the order of 3 days. A longer periodic behaviour was also observed, the negative relative vorticity regions that are in contact at $60^o N$ and $25^o S$ separate, move accross and reattach again, all with a period of approximately 60 days.

The one-dimensional maximum entropy model of chapter 3 with maximum total wavenumber $N = 127$ and 60 vorticity levels, was also run for experiment 9.

Results for the longitude-independent maximum entropy method, the zonal average of the two-dimensional maximum entropy solution, the zonal average of the direct numerical integration at $t = 150$ days and the initial condition are shown if Fig. 7.7 for the zonal wind, and Fig. 7.8 for the absolute vorticity.

In Fig. 7.7 we observe that the high-latitude $(65 - 90^o N, S)$ westerly jets of the initial condition dissappear in the time integration and the maximum entropy predictions, while the middle and low-latitude alternating jets are preserved. The most significant difference is at high latitudes (poleward of 50^o) where the direct numerical integration line is between of the two maximum entropy predictions.

Figure 7.8 shows that the absolute vorticity profiles resulting from the maximum entropy models and the direct numerical integration remove the reversals in the latitudinal gradient of the absolute vorticity, except the 1D maximum entropy at high latitudes, where the line of the direct numerical integration model is between of the two maximum entropy predictions.

Note that the zonally averaged profiles of the 2-D maximum entropy prediction and the time integration model have lower energy that the initial condition since the meridional part of the flow is not taken into account. In addition cancellations may occur at latitudes where easterly and westerly winds coexist, while the 1-D maximum entropy profile has all the energy of the initial state in the zonal flow.

A second 2-D maximum entropy solution for this experiment was found. It has an absolute vorticity profile without appreciable difference from the first 2-D solution, but the relative vorticity field shows a different type of wavenumber distribution in the midlatitude structures and the flow is more zonal in the tropical regions (Fig. 7.9). The entropy difference between the two solutions

is only 0.001%. The profile of the zonal wind for both of the two-dimensional maximum entropy solutions is shown in Fig. 7.10; the second solution has a stronger westerly flow at the equator, but weaker westerly jets at midlatitudes, with a difference of approximately 1ms^{-1}.

7.4.2 Experiment 10

For this experiment we have used the same relative vorticity condition (equation 7.11) as in experiment 9; the difference is that the flow in on a non-rotating sphere ($\Omega \equiv 0$), so that the relative vorticity field and the absolute vorticity field are the same. The disturbance $\zeta_d(\lambda, \phi)$ given by (5.4) is added to (7.11), so that the initial flow is given by

$$\zeta(\lambda, \phi) = 3 \times 10^{-5}\text{s}^{-1} \sin(10\phi) + \zeta_d(\lambda, \phi). \tag{7.13}$$

A 200 day direct numerical integration of the initial flow (7.13) is performed using the nondivergent barotropic model of chapter 2, with triangular truncation $T170$, a timestep of 600s and a hyperdiffusion coefficient $\nu = 9 \times 10^{13}\text{m}^4\text{s}^{-1}$, which corresponds to a damping time of the highest total wavenumber $N = 170$ of $\tau_{170} = 6$ hours.

Figure 7.11 presents Northern Hemisphere polar stereographic plots of the vorticity field at different times. At $t = 0$ (Fig. 7.11*a*) the flow consists of concentric regions of alternating positive and negative (dashed) vorticity.

After 6 days of evolution, the vorticity contours show some distortion from zonal symmetry, and at $t = 10$ days (Fig. 7.11b) a wavy pattern is evident in the vorticity field, which is followed by irreversible elongation and breakdown of contours at $t = 13$ days. By $t = 15$ days turbulent behaviour is present over the whole domain, making it difficult to follow particular features of the flow; examples of this turbulent behaviour are shown in Fig. 7.11c,d. At $t = 35$ days (not shown) there are a few vortices that have emerged, but the flow still contains a lot of small scale filamentary features.

Figure 7.11e shows the state of the flow at $t = 40$ days where it is possible to observe, especially in the positive vorticity regions, vortices with sizes up to 20^o latitude in diameter. These vortices have spontaneously emerged from the turbulence through merging of smaller scale features and shedding

of long, thin filaments. Such behaviour is typical of two-dimensional turbulence experiments (i.e. McWilliams, 1984).

During the simulation it is possible to follow interactions of same-sign vortices which end in partial or total merger, followed by symmetrization of the "victorious" vortex through the ejection of filaments, an example of which is seen in the lower part of Fig. 7.11f. A consequence of this merging behaviour is the reduction of the total number of vortices observed as time increases.

In Fig. 7.11g ($t = 80$ days) we see that a pair of positive-negative vortices has emerged, with a diameter of approximately 35^o latitude, surrounded by smaller scale features. At $t = 100$ days another large positive vortex that previously was in the Southern Hemisphere appears at low latitudes.

The simulation runs for a total of 200 days. During the invertval between 100 and 200 days it is possible to follow a total of four large vortices, two with positive vorticity, and two with negative vorticity. These vortices continue to absorb small scale features, but without any major interaction among them other than mutual translation, showing a tendency for an equilibrium state where the large vortices slowly move across homogeneous same-sign vorticity regions. The "quadrupole" that we have at the end of the 200 day direct numerical integration is consistent with the experiment that Cho and Polvani (1996) performed with their barotropic nondivergent vorticity model. During the 200 days of numerical simulation, the kinetic energy decayed 1.82%, while the enstrophy decayed 91.8% (see Fig. 7.12).

As mentioned in section 7.1, the inverse energy cascade is blocked at total wavenumber $n = 2$, forbidding the flux of energy towards the $n = 1$ mode. Knowing this, we have solved the maximum entropy problem in two dimensions with initial guesses that consist of pure total wavenumber 2 modes; the number of vorticity levels we used is $L = 10$, with a domain resolution of $T42$, and with the same energy, circulation and angular momentum vector of the initial condition. Figure 7.13 presents the three maximum entropy states obtained with their entropy value indicated.

Note that the flow given by the initial condition (7.13) has values of each of the angular momentum components that are close to zero (the alternating zonal jets cancel out most of the angular momentum in the $\vec{\Omega}$ direction, while the two other components are due just to the small initial perturbation $\zeta_d(\lambda, \phi)$), and since our initial guesses were pure total wavenumber 2 modes, the maximum

entropy states of Fig. 7.13 remain almost pure total wavenumber 2 modes.

The case $n = 2$, $m = 0$ has higher entropy than the other two, but with a relative difference that is of the order of 0.03%. This is an indication that each of the three end-states has a high probability to be an equilibrium state for a flow with the same macroscopic invariants and which has a turbulent evolution. We do not know a priori which of these three states is the one favored by the nonlinear flow evolution, but because they are almost orthogonal functions for the reasons described above, we could expect that the end-state of a turbulent evolution is a linear combination of those three maximum entropy flows. To test this idea we have taken the average of the three maximum entropy states shown in Fig. 7.13 and used it as a guess for the maximum entropy code with the same parameters described above.

Figure 7.14 presents the comparison of the state of the nonlinear flow evolution at $t = 200$ days, and the maximum entropy prediction obtained in the way just explained. The figures are polar stereographic plots of the Northern and Southern Hemispheres, note that the contour interval for Fig. 7.14a,b is $1 \times 10^{-5}\mathrm{s}^{-1}$, while for Fig 7.14c,d is $4 \times 10^{-6}\mathrm{s}^{-1}$.

The maximum entropy prediction has strong similarities with the direct numerical integration at $t = 200$ days. Maximum entropy theory predicts the correct number of vortices and approximately gives the correct orientation for the zero contour. But there are also some differences. The vortices of the time integration are smaller and have a higher (lower) vorticity maximum (minimum). At the end of the numerical integration the vortices are moving at a rate of 1.4 degrees of latitude per day, keeping the same orientation of the zero contour, but slowing their speed with time. When the solution given by maximum entropy theory was taken as the initial condition for the barotropic model, a slow movement of the vortices of the order of 0.1 degrees of latitude per day was detected.

7.5 Discussion

The results of this chapter indicate that the dynamics of a flow and its equilibrium state is strikingly different if the evolution occurs in a rotating or non-rotating sphere, even with the same initial values of the macroscopic invariants.

In section 7.1 we have argued that the turbulent migration of the dominant scale ceases at wavenumber $k_\beta = (\beta/2U)^{1/2}$, dependent only on the root-mean-square eddy velocity amplitude (U) and β, the northward gradient of the Coriolis parameter. An alternative view to this effect is given by the beta-Rossby number (see Möller and Montgomery, 1999)

$$R_\beta = \frac{U}{\beta L^2},$$

where L is the eddy scale. R_β represents the ratio of the nonlinear terms in the vorticity equation to the linear Rossby restoring term. When the sphere is rotating, the basic vorticity gradient tends to suppress the nonlinear advective terms (in regions not close to the poles), while at the limit of no rotation $R_\beta \to \infty$, and the dynamics is dominated by nonlinear processes.

We have seen that maximum entropy theory can give us more than one solution for a particular initial condition, raising the question of which solution the actual flow evolution will prefer. Another point of interest is that, if we have an equilibrium state that is changing with time (for example, having a translation or even having some change in structure which returns to a specific configuration after some time), then we could expect an infinite number of maximum entropy solutions depending on the initial guess we use.

Looking at the kind of macroscopic state that the maximum entropy theory gives us, we note that they do have a large degree of organization, while an equilibrium state obtained from a direct numerical integration is more or less disorganized.

Marcus (1990) studied the dynamics of vortices in a shearing zonal flow, performing a series of five experiments to find out if the final equilibrium state was a function only of the values of the conserved quantities, and whether the flow losses the memory of all of the other properties of its initial condition. His findings showed that each of the five flows evolved to form one large vortex, but the vortex's final radial location was not the same for all five flows and in each case was approximately equal to its initial value. Thus, these flows retained memory of their initial condition. However, Marcus (1990) found that for other flows where the evolution is less laminar and there is more mixing, the final flow depends only on the values of the conserved quantities and looses memory of the initial condition.

Some understanding for solving this kind of problem is illustrated in the non-rotating case explained above. We may need to look to the maximum entropy solutions that are orthogonal among them, and compare their actual values of entropy. Then the end state of flow evolution can be represented by a weighted average of those orthogonal maximum entropy solutions, with weights that are proportional to their entropy values, considering also which of the orthogonal maximum entropy solution is closer to the initial condition.

In the literature it is common to read that orographic effects are the main reason that mean atmospheric flows deviate from zonal symmetry. For the experiment on the rotating sphere explained in this chapter, we have seen that the nonlinear time integration and the two-dimensional maximum entropy prediction prefer equilibrium states that are not zonally symmetric, consisting of elongated vortices of different sizes, ranging from 1,000 to 3,000 km in meridional extent, and from 2,000 to 10,000 km in zonal extent. These solutions are obtained in a barotropic nondivergent model without any orographic forcing present, pointing out the need to quantify how much of the large-scale atmospheric mean flow is influenced by orographic effects and how much of it is due to the natural tendency of the flow towards a nonsymmetric equilibrium state.

Future tests of the two-dimensional maximum entropy theory are needed for more cases and under a wide variety of initial conditions in order to have a better view of the usefulness of the theory for real meteorological problems.

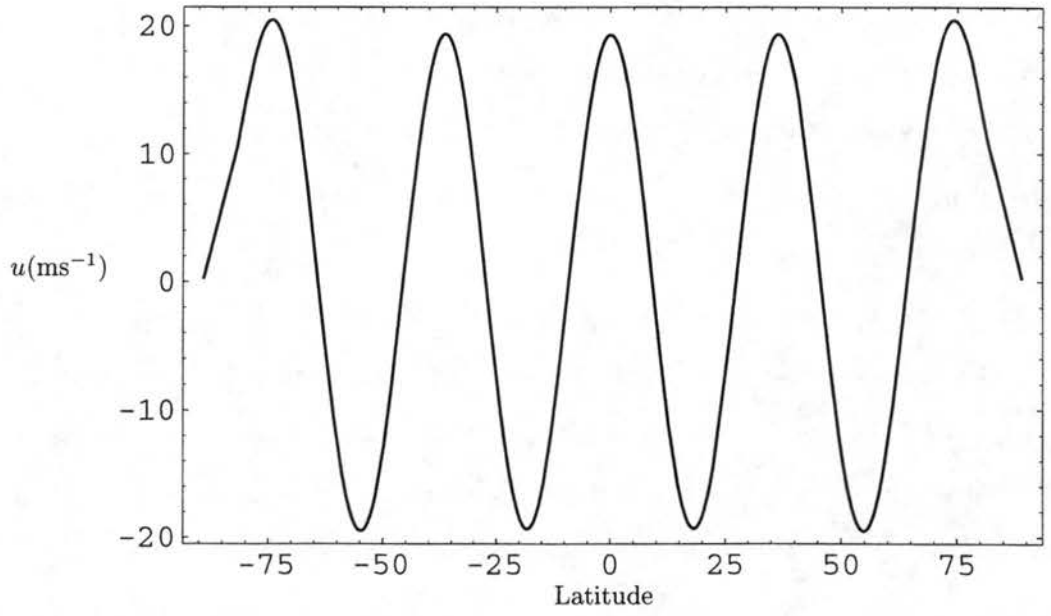

Figure 7.1: Initial zonal wind profile. Experiments 9 and 10.

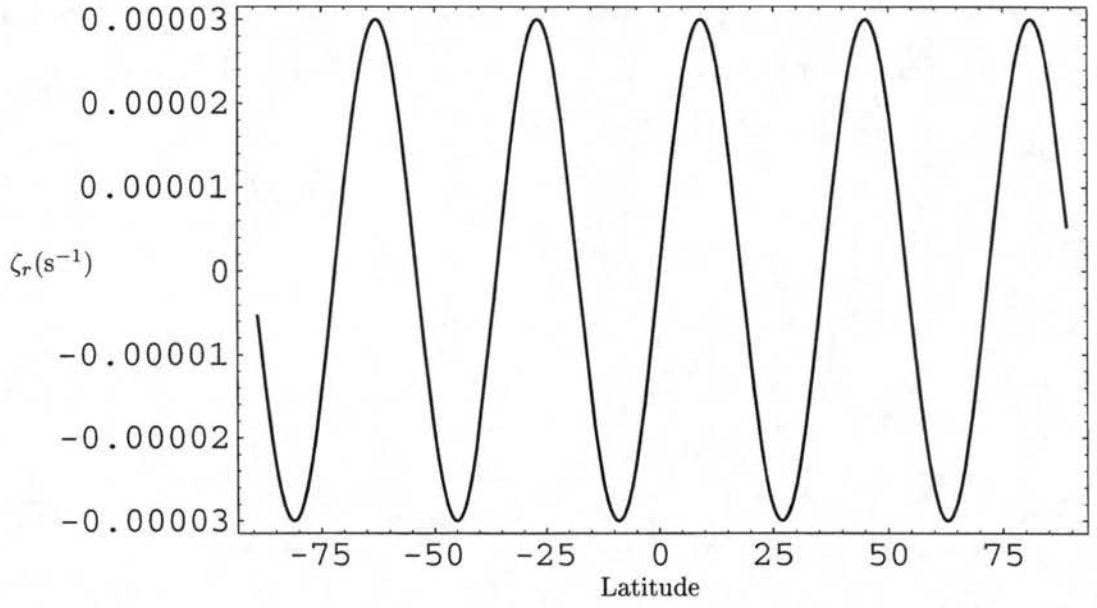

Figure 7.2: Initial relative vorticity profile. Experiments 9 and 10.

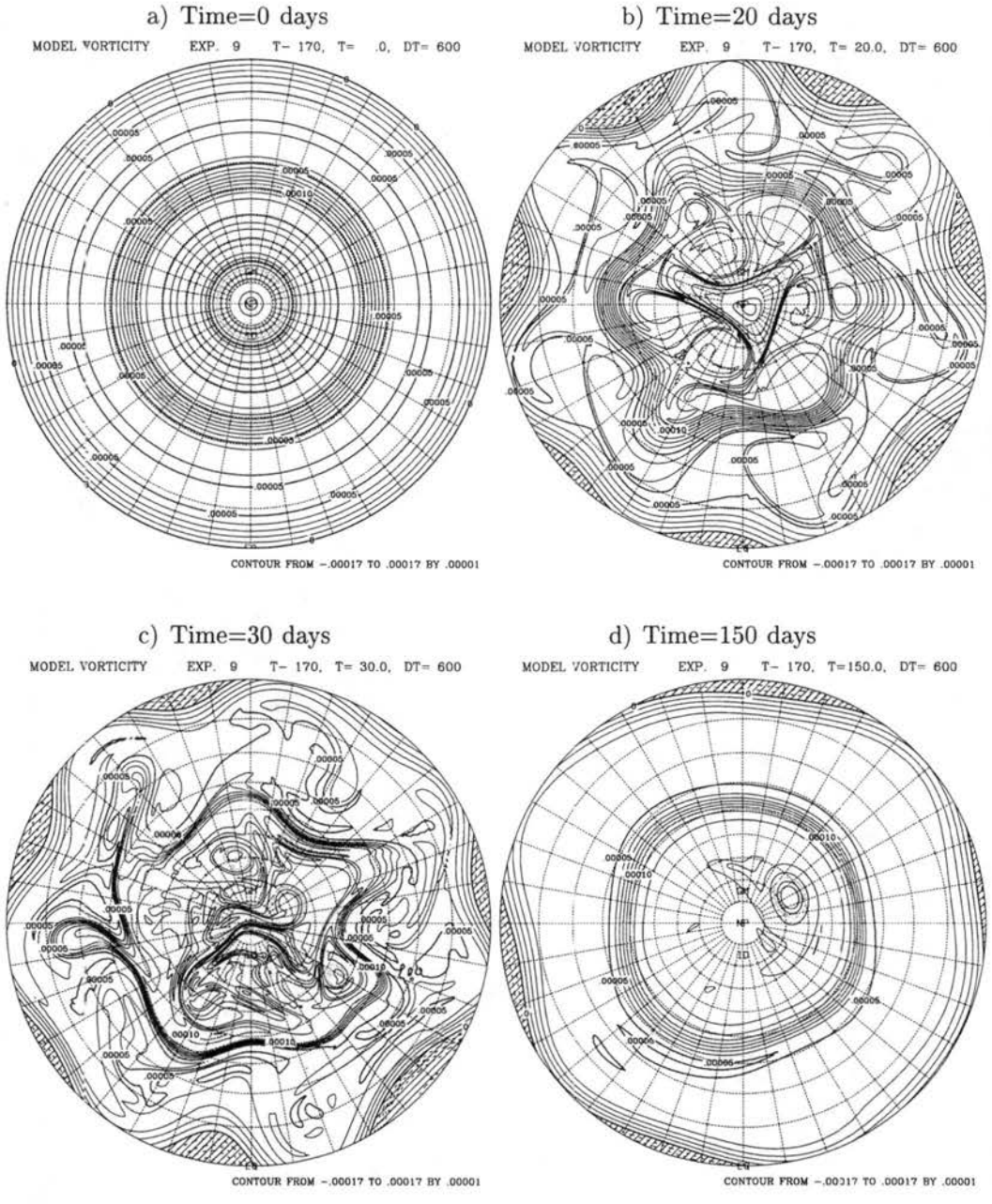

Figure 7.3: Northern Hemisphere polar stereographic plots of the absolute vorticity field (in s^{-1}) for selected snapshots of experiment number 9. Negative absolute vorticity regions are dashed.

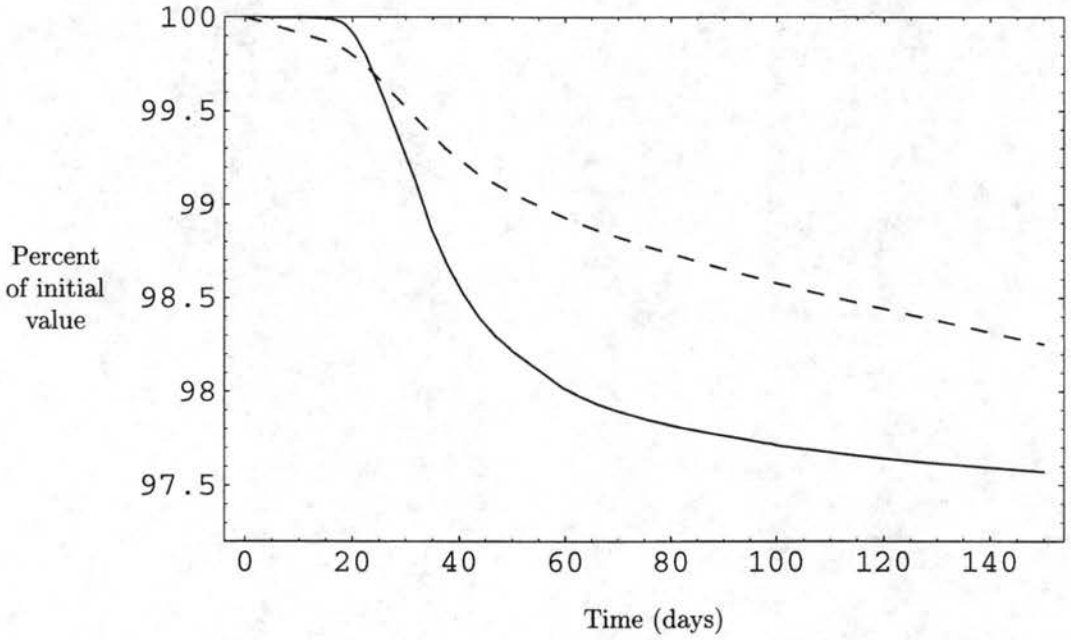

Figure 7.4: Time dependence of the kinetic energy (dashed line) and absolute enstrophy (continuous line) relative to their initial values for experiment 9.

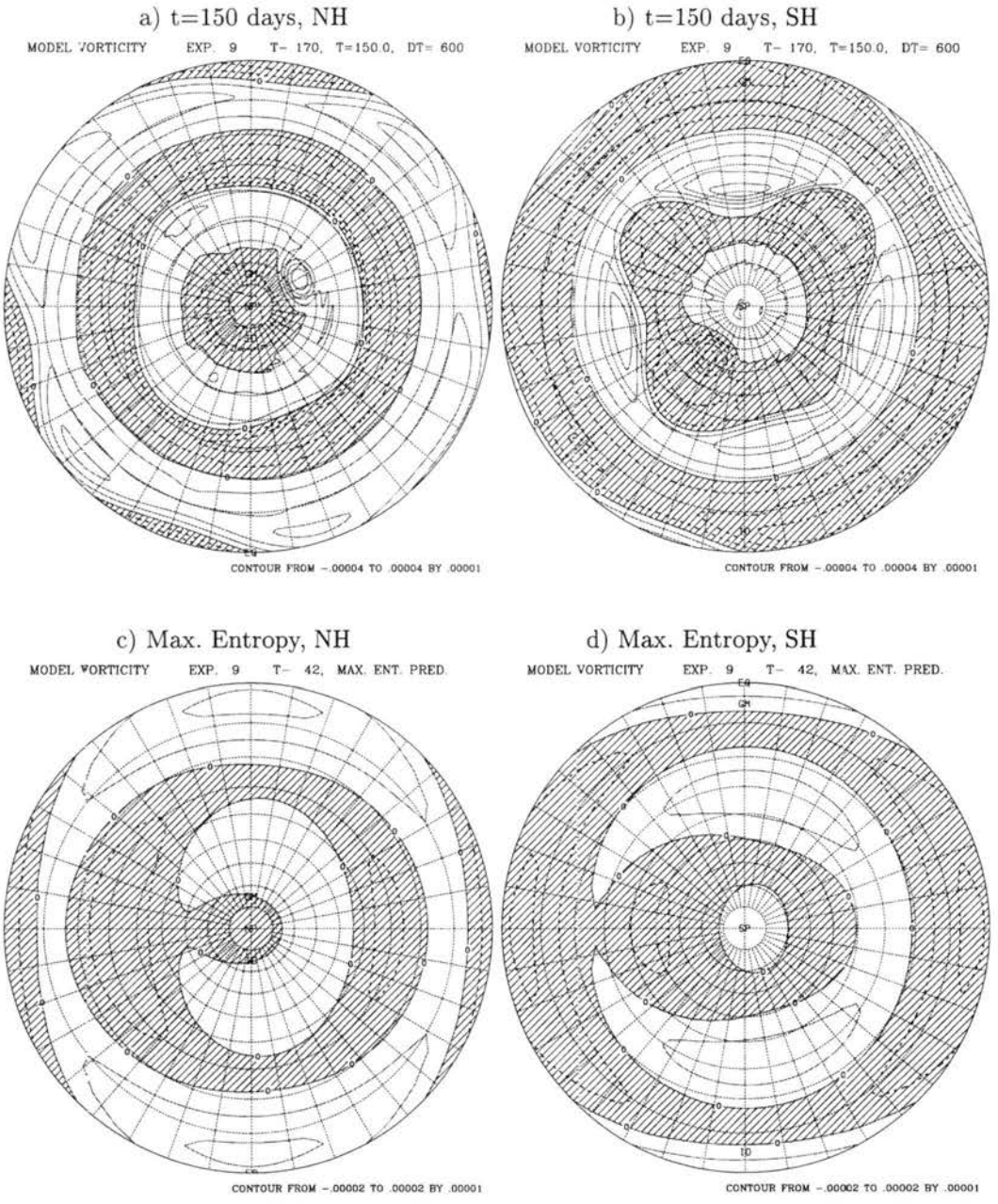

Figure 7.5: Relative vorticity field comparison between the direct numerical integration at $t = 150$ days for the Northern and Southern Hemispheres (a and b respectively) and the maximum entropy prediction for c) Northern Hemisphere and d) Southern Hemisphere. Negative relative vorticity regions are dashed, the units are s^{-1}. Experiment 9.

a) t=150 days, NH

b) t=150 days, SH

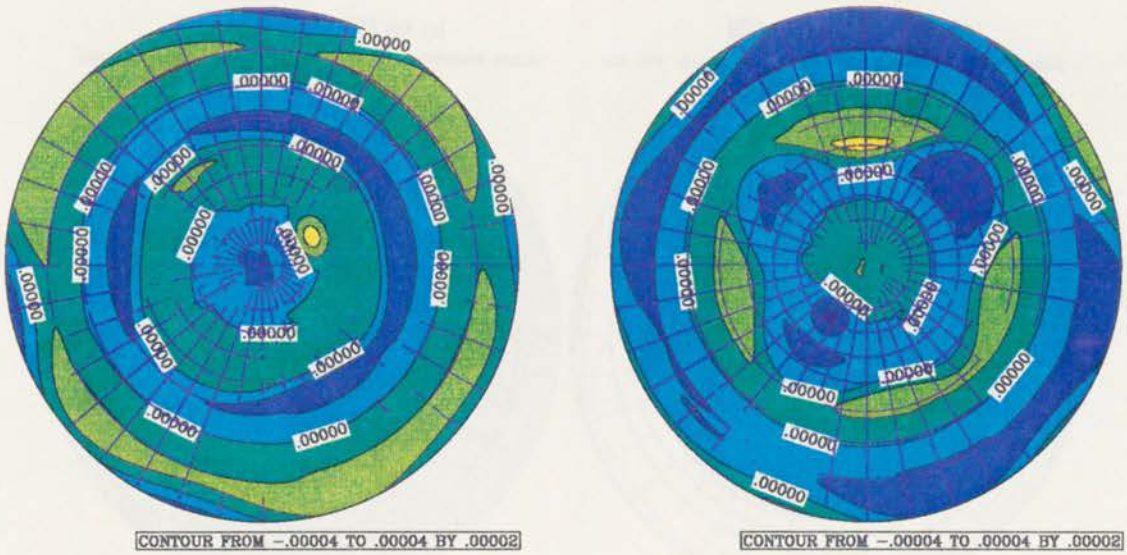

c) Max. Entropy, NH

d) Max. Entropy, SH

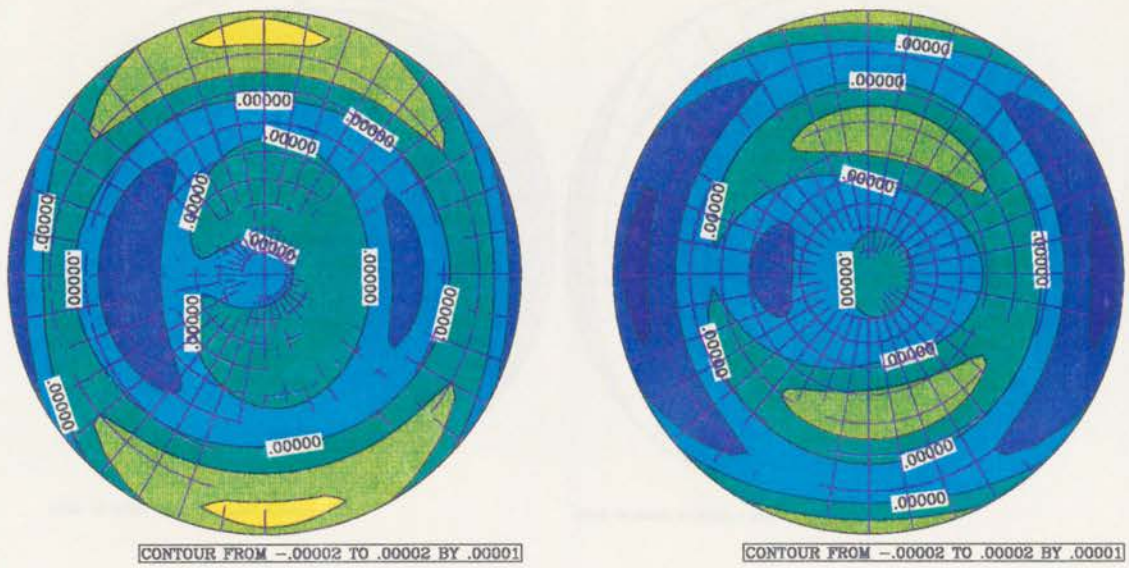

Figure 7.6: Same that Fig. 7.5 except that the contour interval for a) and b) is $2 \times 10^{-5}s^{-1}$ instead than $1 \times 10^{-5}s^{-1}$. Blue regions are negative; green and yellow regions are positive; the zero line is indicated. Experiment 9.

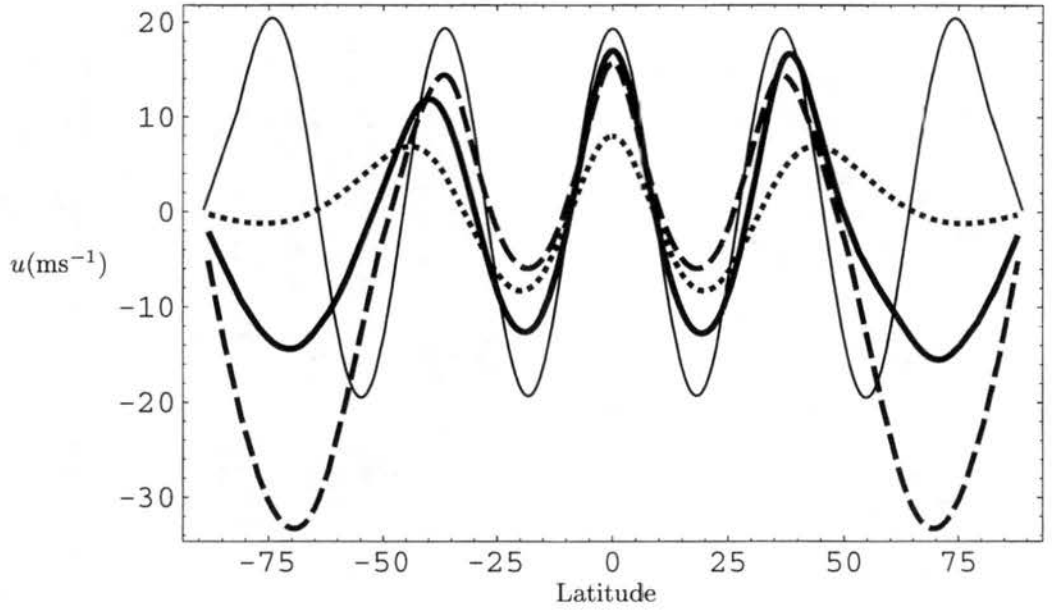

Figure 7.7: Zonal wind profiles. Initial condition: thin solid line. Zonal average of the direct numerical integration at t=150 days: thick solid line. Zonal average of the maximum entropy prediction in two dimensions: dotted line. Maximum entropy prediction in one dimension: dashed line. Experiment 9.

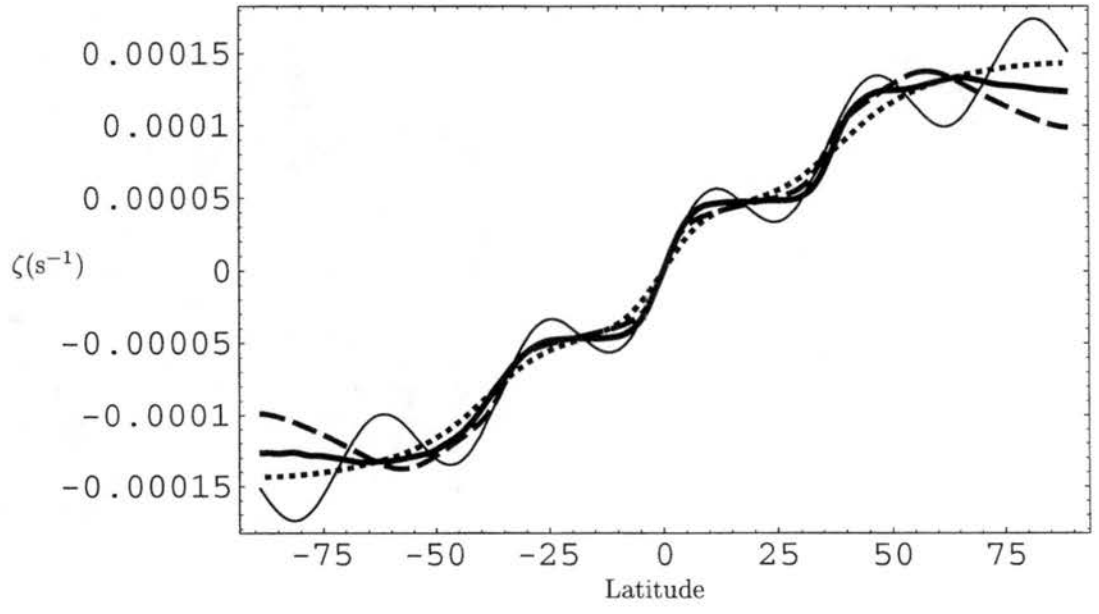

Figure 7.8: Same than Fig. 7.7 but for absolute vorticity profiles. Experiment 9.

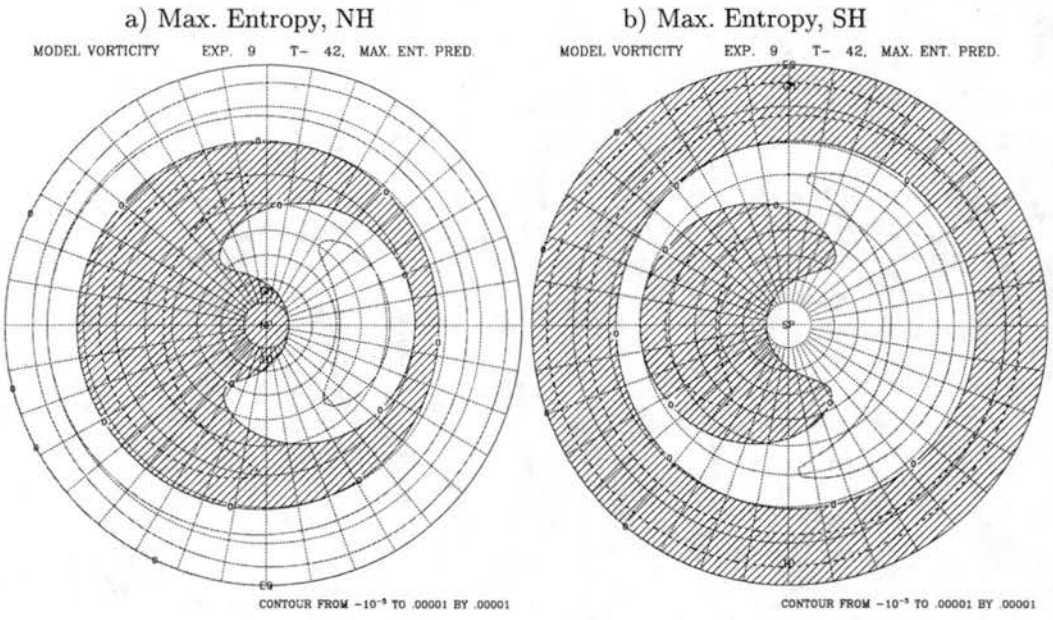

Figure 7.9: Relative vorticity field (in s^{-1}) for the second maximum entropy solution. a) Northern Hemisphere and b) Southern Hemisphere. Negative relative vorticity regions are dashed. Experiment 9.

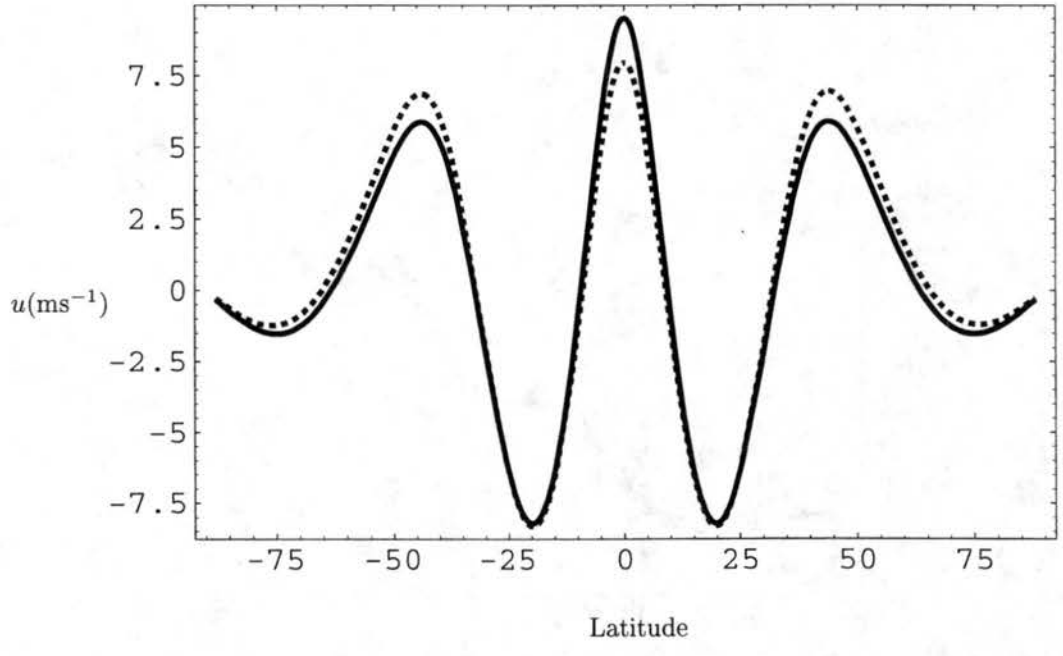

Figure 7.10: Zonal wind profiles. First maximum entropy solution (Fig. 7.5c,d): dotted line. Second maximum entropy solution (Fig. 7.9): solid line. Experiment 9.

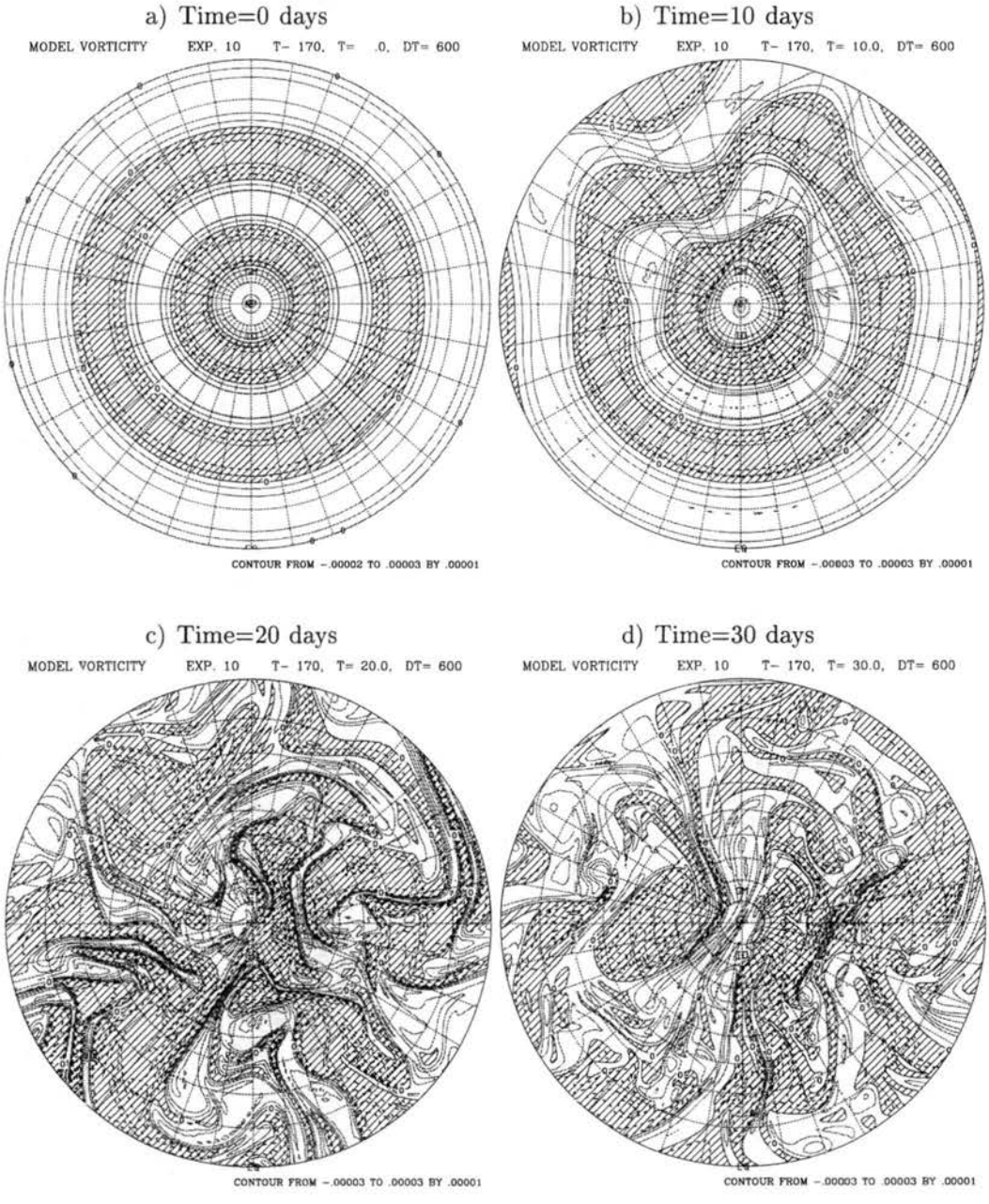

Figure 7.11: Northern Hemisphere polar stereographic plots of the vorticity field (in s^{-1}) for selected snapshots of experiment number 10. Negative vorticity regions are dashed.

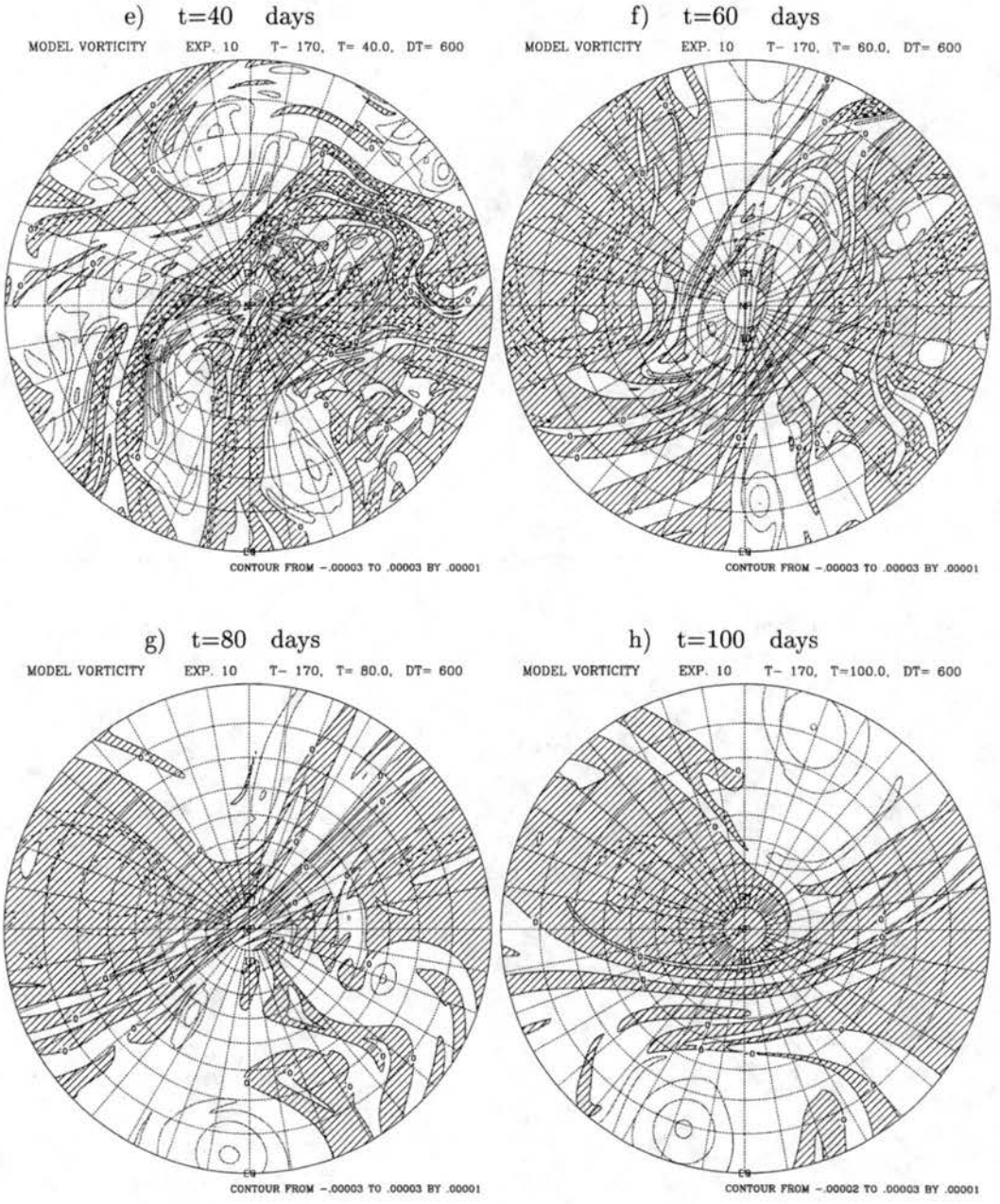

Figure 7.11: Continuation.

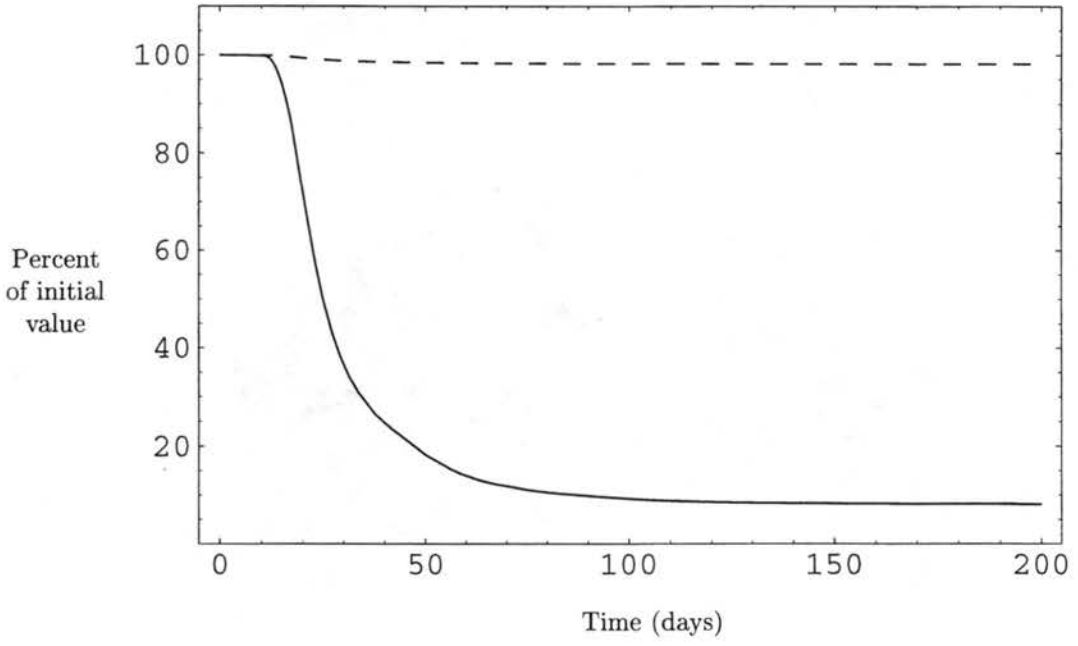

Figure 7.12: Time dependence of the kinetic energy (dashed line) and enstrophy (continuous line) relative to their initial values for experiment 10.

a) n=2, m=2. S = 27.2152

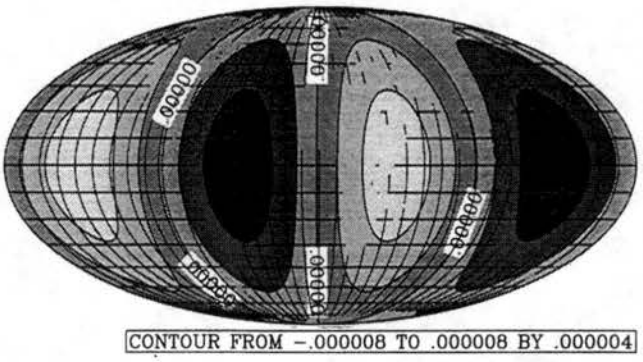

b) n=2, m=1. S=27.2161

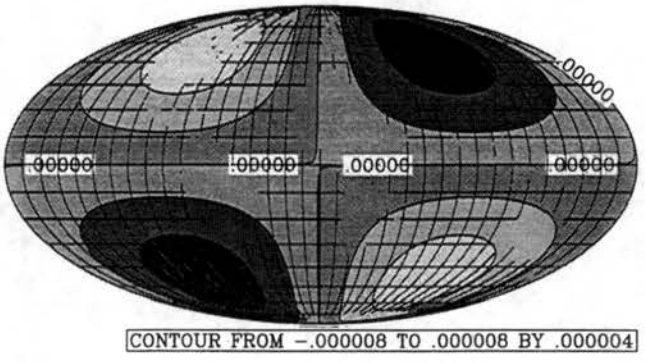

c) n=2, m=0. S=27.2234

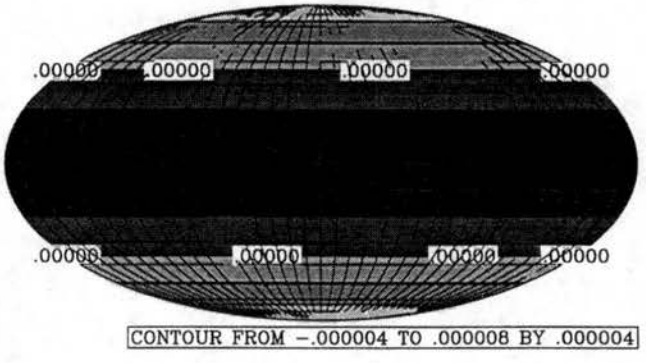

Figure 7.13: Maximun entropy predictions obtained for the vorticity field (in s^{-1}) from initial guesses with total wavenumber $n = 2$. The domain shown is the whole sphere in Mollweide projection. The zero line is indicated; the clearest region is positive and the darkest is negative. The entropy value (S) associated with each flow is indicated.

a) t=200 days, NH

b) t=200 days, SH

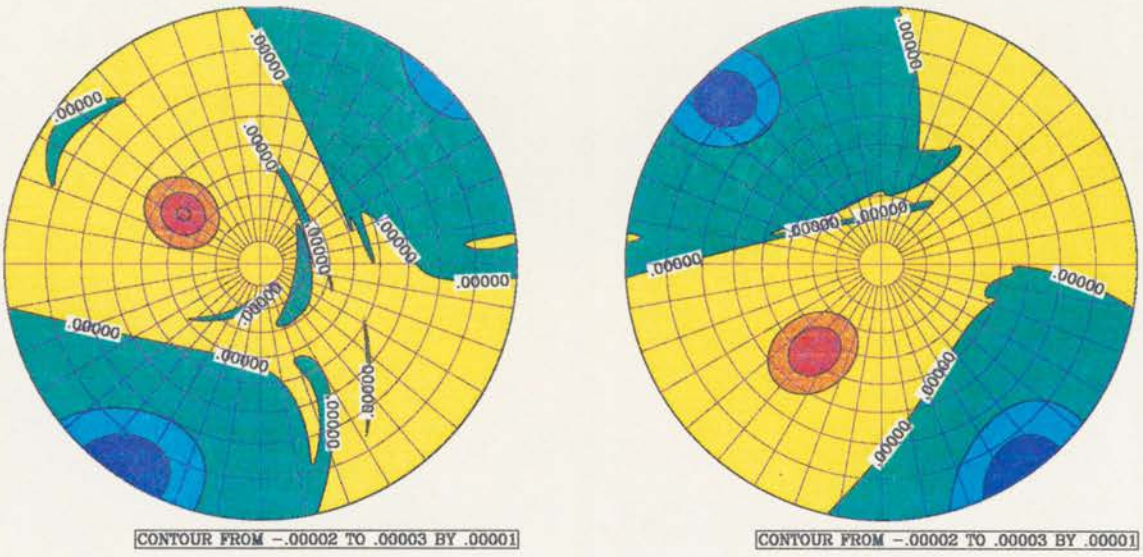

c) Max. Entropy, NH

d) Max. Entropy, SH

$S = 27.2158$

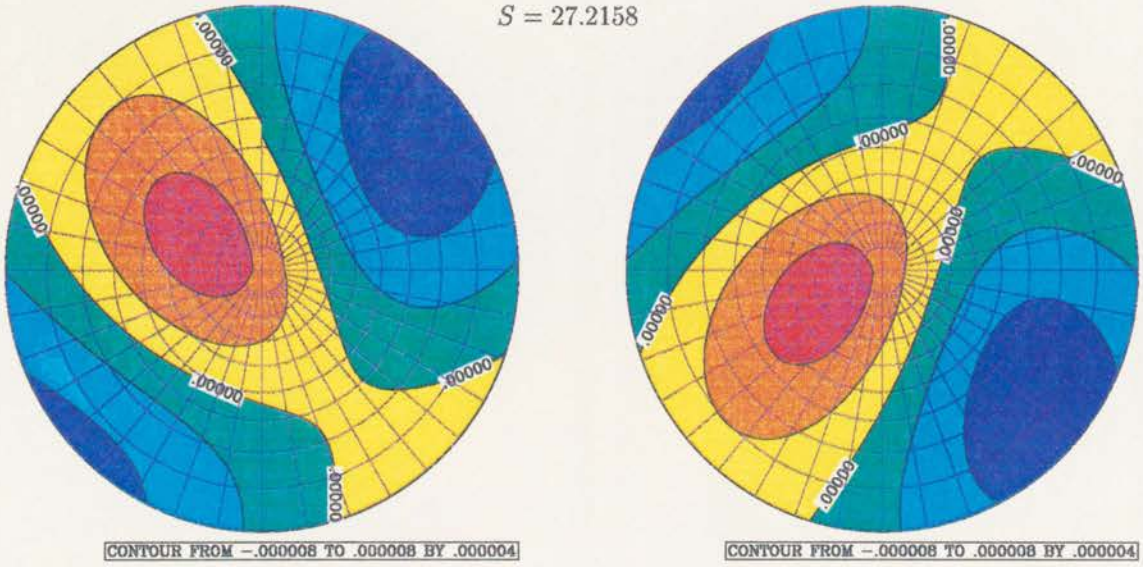

Figure 7.14: Vorticity field comparison between the direct numerical integration at $t = 200$ days for the Northern and Southern Hemispheres (a and b respectively), and the maximum entropy prediction for c Northern Hemisphere and d Southern Hemisphere. Note that the contour interval for a and b is $1 \times 10^{-5} s^{-1}$, and for c and d is $4 \times 10^{-6} s^{-1}$. Blue and green regions are negative; red and yellow regions are positive; the zero line is indicated. The entropy value (S) associated with the maximum entropy prediction is indicated. Experiment 10.

Chapter 8

SUMMARY AND CONCLUSIONS

Numerical simulations of barotropic flows (e.g., McWilliams 1984, Yoden and Yamada 1993, Polvani et al. 1994, Cho and Polvani 1996), as well as laboratory experiments (e.g., Van de Konijnenberg et al. 1998) have reported the emergence of isolated coherent vortices from initial turbulent conditions. Large scale coherent vortices are also present in the atmospheric circulation, for example the stratospheric polar vortex, midlatitude anticyclones, blocking action in the westerlies and, at a smaller scale, tropical cyclones.

The maximum entropy and minimum enstrophy theories are two different approaches that predict the final equilibrium state reached by a flow which evolves from an initial configuration, without following the intermediate states of the fluid.

The Miller-Robert version (Miller 1990, Robert 1991) of the maximum entropy theory uses the ideas of statistical mechanics and applies them to a discrete version of a continuous vorticity field. In this work we have extended the maximum entropy theory to flows that evolve on the surface of a sphere, expressing the coarse grained or "macroscopic" vorticity field as the sum of the initially defined vorticity levels $\hat{\zeta}_\ell$, times the probability $\rho_\ell(\lambda, \mu)$ of finding that vorticity level at a specific point (λ, μ) on the sphere. The problem is to find the expectation functions $\rho_\ell(\lambda, \mu)$ which maximize the Boltzmann mixing entropy, subject to the conservation laws of total kinetic energy, angular momentum and circulation. In mathematical form, the solution of the maximum entropy flow involves a nonlinear system of equations, which is solved using an iterative method proposed

by Turkington and Whitaker (1996), adapting it to spherical geometry.

Following the selective decay hypothesis (Matthaeus and Montgomery, 1980, Carnevale et al. 1991, 1992, Matthaeus et al. 1991) in which the equilibrium state of the flow is that with the minimal ratio of enstrophy to energy, we have developed a total of four different minimum enstrophy predictions with either constant zonal angular momentum (MinEF-$\mathcal{M}$) or constant kinetic energy (MinEF-$\mathcal{E}$) where mixing is confined to a polar cap (one edge), or to a latitude belt which excludes the poles (two edges). The technique applied was the calculus of variations with one constraint (energy or angular momentum), maximizing the enstrophy deficit.

For the MinEF-$\mathcal{M}$, the mathematical problem leads to equations for the zonal wind and absolute vorticity as a function of latitude, the southern edge of mixing (μ_s), and, for the case with two edges, the northern edge of mixing (μ_n); the solution is obtained by enforcing the condition that the zonal angular momentum of the flow is conserved. The MinEF-$\mathcal{E}$ problem involves finding the mixing edge μ_s and the Lagrange multiplier α (and the northern mixing edge μ_n for the two edge problem); these unknowns are obtained from consistency between the derived angular velocity and absolute vorticity profiles and the condition of constant kinetic energy.

A barotropic non-divergent numerical model on the sphere is used to study the evolution of ten different barotropically unstable initial conditions, four of them corresponding to a northern hemisphere stratospheric polar vortex, four to tropical shear layers, one to an alternating zonal jet configuration on a rotating sphere and one to the same zonal jet configuration on a non-rotating sphere.

Direct numerical integration of stratospheric polar vortex experiments showed instability, folding and breaking of absolute vorticity contours, mixing of vorticity in the initially barotropically unstable regions, and a tendency to a monotonic absolute vorticity profile, behaviour that is consistent with previous experiments reported by Ishioka and Yoden (1994). The predictions of maximum entropy theory compared well with the zonal average of the absolute vorticity and the zonal wind of the direct numerical integration after 100 days of evolution, showing also good predictive skill of the statistical distribution of air parcels traced during the numerical simulation. MinEF-$\mathcal{E}$ and MinEF-$\mathcal{M}$ showed

good predictive skill in the polar vortex experiments where mixing was confined to a polar cap, but was deficient in cases where mixing was global or was confined to a latitude belt; for the later case, the two-edge problem showed considerable improvement over the one-edge solution.

In order to study the dynamical behaviour and equilibrium state for flows that resemble conditions associated with the intertropical convergence zone (ITCZ), we used a zonally-symmetric vorticity field that produces a shear zone with westerlies on the south side of a local vorticity maximum and easterlies on the north side. Barotropic non-divergent simulations showed deformation, elongation and breaking of absolute vorticity contours, creating a series of vortices with relatively high absolute vorticity in their cores; the whole pattern of vortices moved towards the west and slightly towards the north, while the instability of the original zonal flow moved towards the east; this behaviour is consistent with observations of the ITCZ (Agee 1972, Nieto Ferreira and Schubert 1997). The MinEF-$\mathcal{E}$ with two edges captured a northward displacement of the easterly wind maximum, as well as the flattening of the absolute vorticity profile in tropical regions, behaviour which is consistent with the direct numerical integration. Maximum entropy theory qualitatively captured changes of the flow in the southern hemisphere, but showed strong sensitivity to small variations of the scale and strength of the initial condition. The predictions of MinEF-$\mathcal{M}$ with one and two edges, and MinEF-$\mathcal{E}$ with one edge, showed little skill in predicting the end-state; the weak decay of enstrophy observed in the time integration model for these cases is a major factor in the predictive skill of the theory.

In chapter 7 we studied experiments with two-dimensional turbulence on the sphere and expanded the maximum entropy theory to consider full two-dimensional equilibrium states, in contrast with the longitude-independent predictions of chapters 5 and 6. The major change to the maximum entropy theory was to account for the conservation of the angular momentum vector and not just for the angular momentum component parallel to the rotation axis of the sphere. Expressions for the three components of the angular momentum vector in an inertial reference frame were derived and incorporated to the maximum entropy code for a rotating and non-rotating sphere. Direct numerical integrations of an initial condition consisting of five westerly jets and four easterly jets

were performed; the magnitude of the zonal wind maximum was of the order of 20 ms^{-1}. Strong turbulent behaviour was observed in the numerical simulations performed on both the rotating and the non-rotating sphere. In the rotating case, the relative vorticity field after 150 days of simulation contains zonally elongated vortices of different sizes, ranging from 1,000 to 3,000 km in meridional extent, and from 2,000 to 10,000 km in their zonal dimension. A solution obtained from the maximum entropy theory contains similar types of coherent structures, but with different zonal wavenumber patterns. The zonal wind and absolute vorticity profiles showed that the direct numerical integration is between the two-dimensional and the longitude-independent maximum entropy predictions.

From the direct numerical integration in the non-rotating case, and after strong turbulent behaviour, a quadrupolar feature emerged after 80 days of evolution; that structure slowly symmetrized and, after a total of 200 days of simulation, four large vortices were present on the sphere, two with positive vorticity and two with negative vorticity, without having major interactions other that slow mutual translation, showing a tendency for an equilibrium state where the large vortices slowly move across homogeneous same-sign vorticity regions, which is consistent with a similar numerical simulation presented by Cho and Polvani (1996). Using maximum entropy theory, we obtained three quasi-orthogonal maximum entropy states of almost pure total wavenumber 2 modes, which have a similar value of entropy. Initializing the maximum entropy code with a linear combination of the quasi-orthogonal solutions, we obtained a prediction having strong similarities with the direct numerical integration at $t = 200$ days; maximum entropy predicts the correct number of vortices and approximately gives the correct orientation of the zero contour, but the vortices of the time integration are smaller and have a higher (lower) vorticity maximum (minimum).

As a brief summary of the main conclusions of this work we have:

1. Maximum entropy and minimum enstrophy theories were able to be extended to the case of a spherical domain, giving predictions for zonally symmetric equilibrum states.
2. Polar vortex experiments: Predictions from the maximum entropy theory demonstrated good skill for flows which have a substantial change over the whole sphere. Minimum enstrophy predictions showed very good agreement with flows in which the nonlinear

behaviour is restricted to a polar cap. Maximum entropy theory gave an additional source of information with the density functions, which in a probabilistic sense tells us how the vorticity field (and therefore the mass field) is redistributed at the equilibrium state; this information could be valuable in tracing atmospheric chemical components. The density functions showed good skill predicting several traced air parcel distributions.

3. Tropical shear layer experiments: The maximum entropy theory showed strong sensitivity to initial conditions with small scale features, due to the discretization of the vorticity field and a strong sensitivity of the fluid invariants (total kinetic energy and angular momentum) with respect to small variations of the parameters controlling the amplitude, width and location of the vorticity strip. The minimum enstrophy predictions were deficient due to the weak decay of enstrophy observed in the direct numerical integration, except for the MinEF-$\mathcal{E}$ with two edges, which showed some ability in detecting localized changes in the flow. The nonlinear time integration showed sensitivity to the resolution and value of the diffusion coefficient for these experiments.

4. Two-dimensional turbulence experiments: Maximum entropy theory was able to be extended to obtain fully two-dimensional predictions on the spherical domain, where account for the conservation of the total angular momentum vector was needed. For the rotating sphere case, the maximum entropy solution shares some characteristics with the direct numerical integration after 150 days of evolution. The non-rotating sphere case brought the possibility of having more than one equilibrium state, and that the end-state chosen by the nonlinear evolution of the flow might be a combination of quasi-orthogonal maximum entropy states.

In this work we have presented predictions given by two theories: minimum enstrophy and maximum entropy. From the results presented in chapters 5 and 6 we conclude that maximum entropy did better than minimum enstrophy for flows that change over the whole domain, while minimum enstrophy did better for flows that change just over a localized region of the sphere. From the computational point of view, minimum enstrophy solutions were obtained faster (in few minutes)

compared to the maximum entropy iterative code, which generally took a couple hours to converge on a Pentium I processor machine. We should note that the maximum entropy solution was able to be extended to predictions in two dimensions, while minimum enstrophy theory, in this work, computed just zonally symmetric equilibrium states. Chavanis and Sommeria (1998) showed that in the limit of strong mixing and within a given subdomain of an infinite plane, a maximum entropy state and a minimum enstrophy state are equivalent. Thus, we could expect that both theories will have similar predictions in problems with strong mixing and where their computational methods have the same assumptions.

The ideas of the maximum entropy theory have been further developed by Chavanis and Sommeria (1997), Robert and Rosier (1997) and Kazantsev et al. (1998), who used the Maximum Entropy Production Principle (MEPP), which states that during the relaxation process towards equilibrium, the system tends to maximize its rate of entropy production while it satisfies all the constants imposed by the dynamics, obtaining a set of relaxation equations leading a fluid towards equilibrium. The main difference from the Navier-Stokes equations is that the MEPP conserves the energy and all the constants of the motion of the Euler equations. This new theory leads to a natural modeling of the small scales in turbulent flows, which might be relevant for meteorological and oceanographic applications.

Although baroclinic processes have an important contribution to the growth of atmospheric instabilities and the subsequent approach towards an equilibrium configuration, these effects have not been taken into account in this work. Further insight in the role of both barotropic and baroclinic processes for atmospheric flows which approach equilibrium can be gained with a quasi-geostrophic maximum entropy model; Sommeria et al. (1991) have developed such a model and shown that a permanent isolated vortex can be obtained as the most probable state in an atmosphere with strong turbulent mixing. Additional applications of such ideas to atmospheric flows evolving over a sphere would be valuable to understanding the general circulation of the Earth's atmosphere.

REFERENCES

Agee, E. M., 1972: Note on ITCZ wave disturbances and formation of Tropical Storm Anna. *Mon. Wea. Rev.*, **100**, 733–737.

Boer, G. J., and T. G. Shepherd, 1983: Large-scale two-dimensional turbulence in the Atmosphere. *J. Atmos. Sci.*, **40**, 164–184.

Bowman, K. P., 1993a: Barotropic simulation of large-scale mixing in the Antartic polar vortex. *J. Atmos. Sci.*, **50**, 2901–2914.

Bowman, K. P., 1993b: Large-scale isentropic mixing properties of the antarctic polar vortex from analyzed winds. *J. Geophys. Res.*, **98**, 23013–23027.

Bowman, K. P., and N. J. Mangus, 1993: Observations of deformation and mixing of the total ozone field in the antarctic polar vortex. *J. Atmos. Sci.*, **50**, 2915–2921.

Bowman, K. P., 1995: Diffusive transport by breaking waves. *J. Atmos. Sci.*, **52**, 2416–2427.

Bowman, K. P., 1996: Rossby wave phase speeds and mixing barriers in the stratosphere. Part I: Observations. *J. Atmos. Sci.*, **53**, 905–916.

Bretherton, F., and D. Haidvogel, 1976: Two-dimensional turbulence above topography. *J. Fluid Mech.*, **78**, 129–154.

Burpee , R. W., 1972: The origin and structure of easterly waves in the lower troposphere of North Africa. *J. Atmos. Sci.*, **29**, 77–90.

Carlson, T. N., 1969: Some remarks on African disturbances and their progress over the tropical Atlantic. *Mon. Wea. Rev.*, **97**, 716–726.

Carnevale, G. F., J. C. McWilliams, Y. Pomeau, J. B. Weiss, and W. R. Young, 1991: Evolution of vortex statistics in two-dimensional turbulence. *Phys. Rev. Lett.*, **66**, 2735–2737.

Carnevale, G. F., J. C. McWilliams, Y. Pomeau, J. B. Weiss, and W. R. Young, 1992: Rates, pathways, and end states of nonlinear evolution in decaying two-dimensional turbulence: Scaling theory versus selective decay. *Phys. Fluids A*, **4**, 1314–1316.

Charney, J. G., and P.G. Drazin, 1961: Propagation of planetary scale disturbances from the lower into the upper atmosphere. *J. Geophys. Res.*, **66**, 83–109.

Charney, J. G., and M.E. Stern, 1962: On the Stability of Internal Baroclinic Jets in a Rotating Atmosphere. *J. Atmos. Sci.*, **19**, 159–172.

Chavanis, P. H., and J. Sommeria, 1996: Classification of self-organized vortices in two-dimensional turbulence: the case of a bounded domain. *J. Fluid Mech.*, **314**, 267–297.

Chavanis, P. H., and J. Sommeria, 1997: Thermodynamical approach for small-scale parametrization in 2D turbulence. *Phys. Rev. Lett.*, **78**, 3302–3305.

Chavanis, P. H., and J. Sommeria, 1998: Classification of robust isolated vortices in two-dimensional hydrodynamics. *J. Fluid. Mech.*, **356**, 259–296.

Cho, J. Y., and L. M. Polvani, 1996: The emergence of jets and vortices in freely evolving, shallow-water turbulence on a sphere. *Phys. Fluids*, **8**, 1531–1552.

Fjørtoft, R., 1953: On the changes in the spectral distribution of kinetic energy for two-dimensional non-divergent flow. *Tellus*, **5**, 225–230.

Fox, C., 1987: *An introduction to the calculus of variations.* Dover Publications, Inc., New York, 271 pp. [ISBN 0-486-65499-0].

Gray, W. M., 1968: Global view of the origin of tropical disturbances and storms. *Mon. Wea. Rev.*, **96**, 669–700.

Hack, J. J., and R. Jakob, 1992: Description of a global shallow water model based on the transform method. NCAR Tech. Note NCAR/TN-343+STR, 39 pp.

Hartman, D. L., 1983: Barotropic instability of the polar night jet stream. *J. Atmos. Sci.*, **40**, 817–835.

Hastenrath, S., and P. Lamb, 1978: On the dynamics and climatology of surface flow over the equatorial oceans. *Tellus*, **30**, 436–448.

Huang, H. P., and W. A. Robinson, 1998: Two-dimensional turbulence and persistent zonal jets in a global barotropic model. *J. Atmos. Sci.*, **55**, 611–632.

Ishioka, K., and S. Yoden, 1994: Non-linear evolution of a barotropically unstable circumpolar vortex. *J. Met. Soc. Japan*, **72**, 63–79.

Joyce, G., and D. Montgomery, 1973: Negative temperature states for the two-dimensional guiding-centre plasma. *J. Plasma Phys.*, **10**, 107–121.

Juckes, M. N., and M. E. McIntyre, 1987: A high-resolution one-layer model of breaking planetary waves in the stratosphere. *Nature*, **328**, 590–596.

Kazantsev, E., J. Sommeria, and J. Verron, 1998: Subgrid-scale eddy parameterization by statistical mechanics in a barotropic ocean model. *J. Phys. Oceanogr.*, **28**, 1017–1042.

Killworth, P.D. and M. E. McIntyre, 1985: Do Rossby-wave critical layers absorb, reflect or over-reflect? *J. Fluid. Mech.*, **161**, 449–492.

Kraichnan, R. H., 1967: Inertial ranges in two-dimensional turbulence. *The Physics of Fluids*, **10**, 1417–1423.

Kuo, H. L., 1949: Dynamic instability of two-dimensional nondivergent flow in a barotropic atmosphere. *J. Meteor.*, **6**, 105–122.

Lanczos, C., 1986: *The variational principles of mechanics.* Dover Publications, Inc., New York, 418 pp. [ISBN 0-486-65067-7].

Legras, B., and D. G. Dritschel, 1993: A comparison of the contour surgery and pseudo-spectral methods. *J. Comp. Phys.*, **104**, 287–302.

Leith, C. E., 1984: Minimum enstrophy vortices. *Phys. Fluids*, **27**, 1388–1395.

Marcus, P. S., 1990: Vortex dynamics in a shearing zonal flow. *J. Fluid Mech.*, **215**, 393–430.

Matsuno, T., 1970: Vertical propagation of stationary planetary waves in the winter Northern Hemisphere. *J. Atmos. Sci.*, **27**, 871–873.

Matsuno, T., 1971: A dynamical model of the stratospheric sudden warming. *J. Atmos. Sci.*, **28**, 1479–1494.

Matthaeus, W.H., and D. Montgomery, 1980: Selective decay hypothesis at high mechanical and magnetic Reynolds numbers. *Annals. N.Y. Acad. Sci.*, **357**, 203–222.

Matthaeus, W.H., W. T. Stribling, D. Martinez, and S. Oughton, 1991: Selective decay and coherent vortices in two-dimensional incompressible turbulence. *Phys. Rev. Lett.*, **66**, 2731–2734.

McIntyre, M. E., 1982: How well do we understand the dynamics of stratospheric warmings? *J. Met. Soc. Japan*, **60**, 37–65.

McIntyre, M. E., 1989: On the antarctic ozone hole. *J. Atmos. Terr. Phys.*, **51**, 29–43.

McIntyre, M. E., and T. N. Palmer, 1983: Breaking planetary waves in the stratosphere. *Nature*, **305**, 593–600.

McIntyre, M. E., and T. N. Palmer, 1984: The 'surf zone' in the stratosphere. *J. Atmos. Terr. Phys.*, **46**, 825–849.

McWilliams, 1984: The emergence of isolated coherent vortices in turbulent flow. *J. Fluid Mech.*, **146**, 21–43.

Merilees, P. E., and H. Warn, 1975: On energy and enstrophy exchanges in two-dimensional non-divergent flow. *J. Fluid Mech.*, **69**, 625–630.

Miller, J., 1990: Statistical mechanics of Euler equations in two dimensions. *Phys. Rev. Lett.*, **65**, 2137–2140.

Miller, J., P. B. Weichman, and M. C. Cross, 1992: Statistical mechanics, Euler's equations, and Jupiter's red spot. *Phys. Rev. A*, **45**, 2328–2359.

Molinari, J., D. Knight, M. Dickinson, D. Vollaro, and S. Skubis, 1997: Potential vorticity, easterly waves, and eastern Pacific tropical cyclogenesis. *Mon. Wea. Rev.*, **125**, 2699–2708.

Möller, J. D., and M. T. Montgomery, 1999: Tropical cyclone evolution via potential vorticity anomalies in a three-dimensional balance model. Accepted with revision in the *J. Atmos. Sci.*

Montgomery, D., W. H. Matthaeus, W. T. Stribling, D. Martinez, and S. Oughton, 1992: Relaxation in two dimensions and the "sinh-Poisson" equation. *Phys. Fluids A*, **4**, 3–6.

Nieto-Ferreira, R., and W. H. Schubert, 1977: Barotropic aspects of ITCZ breakdown. *J. Atmos. Sci.*, **54**, 261–285.

Nitta, T., and M. Yanai, 1969: A note on the barotropic instability of the tropical easterly currrent. *J. Meteor. Soc. Japan*, **47**, 127–130.

Norton, W. A., 1994: Breaking Rossby waves in a model stratosphere diagnosed by a vortex-following coordinate system and a technique for advecting material contours. *J. Atmos. Sci.*, **51**, 654–673.

Nozawa, T., and S. Yoden, 1997: Formation of zonal band structure in forced two-dimensional turbulence on a rotating sphere. *Phys. Fluids*, **9**, 2081–2093.

Onsager, L., 1949: Statistical Hydrodynamics. *Nuovo Cimento Suppl.*, **6**, 279–287.

Polvani, L. M., J. C. McWilliams, M. A. Spall, and R. Ford, 1994: The coherent structures of shallow-water turbulence: Deformation-radius effects, cyclone/anticyclone asymmetry and gravity-wave generation. *Chaos*, **4**, 177–186.

Reed, R. D., and R. R. Roy, 1995: *Statistical Physics for students of science and engineering.* Dover Publications, Inc., New York, 320 pp. [ISBN 0-486-68568-3].

Reed, R. J., D. C. Norquist, and E. E. Recker, 1977: The structure and properties of African wave disturbances as observed during phase III of GATE. *Mon. Wea. Rev.*, **105**, 317–333.

Rhines, P. B., 1975: Waves and turbulence on a beta-plane. *J. Fluid Mech.*, **69**, 417–443.

Robert, R., 1991: A maximum-entropy principle for two-dimensional perfect fluid dynamics. *J. Stat. Phys.*, **65**, 531–551.

Robert, R., and C. Rosier, 1997: The modeling of small scales in two-dimensional turbulent flows: A statistical mechanics approach. *J. Stat. Phys.*, **86**, 481–515.

Robert, R., and J. Sommeria, 1991: Statistical equilibrium states for two-dimensional flows. *J. Fluid Mech.*, **229**, 291–310.

Robert, R., and J. Sommeria, 1992: Relaxation towards a statistical equilibrium state in two-dimensional perfect fluid dynamics. *Phys. Review Lett.*, **69**, 2776–2779.

Schubert, W. H., M. T. Montgomery, R. K. Taft, T. A. Guinn, S. R. Fulton, J. P. Kossin and J. P. Edwards, 1999: Polygonal eyewalls, asymmetric eye contraction, and potential vorticity mixing in hurricanes. *J. Atmos. Sci.*, **56**, 1197–1223.

Simmons, A. J., 1977: A note on the instability of the African easterly jet. *J. Atmos. Sci.*, **34**, 1670–1674.

Sommeria, J., C. Nore, T. Dumont and R. Robert, 1991: Théorie statistique de la tache rouge de Jupiter. *Physique de l'atmosphère*, **312**, 999-1004.

Sommeria, J., C. Staquet and R. Robert, 1991: Final equilibrium state of a two-dimensional shear layer. *J. Fluid Mech.*, **233**, 661–689.

Tang, C., and S. A. Orszag, 1978: Two-dimensional turbulence on the surface of a sphere. *J. Fluid Mech.*, **87**, 305–319.

Thorncroft, C. D., and B. J. Hoskins, 1994a: And idealized study of African easterly waves. I: A linear view. *Quart. J. Roy. Meteor. Soc.*, **120**, 953–982.

Thorncroft, C. D., and B. J. Hoskins, 1994b: And idealized study of African easterly waves. II: A nonlinear view. *Quart. J. Roy. Meteor. Soc.*, **120**, 983–1015.

Tolman, R. C., 1979: *The principles of Statistical Mechanics.* Dover Publications, Inc., New York, 661 pp. [ISBN 0-486-63896-0].

Turkington, B., and N. Whitaker, 1996: Statistical equilibrium computations of coherent structures in turbulent shear layers. *SIAM J. Sci. Comput.*, **17**, 1414–1433.

Vallis, G. K., and M. E. Maltrud, 1993: Generation of mean flows and jets on a beta plane and over topography. *J. Phys. Oceanogr.*, **23**, 1346–1362.

Van de Konijnenberg, J. B. Flór, and G.J.F. van Heijst, 1998: Decaying quasi-two-dimensional viscous flow on a square domain. *Phys. Fluids*, **10**, 595–606.

Waliser, D. E., and C. Gautier, 1993: A satellite-derived climatology of the ITCZ. *J. Climate*, **6**, 2162–2174.

Waliser, D. E., and R. C. J. Somerville, 1994: Preferred latitudes of the Intertropical Convergence Zone. *J. Atmos. Sci.*, **51**, 1619–1639.

Waugh, D. W., and R. A. Plumb, 1994: Contour advection with surgery: A technique for investigating finescale structure in tracer transport. *J. Atmos. Sci.*, **51**, 530–540.

Whitaker, N., and B. Turkington, 1994: Maximum entropy states for rotating vortex patches. *Phys. Fluids*, **6**, 3963–3973.

Williams, G. P., 1978: Planetary Circulations: 1. Barotropic representation of jovian and terrestrial turbulence. *J. Atmos. Sci.*, **35**, 1399–1426.

Yoden, S., and Yamada, M., 1993: A numerical experiment on two-dimensional decaying turbulence on a rotating sphere. *J. Atmos. Sci.*, **50**, 631–643.

Young, W. R., 1987: Selective decay of enstrophy and the excitation of barotropic waves in a Channel. *J. Atmos. Sci.*, **44**, 2804–2812.

Appendix A

The Boltzmann mixing entropy

Following Reed and Roy (1995) we now show some of the reasoning which led Boltzmann to his formulation of the relation between the entropy of a system and the thermodynamic probability of the system.

An isolated system σ, may occupy any of various (constant) energy states. We can classify these states by means of their increasing W (the number of ways of realizing a given energy state)

$$W_1 < W_2 \cdots < W_n, \tag{A.1}$$

for $E_1, E_2, \cdots E_n$ respectively. The spontaneous evolution of the system will be such that the system passes into the more probable states. Furthermore, this evolution will proceed in the direction of increasing entropy

$$S_1 < S_2 < \cdots < S_n. \tag{A.2}$$

The existence of relations (A.1) and (A.2) suggested to Boltzmann that there must also exist a relation (which he supposed to be universal and independent of the nature of σ) between S and W,

$$S = S(W). \tag{A.3}$$

To determine the form of this functional relation, let us take two isolated and entirely independent systems σ_1 and σ_2. The probability of finding the ensemble of the two systems with σ_1 in state E_1, having an associated probability W_1, and σ_2 in E_2, with W_2, is

$$W = W_1 W_2. \tag{A.4}$$

The entropy of the ensemble, which is a sum of integrals, is the sum of the system entropies

$$S = S_1 + S_2. \tag{A.5}$$

Since S is additive and W is multiplicative, if there is to be a relation between them, it can only be such that

$$S_1 \propto \ln W_1$$

$$S_2 \propto \ln W_2$$

$$S_1 + S_2 \propto \ln W_1 W_2$$

$$S \propto \ln W. \tag{A.6}$$

When we are sampling over a large number of points N in equation (3.6), the limit of $\ln W$ for large N is proportional to $-\sum_{\ell=1}^{L} \rho_\ell \ln \rho_\ell$, as given by equation (3.7). To account for the amount of entropy on the whole domain, we must integrate

$$S \propto \int_{-1}^{1} \int_{0}^{2\pi} \ln W \, d\lambda d\mu, \tag{A.7}$$

and therefore we recover expression (3.8)

$$S[\rho_1(\lambda,\mu), \cdots, \rho_L(\lambda,\mu)] = \int_{-1}^{1} \int_{0}^{2\pi} \left(-\sum_{\ell=1}^{L} \rho_\ell(\lambda,\mu) \ln \rho_\ell(\lambda,\mu) \right) d\lambda d\mu. \tag{A.8}$$

The quantity $S[\rho_1(\lambda,\mu), \cdots, \rho_L(\lambda,\mu)]$ provides an approximate measure of the extent to which the condition of a system deviates from that corresponding to equilibrium. It was Boltzmann who demonstrated with his H-theorem that this quantity has a tendency to increase with time to a maximum, and thus a tendency for the system to approach its equilibrium condition. It is outside the scope of this discussion to provide that demostration, but the reader is referred to the work of Tolman (1979).

Appendix B

Calculus of variations with auxiliary conditions

The problem of finding the position of a point at which a function has a relative maximum or minimum requires the exploration of the infinitesimal neighborhood of that point. This exploration must show that the function has a stationary value at the point in question.

The exploration of the neighborhood of a point is the process known as "variation" which means infinitesimal change, in analogy with the derivative process of ordinary calculus. However, this infinitesimal change is made in any admissible manner.

Let us consider the case where the quantity to be maximized (or minimized) appears as a stationary integral

$$F = \int_{x_1}^{x_2} f(y, y_x, x)dx. \tag{B.1}$$

Here F is the quantity that takes on a stationary value; f is a known function of y, y_x and x, but the dependence of the y on x is not fixed; that is, $y(x)$ is unknown. This means that although the integral is from x_1 to x_2, the exact path of integration is not known (see Fig. B1). We are to choose the path of integration through points (x_1, y_1) and (x_2, y_2) to maximize (or minimize) F.

We assume there exists an optimum path for which F is stationary, and then we compare F for our optimum path with that obtained from neighboring paths. In Fig. B1 two possible paths are shown. The difference between these two for a given x is called the variation of y, δy.

If we now investigate the variation of the function F with an arbitrary number of variables $F = F(y_1, y_2, \cdots, y_n)$ and with an auxiliary condition

$$f(y_1, y_2, \cdots, y_n) = 0, \tag{B.2}$$

then, the configuration space in which a point can move is restricted to less than n dimensions. We can eliminate one of the y_k —for example y_n— from the auxiliary condition, expressing it in terms of the other y_k. Then our function would depend on the $n-1$ unrestricted variables $y_1, \cdots, y_{n-1}$ and could be handled as a free variation problem. However, frequently the elimination is a difficult procedure. To handle this problem Lagrange devised a method called the "method

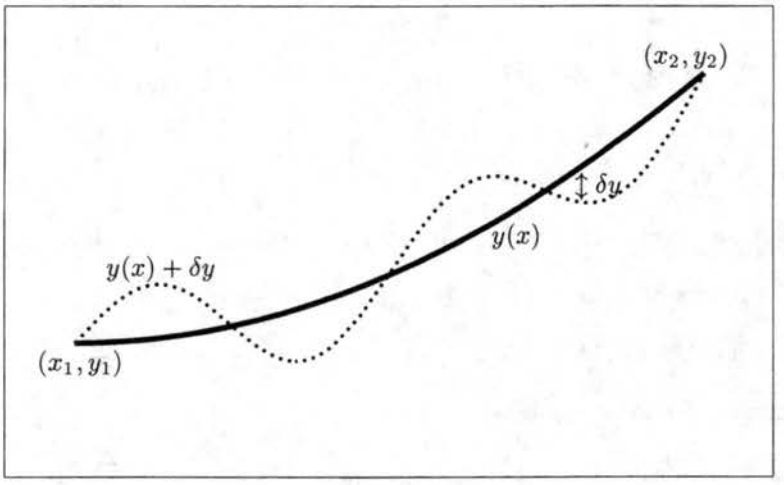

Figure B.1: A varied path.

of the undetermined multiplier". This method works quite generally for any number of auxiliary conditions.

In accordance with the δ notation, we write the infinitesimal changes of our coordinates in the form

$$\delta y_1, \delta y_2, \cdots, \delta y_n. \tag{B.3}$$

The corresponding change of the function F becomes by the rules of elementary calculus

$$\delta F = \frac{\partial F}{\partial y_1}\delta y_1 + \frac{\partial F}{\partial y_2}\delta y_2 + \cdots + \frac{\partial F}{\partial y_n}\delta y_n. \tag{B.4}$$

This expression is called the "first variation" of the function F. In order that F shall have a stationary value, this quantity has to vanish

$$\delta F = 0. \tag{B.5}$$

Taking the variation of (B.2) we obtain

$$\delta f = \frac{\partial f}{\partial y_1}\delta y_1 + \frac{\partial f}{\partial y_2}\delta y_2 + \cdots + \frac{\partial f}{\partial y_n}\delta y_n. \tag{B.6}$$

Multiplying (B.6) by some undetermined factor λ, which is a function of $y_1, \cdots, y_n$, and adding it to δF we get

$$\frac{\partial F}{\partial y_1}\delta y_1 + \frac{\partial F}{\partial y_2}\delta y_2 + \cdots + \frac{\partial F}{\partial y_n}\delta y_n + \lambda\left(\frac{\partial f}{\partial y_1}\delta y_1 + \frac{\partial f}{\partial y_2}\delta y_2 + \cdots + \frac{\partial f}{\partial y_n}\delta y_n\right) = 0. \tag{B.7}$$

We now write (B.7) in the form

$$\sum_{k=1}^{n} \left(\frac{\partial F}{\partial y_k} + \lambda \frac{\partial f}{\partial y_k} \right) \delta y_k = 0. \tag{B.8}$$

We wish to eliminate δy_n. But now we can choose λ so that the factor multiplying δy_n shall vanish:

$$\frac{\partial F}{\partial y_n} + \lambda \frac{\partial f}{\partial y_n} = 0. \tag{B.9}$$

This eliminates δy_n, so that the sum (B.8) is reduced to only $n-1$ terms:

$$\sum_{k=1}^{n-1} \left(\frac{\partial F}{\partial y_k} + \lambda \frac{\partial f}{\partial y_k} \right) \delta y_k = 0. \tag{B.10}$$

Since only those δy_k remain which can be chosen arbitrarily, the conditions of a free variation problem are applicable. These require that the coefficient of each δy_k shall vanish:

$$\frac{\partial F}{\partial y_k} + \lambda \frac{\partial f}{\partial y_k} = 0, \qquad \text{for} \qquad k = 1, 2, \cdots, n-1. \tag{B.11}$$

The conditions (B.11), combined with the condition (B.9) on λ, lead to the conclusion that each coefficient of the sum (B.8) vanishes, just as in the case that all the variations of δy_k were free variations. The result of Lagrange's "method of the undetermined multiplier" can be formulated thus: instead of considering the vanishing of δF, consider the vanishing of

$$\delta F + \lambda \delta f, \tag{B.12}$$

and drop the auxiliary condition, handling the y_k as free, independent variables.

We can generalize this λ-method for the case of an arbitrary number of auxiliary conditions $f_1, f_2, \cdots, f_m$ as follows: Instead of asking for the stationary value of F, we ask for the stationary value of the modified function

$$\bar{F} = F + \lambda_1 f_1 + \cdots + \lambda_m f_m, \tag{B.13}$$

dropping the auxiliary conditions and handling this as a free variation problem. This yields n equations. In addition to these equations we have to satisfy the m auxiliary conditions. This gives $n+m$ equations for the $n+m$ unkonwns

$$y_1, y_2, \cdots, y_n; \lambda_1, \lambda_2, \cdots, \lambda_m. \tag{B.14}$$

After satisfying the conditions for a stationary value, the further criterion for an extremum depends on the sign of the second variation $\delta^2 F$. If $\delta^2 F$ is positive at a point P, then F is increasing in every possible direction from P and we have a minimum at that point. If $\delta^2 F$ is negative at P, then F is decreasing in every possible direction from P and we have a maximum at that point. Hence it is the sign of the second variation which enables us to determine the existence of an extremum value. For more information about the methods of the calculus of variations, the reader is referred to the work of Lanczos (1986).

Appendix C

Conservation of Angular Momentum

The angular momentum $\vec{M}$ of a particle with respect to an origin from which the position vector $\vec{r}$ is measured is defined as

$$\vec{M} \equiv \vec{r} \times \vec{p}, \tag{C.1}$$

where $\vec{p} = m\vec{v}$ is the momentum vector of the particle with mass m and velocity $\vec{v}$.

The torque or moment of force $\vec{N}$ with respect to the same origin is defined to be

$$\vec{N} \equiv \vec{r} \times \vec{F} = \vec{r} \times \frac{d\vec{p}}{dt}, \tag{C.2}$$

Now,

$$\frac{d\vec{M}}{dt} = \frac{d(\vec{r} \times \vec{p})}{dt} = \frac{d\vec{r}}{dt} \times \vec{p} + \vec{r} \times \frac{d\vec{p}}{dt}, \tag{C.3}$$

but

$$\frac{d\vec{r}}{dt} \times \vec{p} = \frac{d\vec{r}}{dt} \times m\vec{v} = m\left(\frac{d\vec{r}}{dt} \times \frac{d\vec{r}}{dt}\right) \equiv 0 \tag{C.4}$$

so that

$$\frac{d\vec{M}}{dt} = \vec{r} \times \frac{d\vec{p}}{dt} = \vec{N}. \tag{C.5}$$

If there are no torques acting on a particle (i.e., if $\vec{N} = 0$), then

$$\frac{d\vec{M}}{dt} = 0,$$

and $\vec{M}$ is a vector constant in time. This is an important conservation law theorem: the angular momentum of a particle subject to no torque is conserved.

Now we compute the total angular momentum of a two-dimensional flow on the surface of a sphere with radius a and which rotates at an angular velocity $\vec{\Omega}$. First, consider a reference frame with origin at the center of the sphere (fig. C.1), the corresponding relation for the change between the longitude-latitude (λ, ϕ) to the xyz reference frame is given by

At t=0:

$$x = a\cos\phi\cos\lambda,$$

$$y = a\cos\phi\sin\lambda,$$

$$z = a\sin\phi.$$

At t=t:

$$x = a\cos\phi\cos(\lambda + \Omega t),$$

$$y = a\cos\phi\sin(\lambda + \Omega t),$$

$$z = a\sin\phi.$$

Applying $(C.1)$ to a fluid element with area A and constant density ρ gives us the angular momentum per unit area:

$$\frac{\vec{M}}{A} = \vec{r} \times \rho\vec{v} = \vec{r} \times \rho\frac{D\vec{r}}{Dt} \tag{C.6}$$

In the xyz reference frame $\vec{r} = (x, y, z)$ and $\frac{D\vec{r}}{Dt} = \left(\frac{Dx}{Dt}, \frac{Dy}{Dt}, \frac{Dz}{Dt}\right)$, which using the transformation laws given above can be expressed in terms of (λ, ϕ) as

$$\begin{aligned}\frac{D\vec{r}}{Dt} = {} & (-a\cos\phi\sin(\lambda + \Omega t)\left[\frac{u}{a\cos\phi} + \Omega\right] - v\sin\phi\cos(\lambda + \Omega t), \\ & a\cos\phi\cos(\lambda + \Omega t)\left[\frac{u}{a\cos\phi} + \Omega\right] - v\sin\phi\sin(\lambda + \Omega t), \\ & v\cos\phi).\end{aligned}$$

Then,

$$\frac{\vec{M}}{A} = \rho\begin{vmatrix} \hat{i} & \hat{j} & \hat{k} \\ x & y & z \\ \frac{Dx}{Dt} & \frac{Dy}{Dt} & \frac{Dz}{Dt} \end{vmatrix}$$

Therefore, the components of $\frac{\vec{M}}{A} = \left(\frac{M_x}{A}, \frac{M_y}{A}, \frac{M_z}{A}\right)$ in the xyz reference frame are given by

$$\frac{M_x}{A} = -a[u + \Omega a\cos\phi]\sin\phi\cos(\lambda + \Omega t) + av\sin(\lambda + \Omega t),$$

$$\frac{M_y}{A} = -a[u + \Omega a\cos\phi]\sin\phi\sin(\lambda + \Omega t) - av\cos(\lambda + \Omega t),$$

$$\frac{M_z}{A} = a[u + \Omega a\cos\phi]\cos\phi.$$

To get the total angular momentum of the flow we integrate $\frac{\vec{M}}{A}$ over the entire domain

$$M_x = \int_{-\frac{\pi}{2}}^{\frac{\pi}{2}} \int_0^{2\pi} -a[u + \Omega a \cos\phi] \sin\phi \cos(\lambda + \Omega t) + av \sin(\lambda + \Omega t) d\lambda \cos\phi d\phi, \tag{C.7a}$$

$$M_y = \int_{-\frac{\pi}{2}}^{\frac{\pi}{2}} \int_0^{2\pi} -a[u + \Omega a \cos\phi] \sin\phi \sin(\lambda + \Omega t) - av \cos(\lambda + \Omega t) d\lambda \cos\phi d\phi, \tag{C.7b}$$

$$M_z = \int_{-\frac{\pi}{2}}^{\frac{\pi}{2}} \int_0^{2\pi} a[u + \Omega a \cos\phi] \cos\phi d\lambda \cos\phi d\phi. \tag{C.7c}$$

To derive a conservation law for each of the angular momentum components we use the momentum equations in the absence of friction

$$\frac{Du}{Dt} - \left(f + \frac{u \sin\phi}{a \cos\phi}\right) v + \alpha \frac{\partial p}{a \cos\phi \partial\lambda} = 0, \tag{C.8}$$

$$\frac{Dv}{Dt} + \left(f + \frac{u \sin\phi}{a \cos\phi}\right) u + \alpha \frac{\partial p}{a \partial\phi} = 0, \tag{C.9}$$

where $\alpha = \rho^{-1}$ is the specific volume and p is the pressure. Multiplying $(C.8)$ by $-a \sin\phi \cos(\lambda + \Omega t)$, and $(C.9)$ by $a \sin(\lambda + \Omega t)$, adding and integrating over the domain we get

$$\int_{-\frac{\pi}{2}}^{\frac{\pi}{2}} \int_0^{2\pi} -a \frac{Du}{Dt} \sin\phi \cos(\lambda + \Omega t) + 2\Omega a v \sin^2\phi \cos(\lambda + \Omega t) + uv \frac{\sin^2\phi}{\cos\phi} \cos(\lambda + \Omega t) +$$

$$a \frac{Dv}{Dt} \sin(\lambda + \Omega t) + 2\Omega a u \sin\phi \sin(\lambda + \Omega t) + u^2 \frac{\sin\phi}{\cos\phi} \sin(\lambda + \Omega t) d\lambda \cos\phi d\phi = 0, \tag{C.10}$$

where we have used integration by parts on the pressure terms to show that

$$a\alpha \int_{-\frac{\pi}{2}}^{\frac{\pi}{2}} \int_0^{2\pi} -\sin\phi \cos(\lambda + \Omega t) \frac{\partial p}{a \cos\phi \partial\lambda} + \sin(\lambda + \Omega t) \frac{\partial p}{a \partial\phi} d\lambda \cos\phi d\phi = 0.$$

Adding $a^2\Omega^2 \int_{-\frac{\pi}{2}}^{\frac{\pi}{2}} \int_0^{2\pi} \sin\phi \cos\phi \sin(\lambda + \Omega t) d\lambda \cos\phi d\phi = 0$ to $(C.10)$ and rearranging we get

$$\int_{-\frac{\pi}{2}}^{\frac{\pi}{2}} \int_0^{2\pi} \frac{D}{Dt} \left[-a[u + \Omega a \cos\phi] \sin\phi \cos(\lambda + \Omega t) + av \sin(\lambda + \Omega t)\right] d\lambda \cos\phi d\phi = 0,$$

or

$$\frac{dM_x}{dt} = \frac{d}{dt} \int_{-\frac{\pi}{2}}^{\frac{\pi}{2}} \int_0^{2\pi} -a[u + \Omega a \cos\phi] \sin\phi \cos(\lambda + \Omega t) + av \sin(\lambda + \Omega t) d\lambda \cos\phi d\phi = 0. \tag{C.11}$$

For the conservation equation of the M_y component we multiply $(C.8)$ by $-a \sin\phi \sin(\lambda + \Omega t)$, and $(C.9)$ by $-a \cos(\lambda + \Omega t)$, add, integrate over the domain, add

$$-a^2\Omega^2 \int_{-\frac{\pi}{2}}^{\frac{\pi}{2}} \int_0^{2\pi} \sin\phi \cos\phi \cos(\lambda + \Omega t) d\lambda \cos\phi d\phi = 0,$$

and rearrange to obtain

$$\frac{dM_y}{dt} = \frac{d}{dt}\int_{-\frac{\pi}{2}}^{\frac{\pi}{2}}\int_0^{2\pi} -a[u + \Omega a\cos\phi]\sin\phi\sin(\lambda+\Omega t) - av\cos(\lambda+\Omega t)d\lambda\cos\phi d\phi = 0. \quad \text{(C.12)}$$

The conservation equation of the M_z component is obtained multiplying $(C.8)$ by $a\cos\phi$, integrating over the domain and rearranging, then

$$\frac{dM_z}{dt} = \frac{d}{dt}\int_{-\frac{\pi}{2}}^{\frac{\pi}{2}}\int_0^{2\pi} a[u + \Omega a\cos\phi]\cos\phi d\lambda\cos\phi d\phi = 0. \quad \text{(C.13)}$$

Therefore,

$$\frac{d\vec{M}}{dt} = 0, \quad \text{(C.14)}$$

that is, the total angular momentum of the two-dimensional flow plus the angular momentum due to the rotation of the sphere is conserved in the absence of friction.

Equations $(C.7a)$ and $(C.7b)$ have an explicit dependence on time. One way to eliminate this is to expand the $\sin(\lambda+\Omega t)$ and $\cos(\lambda+\Omega t)$ terms and write M_x and M_y in terms of the relative vorticity ζ_r,

$$M_x = \int_{-\frac{\pi}{2}}^{\frac{\pi}{2}}\int_0^{2\pi} a^2\zeta_r\cos\lambda\cos\phi d\lambda\cos\phi d\phi\cos\Omega t - \int_{-\frac{\pi}{2}}^{\frac{\pi}{2}}\int_0^{2\pi} a^2\zeta_r\sin\lambda\cos\phi d\lambda\cos\phi d\phi\sin\Omega t$$

$$M_y = \int_{-\frac{\pi}{2}}^{\frac{\pi}{2}}\int_0^{2\pi} a^2\zeta_r\sin\lambda\cos\phi d\lambda\cos\phi d\phi\cos\Omega t + \int_{-\frac{\pi}{2}}^{\frac{\pi}{2}}\int_0^{2\pi} a^2\zeta_r\cos\lambda\cos\phi d\lambda\cos\phi d\phi\sin\Omega t$$

taking $M_x^2 + M_y^2$ we obtain

$$\left[\int_{-\frac{\pi}{2}}^{\frac{\pi}{2}}\int_0^{2\pi} a^2\zeta_r\sin\lambda\cos\phi d\lambda\cos\phi d\phi\right]^2 + \left[\int_{-\frac{\pi}{2}}^{\frac{\pi}{2}}\int_0^{2\pi} a^2\zeta_r\cos\lambda\cos\phi d\lambda\cos\phi d\phi\right]^2 = \text{constant}^2. \quad \text{(C.15)}$$

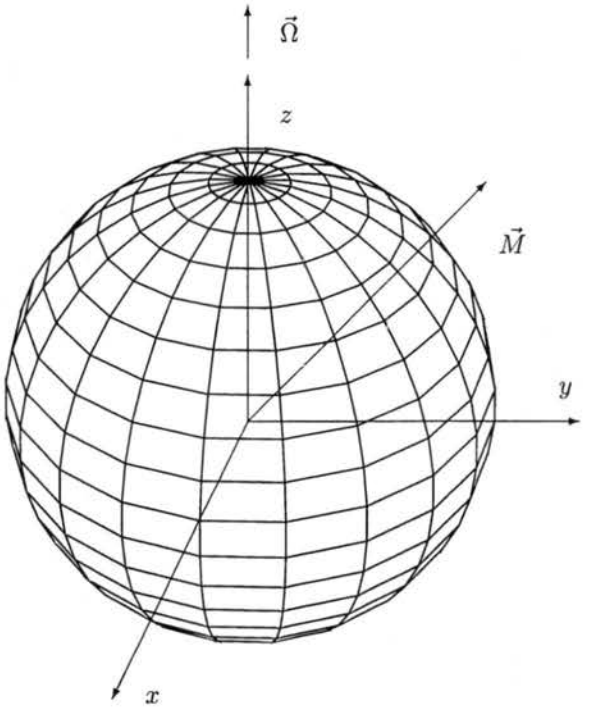

Figure C.1: A sphere with center at the origin of a fixed xyz reference frame. The sphere rotates around the z-axis at a constant angular velocity $\vec{\Omega}$. A two-dimensional flow is present on the surface of the sphere. The total angular momentum of the system is schematically shown as the vector $\vec{M}$. For Earth-type atmospheric flows the angular momentum due to $\vec{\Omega}$ has the biggest contribution to $\vec{M}$.